Chem Soc Rev

REVIEW ARTICLE

View Article Online
View Journal | View Issue

Cite this: *Chem. Soc. Rev.*, 2024, **53**, 10660

Black titanium oxide: synthesis, modification, characterization, physiochemical properties, and emerging applications for energy conversion and storage, and environmental sustainability

Xuelan Hou, [ab] Yiyang Li, [b] Hang Zhang, [c] Peter D. Lund, [c] James Kwan *[a] and Shik Chi Edman Tsang *[b]

Since its advent in 2011, black titanium oxide (B-TiO_x) has garnered significant attention due to its exceptional optical characteristics, notably its enhanced absorption spectrum ranging from 200 to 2000 nm, in stark contrast to its unmodified counterpart. The escalating urgency to address global climate change has spurred intensified research into this material for sustainable hydrogen production through thermal, photocatalytic, electrocatalytic, or hybrid water-splitting techniques. The rapid advancements in this dynamic field necessitate a comprehensive update. In this review, we endeavor to provide a detailed examination and forward-looking insights into the captivating attributes, synthesis methods, modifications, and characterizations of B-TiO_x, as well as a nuanced understanding of its physicochemical properties. We place particular emphasis on the potential integration of B-TiO_x into solar and electrochemical energy systems, highlighting its applications in green hydrogen generation, CO_2 reduction, and supercapacitor technology, among others. Recent breakthroughs in the structure–property relationship of B-TiO_x and its applications, grounded in both theoretical and empirical studies, are underscored. Additionally, we will address the challenges of scaling up B-TiO_x production, its long-term stability, and economic viability to align with ambitious future objectives.

Received 25th May 2024

DOI: 10.1039/d4cs00420e

rsc.li/chem-soc-rev

[a] *Department of Engineering Sciences, University of Oxford, Oxford, OX1 3PJ, UK. E-mail: james.kwan@balliol.ox.ac.uk*
[b] *Wolfson Catalysis Center, Department of Chemistry, University of Oxford, Oxford, OX1 3QR, UK. E-mail: edman.tsang@chem.ox.ac.uk*
[c] *Department of Applied Physics, School of Science, Aalto University, P. O. Box 15100, FI-00076 Aalto, Finland*

Xuelan Hou

Xuelan Hou is currently an assistant professor at Xi'an Jiaotong University, China. She was a Postdoctoral research assistant at both the Department of Engineering Science and the Department of Chemistry, University of Oxford, UK during the preparation of this review. Her research studies were on enhancing the efficiency and stability of photoelectrochemical cells and solar cells with black color semiconductors. Her research interests are also in black semiconductor synthesis and applications for solar energy systems and electrochemical storage systems.

James Kwan

James Kwan is an associate professor at the Department of Engineering Science and a Tutorial Fellow at Balliol College, University of Oxford, UK. Before that he obtained a PhD from Columbia University in chemical engineering. Kwan's research interests include the study of ultrasound and cavitation and applying it to address challenges in personal and environmental health. Regarding environmental health, he has a particular interest in reaction engineering and sonocatalysis to improve sonochemical performance and facilitate green chemistry.

1. Introduction

The escalating climate and energy crises have underscored the importance of renewable energy sources such as solar, wind, geothermal, biomass, hydro, and tidal energy. Solar energy, in particular, stands out as the most abundant and clean resource. With an annual solar flux of 3.00×10^{24} Joules (J) per year, reaching the Earth's surface—over 5000 times the global energy consumption in 2021—solar energy is poised to play a pivotal role in the transition to a sustainable society.[1,2] However, the full exploitation of solar energy faces several challenges: (i) the development of materials with high solar radiation capture efficiency; (ii) the creation of high-performance, stable devices for solar energy conversion and storage; and (iii) the optimization of energy storage and transportation from an economic and technological standpoint.

To capture solar energy sufficiently, 'black' semiconductors, such as black titanium oxide (B-TiO_x),[3–6] black silicon,[7–9] black phosphorus,[10–12] black bismuth vanadium oxide,[13–15] black tungstic oxide,[16] and black copper oxide,[17] are promising materials with special physicochemical properties for broadened light capture from ultraviolet (UV) to near-infrared (NIR) light, and increased numbers of charge carriers by several magnitudes. Among them, B-TiO_x has been regarded as the most promising black semiconductor with low cost and a vast range of applications.

'Black' semiconductors, such as B-TiO_x, have emerged as promising materials for broad-spectrum light capture, from UV to NIR, and for significantly increasing charge carrier generation. B-TiO_x, first synthesized *via* hydrogenation in 2011, has shown remarkable light absorption in the 360–1300 nm wavelength range and enhanced photocatalytic hydrogen production.[3] Its enduring interest stems from its unique physicochemical properties—narrow bandgap, efficient light absorption, rapid electron transport, and high electrical conductivity—coupled with the intrinsic advantages of pristine TiO_2, such as non-toxicity, affordability, chemical and mechanical stability, and versatility in shape, size, morphology, and crystalline phase. Efforts to reduce the energy and time costs of B-TiO_x production have led to innovations in synthesis, including the manipulation of blackness during fabrication.[18–20] For example, one-dimension (1D) B-TiO_x nanotubes share the same advantage with both B-TiO_x in a low charge carrier recombination rate and with 1D pristine TiO_2 nanotubes in a high specific surface area.[21–23] However, the energy and time cost of the hydrogenation method to produce B-TiO_x were huge. Therefore, tremendous efforts have been devoted to lowering the energy and time costs by manipulating the local degrees of blackness (B°) during synthesis of B-TiO_x.[24,25]

In this context, a lot of progress has been achieved in the synthesis of B-TiO_x. Significant progress has been made in optimizing B-TiO_x synthesis, with hydrogenation remaining the primary method. Synthesis conditions have been refined, and alternative techniques like plasma treatment and chemical reduction have been explored to lower production costs.

Yiyang Li is a Postdoctoral research associate at the Department of Chemistry, University of Oxford, UK. He has been working on the solar-driven photocatalytic overall water splitting for hydrogen evolution, especially the local electric and magnetic field effects in this system. His research interests also include the material

Hang Zhang is a Research Fellow at the Department of Applied Physics of Aalto University, Finland. His research covers synthesis, characterization, and self-assembly of nanomaterials, design of hydrogels with novel properties, and bio-inspired soft systems.

Shik Chi Edman Tsang

Shik Chi Edman Tsang is a professor of Inorganic Chemistry and Head of Wolfson Catalysis Laboratory at the University of Oxford, UK. He also serves as the catalysis theme coordinator in the department. His main research interests are on nanomaterials and heterogeneous catalysis concerning energy and environment which include developments of catalytic, photocatalytic and electrocatalytic technologies for green chemistry, fine chemicals, cleaner combustion, energy storages, processes and production. Particular expertise is in design and architecture of nanocatalysts and their in situ diffraction and spectroscopic characterization, which can lead to understanding of catalytic surfaces and interfaces.

Peter D. Lund is a professor of Engineering Physics and Advanced Energy Systems at the Department of Applied Physics of Aalto University, Finland. He pioneered solar energy and energy storage research in Finland. His specialization areas include both New and renewable energy systems, and Energy and innovation. He is active internationally and holds several positions of trust.

Despite these advances, B-TiO_x's performance in various applications is hampered by the rapid charge carrier recombination and suboptimal electrical conductivity. Strategies to enhance B-TiO_x's industrial-level performance include doping, noble metal nanoparticle decoration, junction construction, and facet engineering, all of which require precise characterization to identify genuine material modifications.[26] For instance, the photocatalytic H_2 evolution rate of B-TiO_x is only 0.388 mmol g^{-1} h^{-1} compared to the best recorded value of 21.1 mmol g^{-1} h^{-1} in N-TiO_2 on MgO (111), which stems from low light utilization and severe charge carrier recombination.[3] To optimize B-TiO_x towards an industrial-level performance, several strategies have been proposed, such as doping and co-doping elements, decorating noble metal nanoparticles, constructing homo/hetero/tandem junctions, facet engineering, *etc*.[27] At the same time, proper characterizations are necessary to identify the genuine modifications in B-TiO_x, resulting from different strategies.[28,29] For example, in 2023, Monai *et al.* used operando scanning transmission electron microscopy and infrared spectroscopy to observe the change of extremely thin top layer of TiO_x under hydrogenation reaction conditions.

Concerning the applications of B-TiO_x, they are mainly focused on solar energy conversion and storage systems due to their characteristic properties in light absorption, which have been studied both experimentally and theoretically.[30] For instance, B-TiO_x works as the photocatalyst to split water into H_2 and O_2 gases by the simulated sunlight source, which has great potential in addressing the challenges in the energy crisis and global warming.[31–35] On the other hand, B-TiO_x has been investigated as a functional material for efficient and reliable energy storage systems that is driven by its fast electron transport rate, long electron lifetime, relatively high electrical conductivity, vast active sites of Ti^{3+}, and oxygen vacancies (O_v). For example, B-TiO_x can serve as a crucial candidate to replace fossil fuels in ion-batteries.[36,37] Recently, B-TiO_x is renowned for its interaction with metals, known as the strong metal-support interaction, to tune catalytic performance and even product selectivity.

The rapidly increasing amount of literature on B-TiO_x calls for a continuous updating of review articles. Among them, a first comprehensive review of its fabrications, physicochemical properties, and applications was published in 2015 by Chen *et al*.[6] To date, several short articles dedicated with special focuses on the potential applications of B-TiO_x have also been reported.[4,6,30,32–34,38–40] In addition, these reviews have also covered the diversity of synthesis methods and provided understandings of the physicochemical properties of B-TiO_x though often in a specific way.[4,6,30,32–34,38,39] Meanwhile, continuous studies have deepened our understanding, revealed new properties, enriched designs for devices/installation, and broadened the applications of B-TiO_x to address the energy crisis and environmental issues. On the other hand, black semiconductors other than B-TiO_x are also gaining increasing attention due to their similar application potential for renewables. With this background, we believe that this comprehensive review serves as a timely update of the recent advances of synthesis, modification, characterization, and potential application of B-TiO_x and can also provide a future-oriented perspective on the topic of B-TiO_x.

Herein, this review first presents the definition of B-TiO_x along with its main advantages in solar light capture in Section 2. Six most important methods for the synthesis of B-TiO_x are presented in Section 3 and brief strategies for modification of B-TiO_x are outlined in Section 4. In Section 5, characteristic properties of B-TiO_x are addressed to understand the material. Representative promising applications of B-TiO_x for solar energy utilization, conversion and storage, and electrical energy storage systems are mainly given in Section 6, including water (H_2O) splitting into H_2, O_2, and H_2O_2 production and supercapacitors. In Section 7, perspectives on key challenges in controlling the local degrees of blackness and reduced depth of B-TiO_x, and some new *in situ*/*operando* preparation, modification, and characterization techniques are outlined. Large-scale production of B-TiO_x and its long-term stability are also considered toward commercialization.

Overall, this review is intended to guide readers through the nuances of cost-effective production methods for B-TiO_x and similar black semiconductors, enriching their comprehension of the materials' distinctive properties and underlying mechanisms. We will specifically highlight recent advancements in synchrotron techniques and machine learning that have been instrumental in tackling the energy and environmental challenges associated with these materials. Furthermore, we will encapsulate the strides made in their potential applications, thereby contributing to a broader technological understanding of B-TiO_x.

2. Black titanium oxide

2.1. Definition

Black TiO_x is originally named for its 'black' appearance, as shown in Fig. 1(a), which contrasts with the white color of the pristine TiO_2. In this review, we define a material as black TiO_x (B-TiO_x), if it satisfies one of the following criteria, or is a modification thereof:[41]

(i) Non-white color of TiO_2: the color can be dark, grey, brown, deep blue, *etc*.

(ii) Narrower bandgap than that of the pristine TiO_2 of a strict value of 3.2 eV for anatase TiO_2 and 3.0 eV for rutile TiO_2. As shown in Fig. 1(b), the bandgap of B-TiO_2 is 1.54 eV.

(iii) Light absorption edge longer than 400 nm.

(iv) Structurally disordered surface and subsurface is structurally disordered.

(v) Chemical formula of TiO_x, where $(0 < x < 2)$.

(vi) Reductive or inert conditions during synthesis, resulting in names such as 'reduced TiO_2', 'defective TiO_2', and 'hydrogenated TiO_2'.

2.2. Potential advantages

The potential advantages of B-TiO_x share close similarity as pristine TiO_2:. (i) High chemical and thermal stability, non-toxicity, good corrosion resistance.

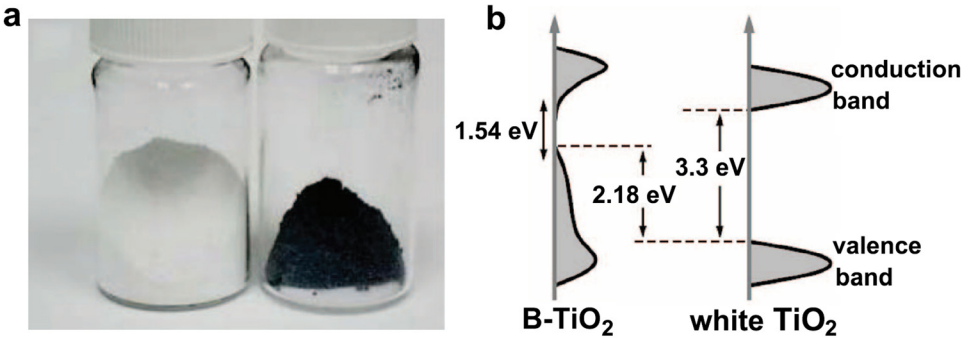

Fig. 1 (a) A photo of unmodified white TiO_2 and B-TiO_x, and (b) electronic bands of both white TiO_2 and B-TiO_x: a short-dashed curve is applied to outline a portion of the interface between the crystalline core and the disordered outer layer of B-TiO_x. Reprinted with permission from ref. 3. Copyright © 2011, The American Association for the Advancement of Science.

(ii) Various shapes, dimensions (D), and sizes: Dimensions (*e.g.*, 0D, 1D, 2D, and 3D), shapes (*e.g.*, nanofiber, nanotube, nanosheet, hierarchical flower-like), and sizes (from nanometers to microns), Fig. 2(a and b).[42–53]

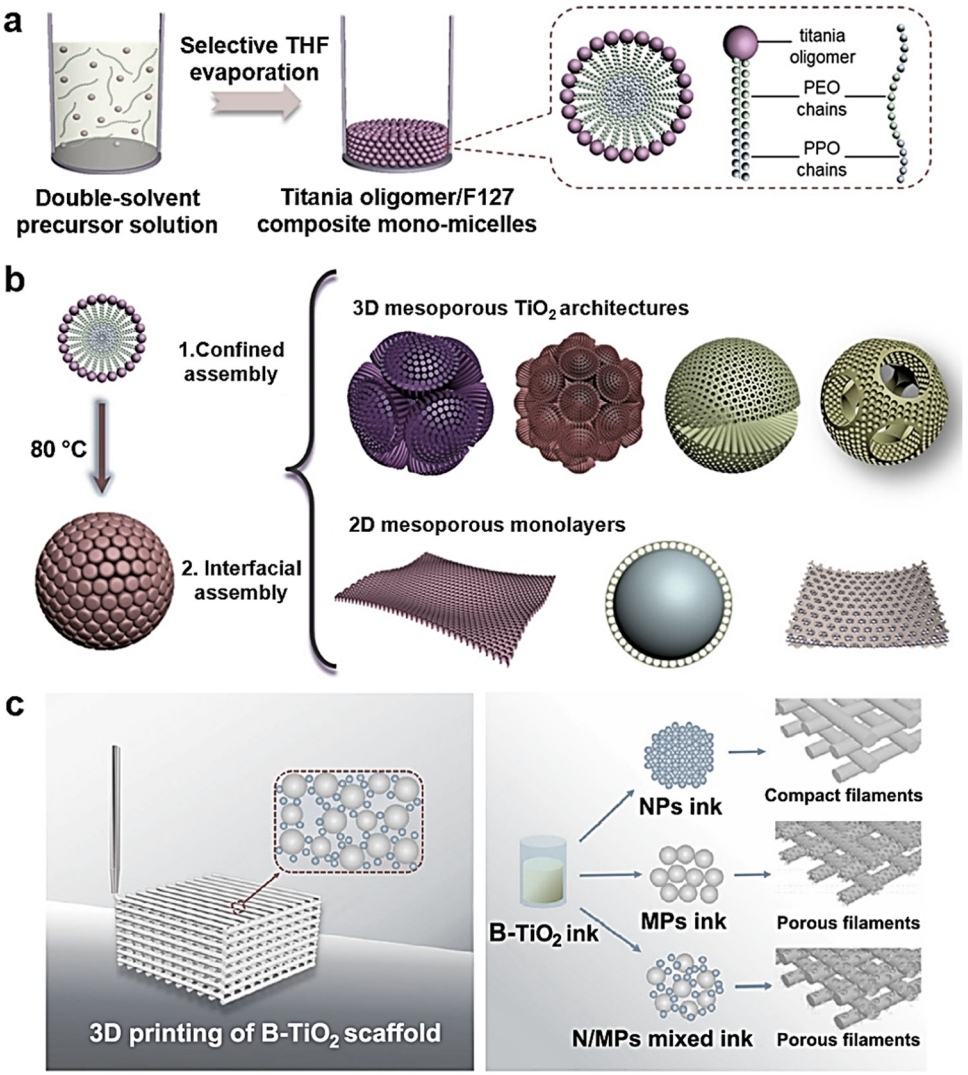

Fig. 2 (a) Synthesis of the monomicelles as building blocks for mesostructured TiO_2 materials and (b) summary of different mesoporous TiO_2 structures. Reprinted with permission from ref. 52 Copyright © 2022, Wiley-VCH GmbH. TiO_2 films are assembled from (c) 3D printing. Reprinted with permission from ref. 54. Copyright © 2019, Wiley-VCH Verlag GmbH & Co. KGaA, Weinhein.

(iii) Synthesis methods: TiO_2 powder is commonly obtained from commercial products such as P25 and from hydrothermal and sol–gel synthesis method using titanium precursors such as titanium tetrachloride.[52,53] Films are typically formed by self-assembling methods such as the anodic oxidation to form TiO_2 nanotube films on a titanium metal,[55–57] hydrothermal method,[58–60] atomic layer deposition method,[61–65] ink-jet printing method,[66] *etc.*; and coating methods (Fig. 2(c)), such as dip-coating, spin-coating, spray-coating,[67–69] doctor blade, 3D-printing method,[54,70] *etc.*

(iv) Wide range of applications including energy, environment, electronic materials, health and medicine, *etc.*

The potential advantageous properties of B-TiO_x over pristine TiO_2 are summarized below. (i) Light absorption: broadened light absorption wavelengths over the range from UV to NIR along with enhanced light absorption intensity.

(ii) Energy band: narrowed bandgap resulting from shifted valence band locations and thus-formed long band tails and mid-gaps.

(iii) Surface active site: the formation of surface defects of Ti^{3+} species, –OH, oxygen vacancies (O_v) and surface or near-surface disorders.[31]

(iv) Interface resistivity: low interface resistivity. (*e.g.*, typical B-TiO_x nanotube films are two orders of magnitude lower than anatase TiO_2 films[71]).

(v) Charge carrier: relatively higher charge carrier density, lower charge carrier recombination, and faster charge carriers' transport rate.[72]

(vi) Longer lifetime of excited electrons.

These potential advantages enable B-TiO_x to form a wide range of functional structures for a wide range of applications, for example as both the anode and cathode electrodes in a fuel cell.[3,28,73]

3. Synthesis methods

Tremendous effort has been devoted to the synthesis of B-TiO_x motivated by its wide-acknowledged advantages in its capability for absorbing the spectrum from UV to NIR range such as oxidation of hydrides.[74–76] Recently, the importance of reductive overlayer to boost catalytic reactions have also been emphasized.[77–83] Herein, this section will focus on presenting representative synthesis methods: hydrogenation, electrochemical reduction, chemical reduction, solution soaking, plasma, and ultrasonic treatment, along with the costs of economic and energetic considerations. The unique features and parameters of each method to manipulate the degree and depth of blackness (B°) of B-TiO_x are highlighted.

3.1. Hydrogenation

Hydrogenation is the first reported method to prepare B-TiO_x and has also been the most widely used one.[3,84] It is typically conducted in a tube furnace (Fig. 3(a)) that enables gas flow to maintain an inert or reductive atmosphere at a temperature range of 200–800 °C for a duration of 0.5–120 h. The gas used in the tube furnace is often a single-component gas such as H_2,[21,85] N_2, CO,[86] and NH_3,[87,88] or a mixture of gases such as H_2/N_2[71,89–95] and H_2/Ar,[96] and vacuum.[97] For instance, as shown in Fig. 3(b), the N, C co-doped TiO_2 is prepared in 5% H_2/Ar at 800 °C using urea as a dopant.[98] At lower post-annealing temperature, the time for the synthesis of B-TiO_x will increase.[99] For example, TiO_2 powder has been annealed at the temperature of 200 °C that required 120 h to form B-TiO_x.[3] In contrast, the time required will be more than 360 h, if the post-annealed temperature is set at room temperature (RT).[99]

To manipulate B° of B-TiO_x, parameters including atmosphere, post-annealing temperature and duration, and annealing times that can be controlled. As depicted in Fig. 3(b), a group of photographs showing the influence of both annealing temperature and duration on the B° of B-TiO_x films along with their bandgaps, and the photoelectrochemical (PEC) water splitting (WS) performance, 21, 33, 38, 38, 36, and 20 μA cm^{-2}, respectively, under the same test conditions, is given. The PECWS performance reveals that the darker of the TiO_2 and the narrower of the bandgaps do not necessarily lead to higher activity. Therefore, it is important to control B° of B-TiO_x to an optimal range to achieve the highest performance for a specific reaction.

Despite the facile production of B-TiO_x *via* hydrogenation method, it still needs further consideration for large-scale production of B-TiO_x in aspects of energy cost, time, and consumption of high-value gases such as Ar and H_2.

3.2. Electrochemical reduction

The electrochemical reduction (ECR) method is carried out in an electrochemical (EC) cell that uses the negative potential with reductive agent(s) to produce B-TiO_x.[21,100–108]

In an EC cell, the B-TiO_x is often produced at RT for a duration of less than 1 h. For instance, Hou *et al.* prepared B-TiO_x in an EC cell using an organic electrolyte of a mixture of 0.3 wt% ammonium fluoride (NH_4F) and 6 vol% deionized H_2O in ethylene glycol (EG) under a constant 60 V for 1–3 min, giving a 3 times enhancement in the value of photocurrent density over the pristine TiO_2 under the same test conditions.[101] To manipulate B° of B-TiO_x with the ECR method, parameters including electrolytes (organic or inorganic), applied constant current/potential, and reduction time are to be controlled as listed in Table 1.[109–117] From Table 1, there is a reverse relationship between the ECR time and the applied current/potential in both inorganic and organic electrolytes. For example, 30 min is required to produce B-TiO_x in 1 M Na_2SO_4, under a bias of −0.4 V_{RHE},[109] whereas, it only takes 15 s under a bias of −5 V.[110,111]

In comparison to the hydrogenation method, the merits of the ECR method include higher cost-effectiveness and lower energy and time cost. Moreover, the ECR method enables the use of small voltages and currents from renewable electricity to power this process, such as photovoltage from solar cells.[118] It should be noted that TiO_2 in powder form cannot be employed using this method to prepare the B-TiO_x.

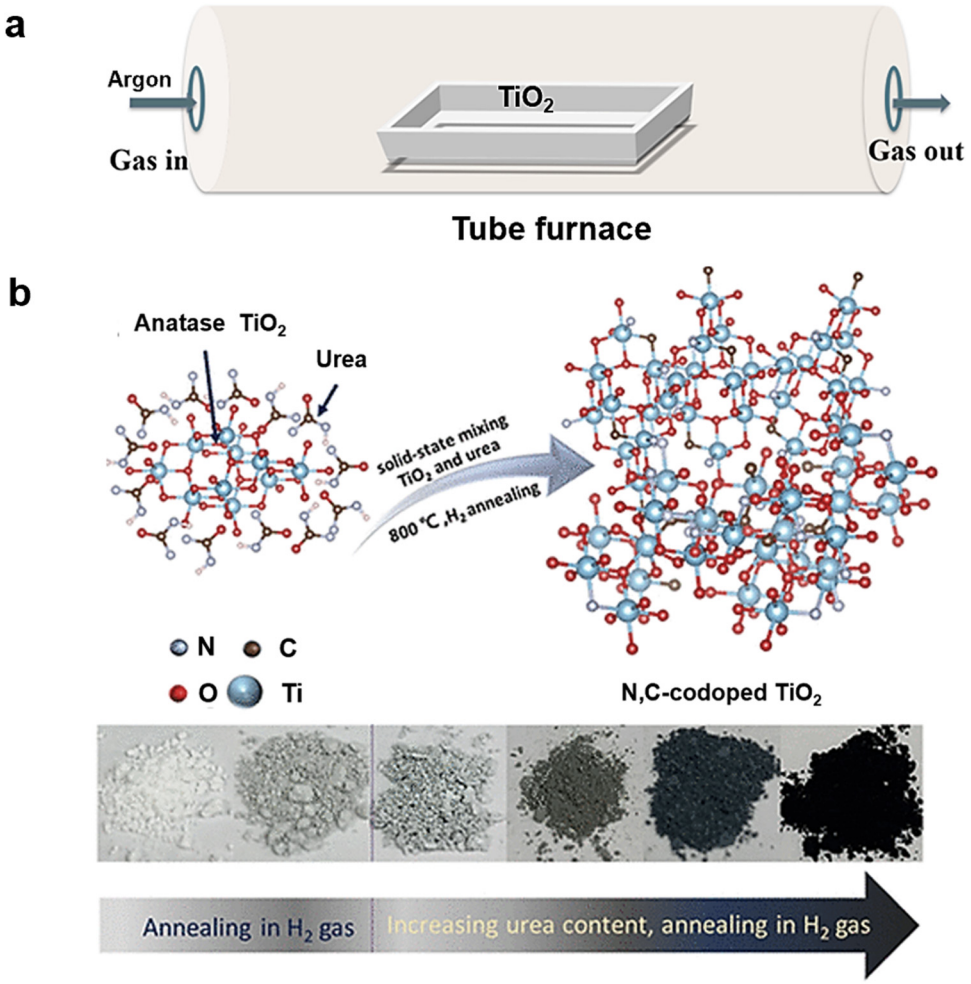

Fig. 3 (a) A schematic to show the hydrogeneration method using Ar gas in a tube furnace, and (b) a drawing and photographs concerning the synthesis of N, C-codoped TiO_2 samples under H_2 gas condition. Reprinted with permission from ref. 98. Copyright © 2020, American Chemical Society.

Table 1 Summary of the factors of electrolyte, current or potential, and reduction time that affect the electrochemical reduction of the TiO_2 sample

No.	Electrolyte	Bias/Current	Time	Ref.
1	1 M Na_2SO_4	−0.4 V_{RHE}	30 min	109
2	0.5 M Na_2SO_4	−5 V	0.25 min	110 and 111
3	0.5 M Na_2SO_4	−1.0 V_{SCE} −1.2 V_{SCE} −1.4 V_{SCE} −1.6 V_{SCE}	10 min	112
4	1 M $NaClO_4$	−5 mA cm^{-2}	10 min	113
5	0.1 M potassium phosphate buffer solution (KPi)	−5 mA cm^{-2}	10 min	93
6	Phosphate buffer solution, pH = 7.2	−17 mA cm^{-2}	1.5 min	114
7	1 M Li_2SO_4 aqueous solution	−1.2 $V_{Ag/AgCl}$	30 min	115
8	EG solution of 0.27 wt% NH_4F	−40 V	3.33 min (200 s)	100 and 116
9	0.3 wt% NH_4F and 6 vol% H_2O in EG	−60 V	1 min 2 min 3 min	101
10	0.27 wt% NH_4F and 5 wt% H_2O in EG	−30 V −35 V −40 V −45 V −50 V	15 min 20 min 30 min 60 min 120 min	117
11	200 mL EG and 10 mL 1 M of Na_2SO_4	−6 V	0.5 min	107

3.3. Chemical reduction

The chemical reduction (CR) method involves the use of reductive agents to generate the reductive condition to produce B-TiO_x.[119–121] There are two kinds of reductive agents commonly used in the CR process: active metals such as Mg[122,123] and Al,[84,91,124–126] and active hydrogen providing chemicals such as $NaBH_4$,[127–135] KBH_4,[136] and CaH_2.[137]

The CR process using active metals such as Al consists of two furnace zones: The high-temperature zone works at the temperature around 800 °C to melt Al to form a reductive condition, and the low-temperature zone is kept at 500 °C to blacken TiO_2, which is suitable to prepare both B-TiO_x powders, and B-TiO_x films.[120] In literature, the duration of the CR process is between 0.5–6 h.[84,121,125] So far, the two-zone CR method with active metals does not yet provide further information on how to control the B° of B-TiO_x.

On the other hand, using active hydrogen providing chemical sources (*i.e.*, KBH_4) is another option to produce B-TiO_x.[127,128,136,138] Here, N-TiO_2 and $NaBH_4$ are mixed and grounded for 30 min at RT, which is then post-annealed at 350 °C for 55 min under the Ar gas.[136,138] Besides, a liquid-state CR process, *viz*, a solvent CR process, uses reductant chemicals to produce B-TiO_x. To manipulate B° of B-TiO_x, the concentration of the chemical, the reaction temperature, and the duration can be adjusted. For example, tuning the weight of KBH_4 from 0.025 g, 0.050 g, and 0.100 g, can control the concentration of Ti^{3+} in B-TiO_x.[136] The highest performance with KBH_4 (0.050 g) gives a photocurrent density of 0.55 mA cm^{-2}, which is 1.11 and 1.43 folds than other treatments: (KBH_4, 0.025 g), and (KBH_4, 0.100 g), respectively.[136]

The CR method is a facile and mild method for producing both B-TiO_x powders and films. However, further investigations are required to enrich the database.

3.4. Solution soaking

As the name implies, the solution soaking (SS) method synthesizes the B-TiO_x by soaking TiO_2 in aqueous electrolyte(s). For example, B-TiO_x can be produced by soaking TiO_2 films in a mixture of EG and NH_4F at 60 °C. The B° and the bandgaps of B-TiO_x films are controlled by the soaking temperature, the concentration of NH_4F, and the soaking time.[139] With increasing soaking temperature and the concentration of NH_4F, the B° is increased and the bandgap is narrowed. Moreover, the influence of different solutions such as polyol solution and acidic solution along with different fluoride types and different volumes of H_2O on the B° of B-TiO_x have been studied.[140]

In summary, the SS method is energy and cost-saving, and easy to conduct. At the same time, this method allows large-scale production of B-TiO_x powders and films.

3.5. Plasma treatment

The plasma treatment has recently been intensively used to produce B-TiO_x.[141–150] For instance, Ar/H_2 plasma has been utilized to prepare B-TiO_x nanosheets by introducing both Ti^{3+} and O_v species on its surface at a power of 400 W.[151] Commonly, the components of the plasma electrode system include a power supply, a gas injection channel, a reactor, and a vessel equipped with a stirring magnetic bar.[148] Pylnev *et al.* controlled the H_2 flow rates at 0, 2, 3, 4.5, and 6 scans in a plasma system to manipulate the B° and the bandgaps of corresponding samples[145]

The plasma treatment method is a simple, cost-saving, and energy-saving one in the synthesis of B-TiO_x powders and films, which has also been applied to produce other black semiconductors, such as B-$BiVO_4$.[13]

3.6. Ultrasonic treatment

The ultrasonic method introduces surface defects and disorders to pristine TiO_2 by ultrasonication. In addition, ultrasonication is also used to assist the application of B-TiO_x in chemical reactions.[152,153]

A scheme in Fig. 4(a) gives an overview of the preparation of Pt single atoms on B-TiO_x nanotubes through an ultrasonic method.[154] To clearly understand that ultrasonic system and mechanism, a schematic gives in Fig. 4(b) showing the generator of the ultrasound and the depict of mechanism by the generation of acoustic cavitation for introducing –OH to prepare B-TiO_x: Acoustic cavitation includes the sequential processes of bubble formation, growth, oscillation, and collapse of bubbles in H_2O. The injected –OH forms defects on its surface and gives a 2.33 times improvement in the photocatalysis of acid fuchsin. Fig. 4(c) shows the photos of a series of B-TiO_x powders prepared using ultrasonic irradiation duration from 0 to 8 h, where the changes in both B° and bandgap can be observed.[155] The B-TiO_x powder prepared with ultrasonic method shows the highest enhancement of 22.1 times over the pristine TiO_2 powder in photocatalytic degradation of MB. Various parameters can be used to manipulate B° of B-TiO_x, including the ultrasonic time, the pH of the suspension, the ratio between the TiO_2 (g) and the volume of suspension, the frequency of the ultrasonic wave, the temperature, and the output power density during the ultrasonic irradiation.

This method to produce B-TiO_x is gentle, effective, controllable, and energy-saving, and can enable large-scale production. However, it has not been reported to produce B-TiO_x films so far.

4. Modifications

B-TiO_x has a wide range of promising applications: as photocatalysts for solar energy conversion and storage into solar fuels, as electronic materials for electrochemical devices, and as biomaterials for health and medicine fields, *etc.* However, at present, these have not yet been industrialized because the performance and the stability do not meet with the industrial demands. To moderate the demerits of B-TiO_x, strategies have been designed to address their limitations.[156] For instance, doping strategies are adopted to modify lattice symmetry, electrical conductivity, work function, and semiconductive

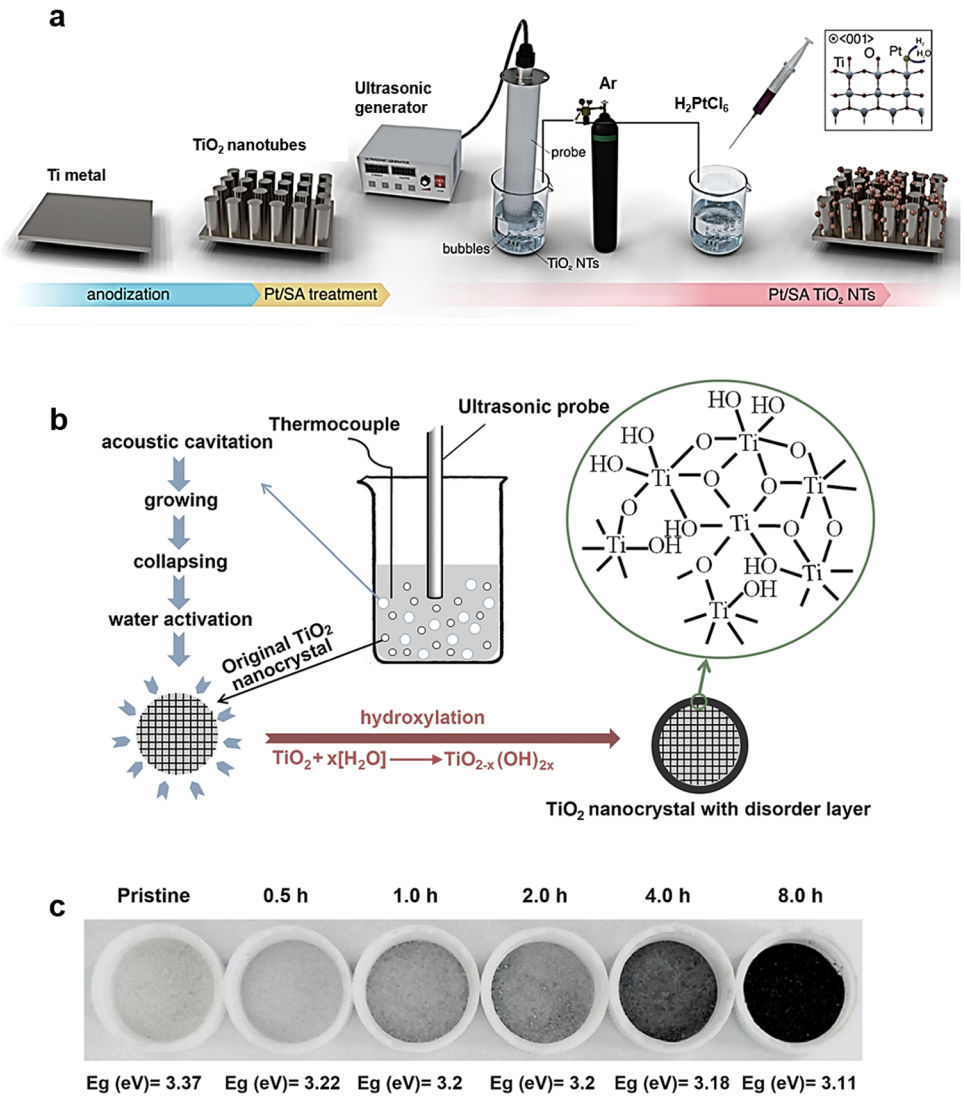

Fig. 4 (a) Schematic illustration of the fabrication of Pt single atom/B-TiO_x nanotubes. Reprinted with permission from ref. 154. Copyright © 2023 The Authors. Published by American Chemical Society. (b) Schematic illustration of the chemical process of ultrasonic treatment in forming B-TiO_x. Reprinted with permission from ref. 153. Copyright © 2017, Elsevier B.V. All rights reserved. (c) Photographs of pristine TiO_2 and B-TiO_x samples prepared with different ultrasonication duration. Reprinted with permission from ref. 155. Copyright © 2015, The Author(s).

types of B-TiO_x.[157–166] In this section, the common modification strategies of B-TiO_x will be presented.

(i) Loading single atoms (SAs), such as Au, Pt, Ru, Pd, Cu, Nb, Mn.[89,167–179]

SAs have been new emerging working catalysts for a growing number of applications such as fuel cells because of their maximal atom utilization efficiencies, *viz* a minimum use of metals, especially noble metals, and simultaneously their contribution in boosting activity, stability, and selectivity of reactions for their unique chemical and physical properties (*i.e.*, distinct as active sites towards reactions). For instance, 4.8% (Pd SA+ NPs) on TiO_2, as shown in Fig. 5(a), where the Pd SA is used for the activation of C=O group and the Pd NPs for the dissociation of H_2, gives a 3.2 times activity of commercial (5.2%) Pd/C benchmark catalyst for hydrogenation of ketone/aldehydes to alcohol under 1 atm (H_2 pressure) at 25 °C.[179] Briefly, there are two main types of structures of SAs, as shown in Fig. 5(a): Ru SA substituting a cation at the TiO_2 surface, and Ru SA supported on top of TiO_2. The two types of SAs generally exhibit different catalytic properties.[169]

(ii) Doping metal or non-metal elements: Single element doping such as P, N, C, *etc.*, and multi-elements co-doping, such as C–N co-doping, C–N–S co-doping, *etc.*[72,167,180–185]

Both self-doping and co-doping of TiO_2 can alter the characteristics of its intrinsic properties including optical, electrical, and physical properties (*i.e.*, the n-type semiconductive property), then widening their applications or enhancing performance.[186] In Fig. 6(a), the Sc and V co-doping narrow the bandgap of TiO_2 from 3.20 eV to 2.72 eV to absorb more sunlight.[187] Also, in Fig. 6(b), Cu and V co-doped TiO_2 facilitate CO_2 reduction reactions into CH_4 and CO by introducing Ti^{3+} to form intermediate band to increase separation of charge carriers, and O_v.[188]

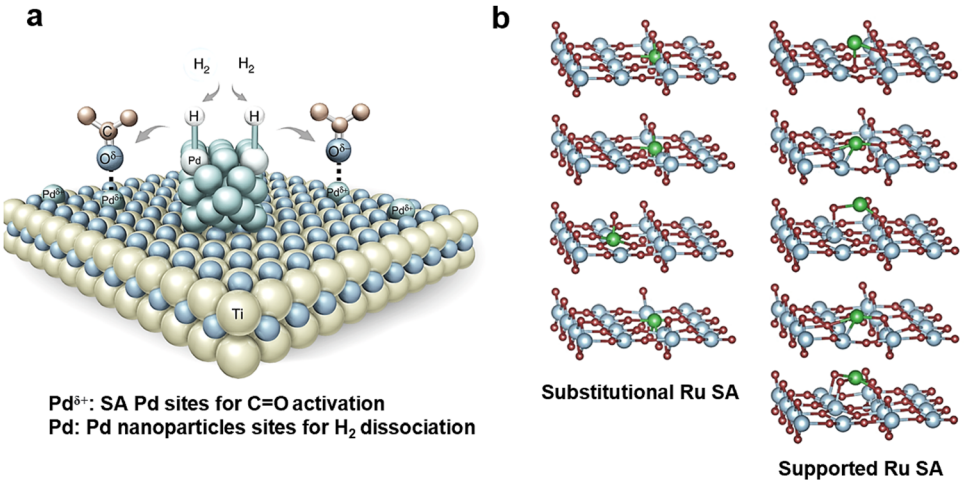

Fig. 5 (a) The mechanism of the synergistic effect of Pd SA and Pd NPs/TiO_2 catalyst for hydrogenation of ketone/aldehydes. Reprinted with permission from ref. 179. Copyright © 2020, The Author(s) (b) Substitutional and supported Rh SAs on the considered TiO_2 (110) surfaces, including O_v or adatoms (Red (O), blue (Ti), green (Rh)). Reprinted with permission from ref. 169. Copyright © 2019, The Author(s).

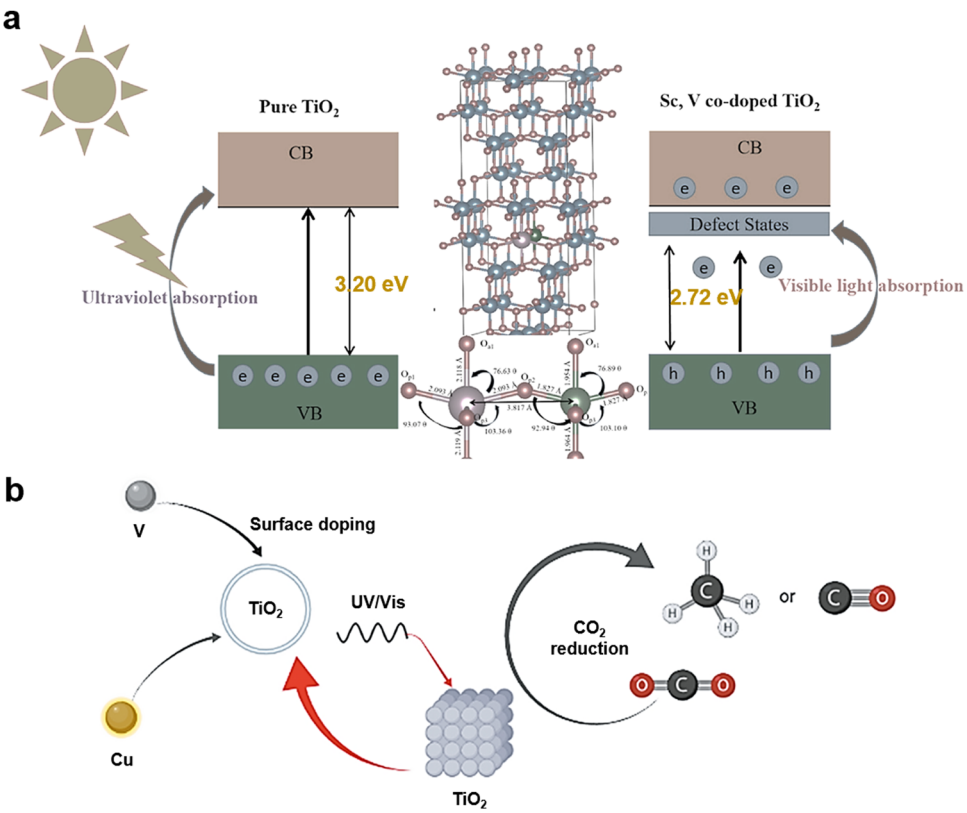

Fig. 6 (a) The band position and bandgap for pure TiO_2 and Sc, V co-doped TiO_2 with its relaxed structure of 2 × 2 × 2 supercell. Reprinted with permission from ref. 187. Copyright © 2023 Published by Elsevier B.V. (b) V, Cu co-doped TiO_2 for CO_2 reduction. Reprinted with permission from ref. 188. Copyright © 2023, The Author(s), under exclusive license to Springer Science Business Media, LLC, part of Springer Nature.

(iii) Decorating with nanoparticles (NPs), such as SiO_2 NPs, Au NPs, Ag NPs, Al_2O_3 NPs, Fe_3O_4 NPs, *etc.*[176,189–191]

(iv) Constructing new junctions: heterojunctions such as Z-scheme heterojunctions and S-scheme heterojunctions, and homojunctions.[192–198]

(v) Constructing core–shell structures: single-component core–shell structure and multi-component core–shell structure.[199,200]

(vi) Facet-engineering: expose highly active facets.[201–205]

(vii) Combination strategy: combining two or multi-strategies of (i)–(vi).[196,206]

As shown in Fig. 7(a), the Au NPs decorating on the surface of TiO_2 (Strategy-iii & iv) is often used to absorb photons because of the localized surface plasmonic resonance derived from the collective oscillation of conductive electrons with its selective injection into TiO_2 to facilitate reactions such as HER.[207–209] Typically, Au exhibits asymmetrical energy distribution in their plasmonic carriers where h^+ are much "hotter" than e^-. These hot carriers drive chemical reactions and offer to control selectivity of the reaction, unlike thermal-driven catalysis.[209] Other functions from the decorating of small NPs on TiO_2 are to increase surface area and surface affinity to anchor dye molecules in the application of solar cells, forming junctions between Fe_3O_4 and TiO_2 to narrow bandgap (Strategy-iv). They also serve as co-catalyst and active sites for accelerating reaction kinetics (in Fig. 7(c)), *etc.*[208]

Facet controls of B-TiO_x (Strategy-vi) show many aspects of interests including the growth rates of facets influence morphology of TiO_2: exposure of highly active facets influence catalytic reactions and modify decoration of Au to TiO_x, see (Fig. 7(b)). They can then affect light absorption, and charge carriers' separation and transport.[210] Accordingly, facet engineering is a useful strategy to modify B-TiO_x towards different applications.[211]

The constructions of junctions such as n–n, n–p, p–p, and tandem junctions (*i.e.*, n–p–n), (Strategy-iv) are often used to narrow bandgap to capture enough photons, to get a high photovoltage for large open circuit voltage, and to enhance e^-/h^+ transfer to their surface for a highly active reduction/oxidation reaction, *etc.*[208,212] As shown in Fig. 7(c), the constructed n-p junction shows band bending and a depletion p-type region that allows high collection of photogenerated electrons.[208] As a result, CO_2 can be reduced with e^-. Other functions such as n–n junctions between Fe_2O_3 and TiO_2 are often used to promote water oxidation to O_2. In terms of core–shell structure, we will present it in Section 5.3.

5. Characteristic properties

Different synthesis methods and modification strategies of B-TiO_x as shown above can result in varied physicochemical properties, which further improve their applications including activity and stability (Table 2).[244] This section will elucidate a selection of recent pivotal techniques aimed at acquiring a comprehensive understanding of the properties and structures of B-TiO_x and its composites. These techniques serve as a foundation for a rational design approach tailored for specific applications.[245] Particularly, the recent advances in synchrotron techniques and density functional theory (DFT) calculations have offered some new structural characterization of modified B-TiO_x which has not been made available in the past, *i.e.*, elucidating the effects of different types of oxygen vacancies (O_v) coordination and configuration on oxidation reaction. Emphasizes are placed to new structural refinement from X-ray diffraction and pair distribution function, with atomic precision and high resolution of scanning transmission electron microscopy to show metal single atom dopers. Also, *in situ* or operando techniques combined with DFT models or machine learning can also deliver new essential information on mechanistic aspects of applications.

5.1. Structural aspects

X-ray diffraction (XRD) spectroscopy is a versatile non-destructive analytical technique frequently used for investigating crystalline nanoscale materials to provide structural information such as phase identification, composition, preferred growth orientation, sample purity, crystallite size, *etc.*[246,247] For example, XRD can identify anatase and rutile B-TiO_x phases as well as Magnéli phase TiO_2 from their characteristic patterns.[248,249]

To confirm the compositions of B-TiO_x loaded with Pt on its surface (Fig. 8(a)), the XRD patterns in Fig. 8(b) are used to

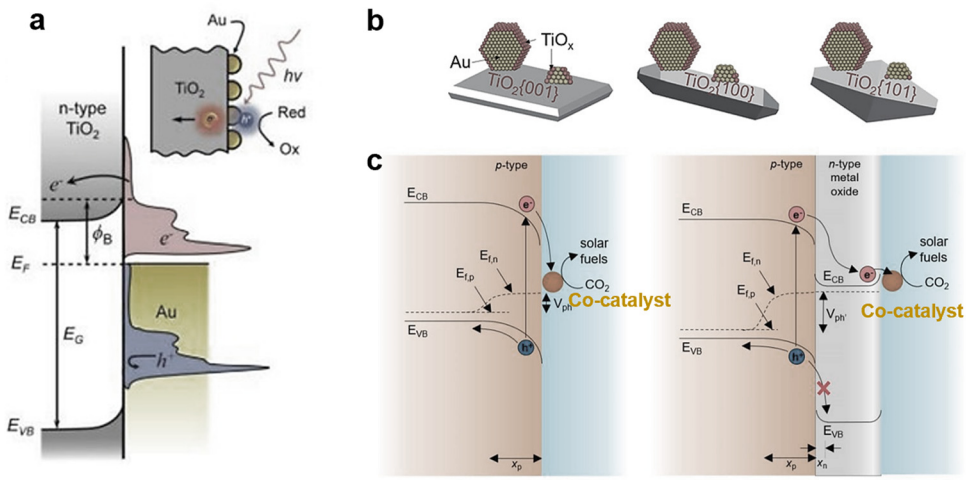

Fig. 7 (a) Schematic of plasmonic metal Au NPs on TiO_2 (heterojunctions) with a distribution of energies governed by the Au band structure and the incident photons energy. Reprinted with permission from ref. 207. Copyright © 2018, American Chemical Society. (b) Schematic of Au/TiO_2 catalysts: Au NP and TiO_x on the facets {001}, {100}, and {101} of TiO_2. Reprinted with permission from ref. 210. © 2021 Wiley-VCH GmbH (c) Energy band diagram for bare p-type semiconductor (left) and p-type semiconductor/n-type metal oxide (right) under illumination (the orange sphere denotes a cocatalyst). Reprinted with permission from ref. 208. © 2022 Wiley-VCH GmbH.

Table 2 Modification strategies of B-TiO_x

No.	Catalyst	Application system	Results	Other important points	Ref.
Strategy (i): modification with single atoms					
1	Cu (0.75 wt%)/B-TiO_x NPs	PC H_2 evolution	Production rate: Cu/B-TiO_x: 16.6 mmol g^{-1} h^{-1} Pure TiO_2: around 0.488 mmol g^{-1} h^{-1}	Function: reversible and cooperative photoactivation	175
2	Pt (0.05 wt%)/2D B-TiO_x nanosheets	PC H_2 evolution	Production rate: Pt/B-TiO_x: 65 μmol g^{-1} h^{-1} (UV light) and 688 μmol g^{-1} h^{-1} (1.7 Sun) Pure TiO_2: 5 μmol g^{-1} h^{-1}	(i) *In situ* formation Ti^{3+} (ii) Self-activation and amplification behavior of the catalyst (iii) Without sacrificial agents	50
3	Pt/B-TiO_x nanorod	As photoanode for PEC selective oxidation of glucose to glucaric	Photocurrent density: 1.9 mA cm^{-2} at 0.6 V_{RHE}, glucaric acid yield 84.3% under simulated sunlight	(i) Optimize oxygen vacancies (ii) Defects modulate the energy of VB holes that improved charge separation and transportation	213
4	Ru (0.29 wt%)/B-TiO_x nanosheet	PC H_2 evolution	H_2 production rate: Ru/B-TiO_x: 17.81 mmol g^{-1} h^{-1} (AQE% of 21.3% at 365 nm) B-TiO_x: 0.38 mmol g^{-1} h^{-1}	Ru atoms serve as charge-trapping sites and facilitate the photo-generated electron separation and transportation	151
5	Ru/B-TiO_x	PC reduction of N_2 to NH_3	NH_3 yields rate under mild conditions without any sacrificial agent: Ru/TiO_2: 18.9 μmol g^{-1} h^{-1} Pristine TiO_2: 0 μmol g^{-1} h^{-1}	(i) Rational design of catalytic sites for N_2 fixation to modulate the local electronic structure (ii) Tune the local atomic structure and accelerate the carriers transfer between Ru single atoms and TiO_2 carriers	214
6	Pd/B-TiO_x	Semi-hydrogenation of acetylene	Light irradiation boosts the conversion of acetylene in semi-hydrogenation reaction from 20 to 80% The semi-hydrogenation of acetylene can be realized at the temperature of 70 °C		215
7	Pd/B-TiO_x	PC NO_x removal	After 5 h of PC NO removal, NO_x removal efficiency is 4–5 times over that of pure TiO_2	The fraction of isolated Pd atoms on TiO_2 is quantified by diffuse reflectance infrared Fourier transform spectroscopy using NO as probing the molecule and $BaSO_4$ as the internal standard	216
8	Fe_1S_x/B-TiO_x sphere	Electrocatalytic NRR	NH_3 yields rate: 18.3 μg h^{-1} mg^{-1} FE of 17.3% at −0.2 V_{RHE}	(i) FeS_2O_2 sites are the active centers for electrocatalytic NRR (ii) Opened and ordered mesopores can facilitate mass transport and offer an enlarged active surface area for NRR	217
9	Au (0.3 wt%)/B-TiO_x nanosheets	CO oxidation	100% conversion at 120 °C with stability for 600 min B-TiO_x is without CO oxidation before 230 °C	(i) The surface defects on B-TiO_x can stabilize Au single atomic sites *via* the Ti–Au–Ti structure (ii) The Ti–Au–Ti structure promotes the catalytic properties by reducing the energy barrier and relieving the competitive adsorption on isolated Au atomic sites	218
10	W, Cu/TiO_2-rGO	Electrocatalytic HER, OER, and PC degradation	Overpotential of HER/OER: 121/295 mV @10 mA cm^{-2} Tafel slope of 96/60.3 mV dec^{-1} in 1 M KOH Photodegradation of ciprofloxacin: W, Cu/TiO_2-rGO: 98.5%, P25: 84.2%		219
Strategy (ii): Doping and co-doping					
11	Mn (1 wt%) doping TiO_2 NPs	Supercapacitor	The capacitance: 335.52 F g^{-1}, twice of pristine one:132.21 F g^{-1} The charge carrier densities have a double enhancement The anodic and cathodic peak separation is 0.09 V	This enhanced electrochemical property is ascribed to the large surface area, mesoporous structure, and appropriate concentration of Mn doping	220
12	Co doping TiO_2 nanotube	Degradation of organic pollutants	The removal rate (pseudo-first-order rate constant): 0.28 min^{-1},	(i) A relatively high electronic conductivity associated with the coexistence of Ti^{4+} and Ti^{3+} in Co–B-TiO_x enables an efficient	89

Table 2 (*continued*)

No.	Catalyst	Application system	Results	Other important points	Ref.
				electron transfer between PMS and the catalyst	
			Co_3O_4/rGO: 0.18 min^{-1} $CoFe_2O_4$: 0.17 min^{-1} Co_3O_4: 0.13 min^{-1} Co-TiO_2: 0.11 min^{-1} The arc size in EIS Nyquist plots in the order: bare TiO_2 > Co-TiO_2 > B-TiO_x > Co- B-TiO_x	(ii) A partial reduction of Ti^{4+} to Ti^{3+} enhances the degradation of organic chemical contaminants	
13	S,N co-doped graphene quantum dots TiO_2 NPs	PC production of H_2O_2	H_2O_2 yield rate: 451 μmol L^{-1} which is 3.2 times higher than that of bare TiO_2 under simulated sunlight irradiation	A mechanism of proton-coupled electron transfer to produce H_2O_2 was proposed for the highly selective two-electron H_2O_2 production	221
14	N,H co-doped TiO_2	HER	Conductivity: 98.77 μΩ cm^{-1}@300 K Overpotential (Initial): 0.6 V_{RHE}@ 10 mA cm^{-2} Overpotential (After 5 h stability): 0.42 V_{RHE}@10 mA cm^{-2}	(i) O_v and a new phase TiO_xN_y incorporation on the film surface (ii) The cathodic chronoamperometry, generating Ti(III) and Ti(II) facilitate the migration of adsorbed H_{ads} intermediates and perform as active sites that enhanced electrochemical performance	222
Strategy (iii): Decorating with nanoparticles					
15	Au NPs/B-TiO_x nanotube	PC degradation	The degradation efficiency of RhB in 60 min: Au/B-TiO_x: 82% B-TiO_x: 46%	After loading Au, the electron density increased to 6 times that of B-TiO_x Au efficiently transferred electrons and promoted carrier separation	108
16	Au NPs/TiO_2 nanorod	PC degradation of RhB	Photodegradation rate under the irradiation of visible light in 80 min: Au/TiO_2: >98% Pristine TiO_2: 15%	(i) The hybrid Au–TiO_2–C system shows extremely high chemical and mechanical stability (ii) The enhanced visible-light photocatalysis is caused by the plasmon-induced hot-electrons transfer from Au NPs to neighboring TiO_2	51
17	Pt Clusters/B-TiO_x	HER	Overpotential of HER: 18 mV_{RHE}@ 10 mA cm^{-2} Tafel slope: 12 mV dec^{-1} in 0.5 M H_2SO_4 The current density at 50 mV_{RHE} Pt clusters/B-TiO_x: 142 mA cm^{-2} TiO_2: 0.03 mA cm^{-2}	The created O_v and Pt clusters exhibit synergistic effects for optimizing the reaction kinetics	223
Strategy (iv): Constructing junctions					
18	O-$ZnIn_2S_4$ @B-TiO_x	PC H_2 evolution coupled with oxidative dehydrogenation	H_2 and benzaldehyde production rate under visible light O-$ZnIn_2S_4$@B-TiO_x: 2584.9 and 2880.5 μmol g^{-1} h^{-1} Pristine one: 49.24 and 43.38 μmol g^{-1} h^{-1}	S-scheme heterojunction	180
19	g-C_3N_4/TiO_2	PC degradation of X3B dye	The highest degradation rate constant: 0.051 min^{-1} The original one: 0.031 min^{-1}	Z-scheme Heterojunction	224
20	TiO_2/MoS_2/Cu_2S	Photothermal-PC fuel production	The PC H_2 production rate under visible light TiO_2/MoS_2/Cu_2S: 3376.7 μmol h^{-1} g^{-1} B-TiO_x: around 211.0 μmol h^{-1} g^{-1}	Tandem heterojunctions	225
21	2D/1D MoS_2/TiO_2 nanowire	CO_2 photoreduction	Under solar irradiation CO production rate: 36.3 μmol g^{-1} h^{-1} Production rate (TiO_2): 6.7 μmol g^{-1} h^{-1} (CH_4) and 0.9 μmol g^{-1} h^{-1} (CO) Under visible light irradiation: CH_4 production rate of *ca.* 81.6 μmol g^{-1} h^{-1}. Production rate (TiO_2): 0	Heterojunction	226

Table 2 (*continued*)

No.	Catalyst	Application system	Results	Other important points	Ref.
22	B-TiO_x/WO_3 on rGO	PEC WS	Photocurrent density under visible light irradiation: B-TiO_x/WO_3/rGO: 0.83 mA cm^{-2} at 0 V B-TiO_x: 0.28 mA cm^{-2} at 0 V Bandgap of the composites: 1.76 eV	Multi-composite contributes to efficient photoinduced charge carrier separation and transportation	227
23	$RuTe_2$/B-TiO_x	PC degradation of diclofenac (DCF)	The degradation efficiency of DCF under a light source (250 W xenon lamp) in 120 min: $RuTe_2$/B-TiO_x: 95.2% B-TiO_x: around 79.3%	O^{2-} is the main active substance under irradiation	228
24	1T-MoS_2@TiO_2/Ti	Supercapacitor	The specific capacitance is 428.1 F g^{-1} at 0.2 A g^{-1}, energy density is 48.2 W h kg^{-1}, power density is 2481.7 W kg^{-1}, and 97% capacitance retention after 10 000 cycle	TiO_2 nanotube provides a large surface area, shortens the transfer distance of electrolyte ions, and retards the agglomeration of MoS_2 nanosheets, enhancing the electrolyte infiltration; and the direct growth of TiO_2 nanotube on Ti foil benefits the electrons transfer in the electrode 1T-MoS_2 nanosheets possess good hydrophilicity and conductivity, which favors the fast transfer of electrolyte ions and electrons	229
Strategy (v): Core–shell structures					
25	Rutile TiO_2 (core)-TiO_{2-x}:S (shell)	Water splitting	H_2 production rate under simulated solar light: Core–shell: 0.258 mmol h^{-1} g^{-1} (STH: 1.67%) Rutile TiO_2: $<$0.1 mmol h^{-1} g^{-1} The photocurrent density of the core–shell is 30-fold higher than the rutile TiO_2 under simulated solar light	The core–shell modifications enhanced absorption in visible and near-infrared regions and facilitate charge separation and transport	124
26	Ti^{3+} self-doping B-TiO_x nanospheres/ g-C_3N_4 hollow core–shell	PC H_2 evolution	H_2 production rate: Core–shell: $\sim$808.97 μmol h^{-1} g^{-1} Pristine TiO_2: $\sim$45.04 μmol h^{-1} g^{-1} B-TiO_x: $\sim$474.34 μmol h^{-1} g^{-1}	(i) Heterojunction (ii) O_v, Ti^{3+} self-doping and core–shell nano-heterojunction enhance performance (iii) O_v improves the visible light response, Ti^{3+} induces the interface to form a self-hydrogenated shell for reducing the activation barrier of the H_2, core shell drives the transfer of photon-generated carriers to promote the photon-generated carrier separation	230
27	Crystal-Amorphous Core–Shell TiO_2 NPs	Cancer cells imaging	The limit of detection (LOD) of the 4 NBT molecule on B-TiO_x NPs can reach 10^{-6} M	(i) Heterojunction (ii) Efficient exciton separation at the crystal–amorphous interface that facilitates charge transfer from the crystal core to the amorphous shell (iii) The Fermi level of the amorphous layer shifts to a low position compared to that of the crystal core, allowing efficient photoinduced charge transfer between the amorphous shell and probe molecules	231
28	Crystalline Core with Ti^{4+} -Amorphous Shell with Ti^{3+}	PC wastewater treatment	Phenol removal percentage in 180 min under visible light irradiation Core–shell: 76.05% P25: 18.18% The removal rate (pseudo-first-order rate constant): Core–shell: around 0.62 min^{-1} P25: around 0.13 min^{-1}	Bandgap = 2.96 eV	232
29	Fe_3O_4 core @B-TiO_x shell	Wideband microwave absorption	Microwave absorption performance is evaluated by reflection loss (RL) Maximum RL of core–shell: −47.6 dB, the effective absorption bandwidth (RL $<$ −10 dB) spanned 13.0 GHz	Shell: TiO_2–TiO_{2-x} shell	233

Table 2 (*continued*)

No.	Catalyst	Application system	Results	Other important points	Ref.
			Others: −14.7 dB of Fe_3O_4; −27.9 dB of Fe_3O_4@TiO_2 corresponding effective absorption bandwidth of 2.0 GHz and 5.5 GHz, respectively		
30	Cu_2S@TiO_2	PC recovery of H_2 from H_2S	H_2 generation rate: Core–shell: 41.6 mmol h^{-1} g^{-1}, (production efficiency of 10.3%) TiO_2: 9.2 mmol h^{-1} g^{-1} (production efficiency of 2.27%)	(i) Controlling shell thickness directly influenced the optical and surface-interface properties (ii) Shell thickness varied from 12.0 to 16.7 nm (iii) 3-fold prolonged electron lifetime	234
31	O_v amorphous layer (shell) − highly crystalline layer (core)	—	The resistivity of the core shell is 5.9×10^{-3} Ω cm, which is more than five (two) orders of magnitude smaller than that of the crystalline (amorphous) TiO_2	(i) Homojunction (ii) Metallic conduction is achieved at the crystalline–amorphous homo-interface *via* electronic interface reconstruction	235
32	Nanosized graphene/TiO_x (multi-shells) − TiO_2 (core)	PC degradation of organic pollutants	The degradation rate constant: Pristine TiO_2: 3.74×10^{-4} min^{-1} Core–shell: 1.66×10^{-2} min^{-1}	Forming of homo-/hetero-junction on TiO_2	236
Strategy (vi): Facet engineering					
33	Anatase TiO_2 Sheets with dominant {001} facets	PC H_2 evolution	H_2 evolution rate: With O_v: 2332 μmol h^{-1} m^{-2} Without O_v: 1333 μmol h^{-1} m^{-2}	O_v and surface fluorine are subject to obvious surface reconstruction	237
34	Au/TiO_2 (101)	PC CO_2 reduction	CO_2 RR to CO and CH_4	(i) Au acts as a cocatalyst to trap the photogenerated electrons from semiconductors for improved charge separation and provide highly active sites for accelerated reaction kinetics	238
	Au/TiO_2 (101) and (001) Au/TiO_2 (001)		Au/TiO_2 (101): 25.9 and 5.3 μmol g^{-1} h^{-1} Au/TiO_2 (101) and (001): 16.5 and 4.0 μmol g^{-1} h^{-1} Au/TiO_2 (001): 14.9 and 3.0 μmol g^{-1} h^{-1}	(ii) Au serves as light-harvesting antennae to extend the light absorption region based on the injection of plasmonic hot electrons into the semiconductor	
35	TiO_2 dominantly exposed of {001} and TiO_2 dominantly exposed of {101} facets	Reduction of NO with NH_3	NO conversion (%) At 503 K: 10.4% of {001}, 4.3% of {101} At 623 K: 19.6% of {001}, 15.1% of {101} The reaction rate (mol g^{-1} s^{-1}) At 503 K: 1.71×10^{-6} of {001}, 7.05×10^{-7} of {101} At 623 K: 8.03×10^{-6} of {001}, 6.19×10^{-6} of {101}		239
36	TiO_2 nanosheets with O_v on {001} facets	PC CO_2 reduction to CO	The reduction rate under visible light irradiation: TiO_2 with O_v: 128.5 μmol g^{-1} h^{-1} TiO_2: 45.2 μmol g^{-1} h^{-1}	(i) {101} facets in a small number increase the recombination of photogenerated electrons and holes and inhibit the PC CO_2 reduction performance (ii) The synergistic effect of special unsaturated coordination Ti5c atom and O_v	240
37	Graphene quantum dots (GQD) @TiO_2 rutile (011)	HER	H_2 production rate GQD@TiO_2 rutile (011): 31063 μmol g^{-1} h^{-1} Pristine TiO_2 rutile (011): 6931 μmol g^{-1} h^{-1}	The charge transfer from GQD to the TiO_2 rutile (011) surface, facilitating electron–hole separation and reducing charge recombination rate	241
Strategy (vii): multi-strategy					
38	P and C modified Co_2P/B-TiO_x	PC H_2 production	The H_2 production rate under simulated solar light: P, C Co_2P/B-TiO_x: 1.53 mmol g^{-1} h^{-1} (normalized rate: 18 μmol h^{-1} m^{-2}) B-TiO_x: 1.3 μmol h^{-1} m^{-2}	S-scheme heterojunction	196
39	Fe_3O_4@SiO_2@TiO_2/rGO core–shell	PC activation of peroxydisulfate (PDS) towards degradation and mineralization of metronidazole (MNZ)	The removal efficiency of MNZ at the same conditions in 60 min Under PDS and UV: 94.2 ± 5.36% TiO_2 under PDS: 3.1 ± 0.24% TiO_2 under UV: 9.6 ± 0.74%	trapping tests, $HO^{\bullet 1}$, O_2, holes, and $SO_4^{\bullet -}$ species were identified as major reactive species	242

Table 2 (*continued*)

No.	Catalyst	Application system	Results	Other important points	Ref.
40	Pt/B-TiO_x/Cu_xO	PC H_2 evolution	H_2 evolution rate under visible-light excitation (>420 nm) Modified catalysts: 26.1 μmol g^{-1} h^{-1} TiO_2: 0.56 μmol g^{-1} h^{-1}	O_v stabilizes the Pt single atoms deposition that facilitates the separation and transfer of photogenerated charge carriers	243

Photocatalytic (PC); photoelectrochemical (PEC); hydrogen evolution reaction (HER); oxygen evolution reaction (OER); nitrogen reduction reaction (NRR); solar-to-hydrogen (STH).

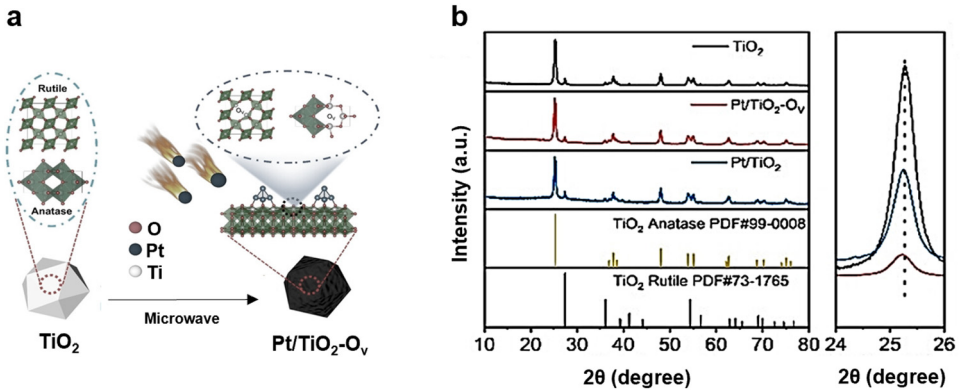

Fig. 8 (a) Diagram of the preparation process of Pt/TiO_2–O_v and (b) XRD spectra of TiO_2, Pt/TiO_2, and Pt/TiO_2–O_v. Reprinted with permission from ref. 250. Copyright © 2023. The Authors. Angewandte Chemie published by Wiley-VCH GmbH.

identify Pt/TiO_2–O_v which is composed of anatase TiO_2 (PDF# 99-0008) and rutile TiO_2 (PDF# 73-1765).[250] Further, the observation of the patterns in the 2θ range of 24–26°, confirm indirectly the O_v resulting in weaker peak intensities and broader peaks over others.[250] Similarly, XRD can be utilized to confirm multi-composition materials and identify each individual component of B-TiO_x prepared by other modification strategies such as doping metal and non-metal elements, constructing Z-Scheme junctions, and core–shell structures.[124,197,199,225,227,230,249] The size of the tiny crystalline particles influences the optical and electronic properties of materials.[251] XRD can also be used to estimate the average crystallite size of B-TiO_x according to Scherrer equation of a peak broadening.[90] Chen *et al.* reported that the average crystallite size of B-TiO_x to be 8 nm, which was further corroborated by TEM.[3] However, XRD has limited applicability to amorphous materials and nanoparticles (NPs) with small sizes, *i.e.* 5 nm. Thus, techniques such as pair distribution function (PDF) are needed.

PDF technique can elucidate the atomic arrangement of materials with high spatial resolution (Fig. 9), especially those that do not possess sharp diffraction reflections, such as amorphous materials or small-sized NPs.[252–254] This technique is appealing for gaining quantitative insights into information such as the amorphous shell or core in B-TiO_x. Particularly, PDF analysis can reveal amorphous, defects and disorder layer of B-TiO_x rather than limited information on NP sizes offered by other applications.[255–257]

Fig. 9(a) presents a schematic illustration of the distribution of atoms and the interatomic distances in a hypothetical lattice of atoms, which can be used for PDFs calculation.[254] The atoms at the position r are displayed (r corresponds to the radius of the circle at the intersection point), and upon the intersection of a new atom with the circle, a unit of intensity is incrementally added to the histogram. Thermal motion of materials causes the histogram to broaden into a Gaussians distribution, and the PDF is well represented by a sum of independent Gaussian functions.

Fig. 9(b) displays the *in-situ* time-resolved PDF profiles of TiO_2 annealed under H_2 atmosphere and the data is analyzed using Python/PDFgetX3.[258] The x-axis is the interatomic distance (r, A) of all pairs of atoms within the sample. The 2 y axes include, one for the temperature, and the other one for the function $G(r)$, *viz* the probability of finding a pair of atoms at a given interatomic distance r with an integrated intensity depending on the coherence scattering lengths of the elements involved and their multiplicities. The figure shows that the r of Ti–O is1.95/1.98 Å and the r of O–O is 2.53 Å assigned to the four equatorial O ions. When the temperature increases from 25 °C to 600 °C under H_2 atmosphere, the interatomic distances of both Ti–Ti, O (3.69 Å) and Ti–Ti (4.74 Å) show obvious shrinkage in both maxima intensity and width, which can be assigned to the removal of oxygen atoms creating the defects.

5.2. Microscopic structures

Microscopic morphologies and structures such as shapes and sizes of B-TiO_x, have pronounced effects on the performance of a reaction or in a device.[55,82,239,259–264] To characterize morphologies, scanning electron microscope (SEM), transmission

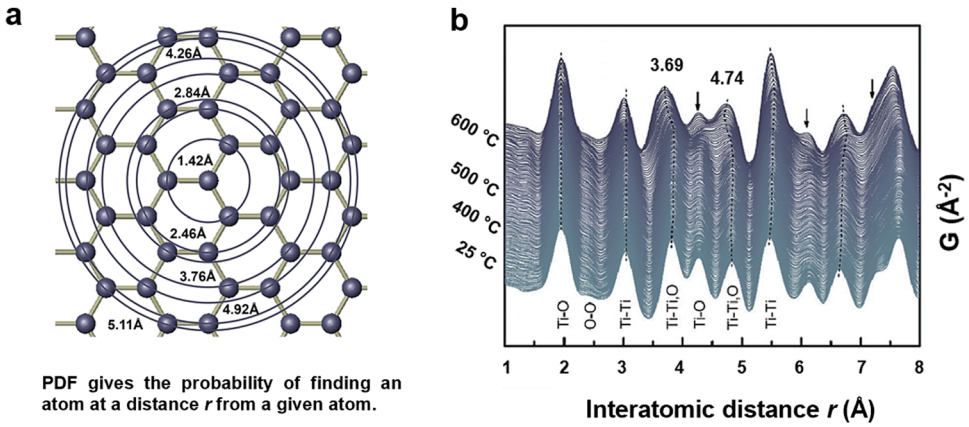

Fig. 9 (a) A schematic of the modelling process: spherically averaged distribution of interatomic distances and numbers in a hypothetical square lattice of atoms (points). Reprinted with permission from ref. 254. Copyright © Royal Society. (b) Time-resolved PDF profiles of TiO_2 upon annealing in a H_2 atmosphere (Black arrows indicate obvious changes in peak position, intensity, and width). Reprinted with permission from ref. 258. Copyright © 2016, American Chemical Society.

electron microscope (TEM), high-resolution TEM (HRTEM), and scanning transmission electron microscopy (STEM) are commonly used.

SEM has the potential to provide images of up to 2 million times magnification, which is frequently used to observe multitude of morphologies of B-TiO_x (*e.g.*, 1D nanorod, 2D nanosheet, 3D nanoflower, *etc.*), such as the nano-cubic shape of B-TiO_x (Fig. 10(a)).[42–51] In addition, sizes can be obtained from SEM images, such as the diameters of nanospheres.[265] TEM can achieve high spatial resolution down to 0.1 nm with the possibility to identify the composition and crystal structure of NPs. For instance, it has been used to observe the distribution of Au NPs with an average size of 20 nm deposited on B-TiO_x, as shown in Fig. 10(b–d).[51] Besides, TEM can provide information on the exposed facets of B-TiO_x and the ratio of different facets, along with their modifications.[133,201,202,237] For example, B-TiO_x in Fig. 10(b) shows a TEM image with an exposed facet of (101). These different exposed facets result in different surface crystallinity influencing the loading amount of Au NPs on each facet, which eventually determines the selectivity and efficiency of the catalyst. For example, in the CO_2 reduction to CO and CH_4, TiO_2 with a dominant exposure of the (101) facet give rates of 25.9 μmol g^{-1} h^{-1} for CO and 5.3 μmol g^{-1} h^{-1} for CH_4, whereas, the TiO_2 with the co-exposure of the (101) and (001) facets give rates of 16.5 μmol g^{-1} h^{-1} for CO and 4.0 μmol g^{-1} h^{-1} for CH_4.[238] HRTEM can observe features

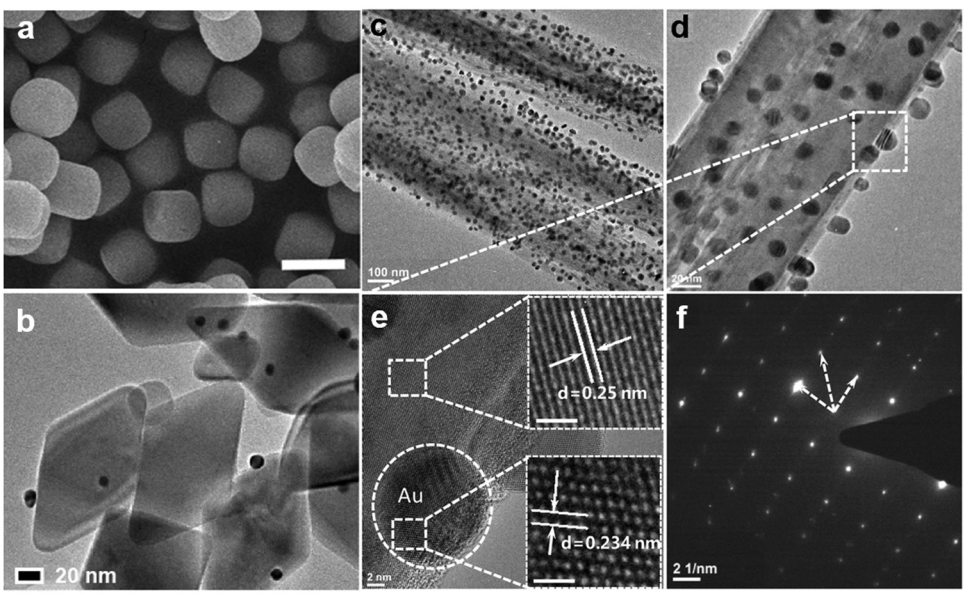

Fig. 10 SEM images of B-TiO_x (a) template of nanocubes. Reprinted with permission from ref. 44. Copyright © 2018 Elsevier B.V. All rights reserved. TEM images of (b) Au–TiO_2 co-exposed (001) and (101). Reprinted with permission from ref. 238. Copyright © 2020, Elsevier B.V. All rights reserved. TEM images of Au–TiO_2 (c) scale-bar: 100 nm, (d) scale-bar: 20 nm, and (f) HR-TEM image from the selected area in (e). Reprinted with permission from ref. 51. Copyright © 2016, Wiley-VCH Verlag GmbH & Co. KGaA, Weinhein.

with single atom resolution, *i.e.*, in the Angstrom scale, and provide additional information such as lattice fringe spacing. Fig. 10(e) and (f) presents the HR-TEM images in which the lattice spacings (*d*) are measured. In Fig. 10(e), there are two *d* values of 0.250 and 0.234 nm, corresponding to (101) facet of rutile TiO_2 and (111) facet of Au NPs, respectively.[51] HRTEM has also been utilized to characterize the morphologies and crystallite sizes of NPs, such as core–shell structure and thicknesses. With increasing number of publications using single atoms such as Pt and Au to enhance reactivity, HRTEM has proven to be a fundamental technique in the characterization of B-TiO_x.[50,151,167–169,175,216–218]

STEM combined with electron energy loss spectroscopy (EELS) is a powerful technique to characterize thin atomistic layers, based on its extremely high spatial resolution.[266–269] In this review, we reveal the use of STEM and EELS to probe details of the interface information between a thin layer of TiO_x and their composites under hydrogenation reaction conditions and observe the microstructure change of B-TiO_x during the catalytic process.[83] Fig. 11(a) shows a scheme of an operando electron microscopy setup for the observation of TiO_x at both H_2 (Fig. 11(b and c)) and CO_2:H_2 (Fig. 11(d and e)) conditions at 400 °C and atmospheric pressure. The *in-situ* HAADF-STEM

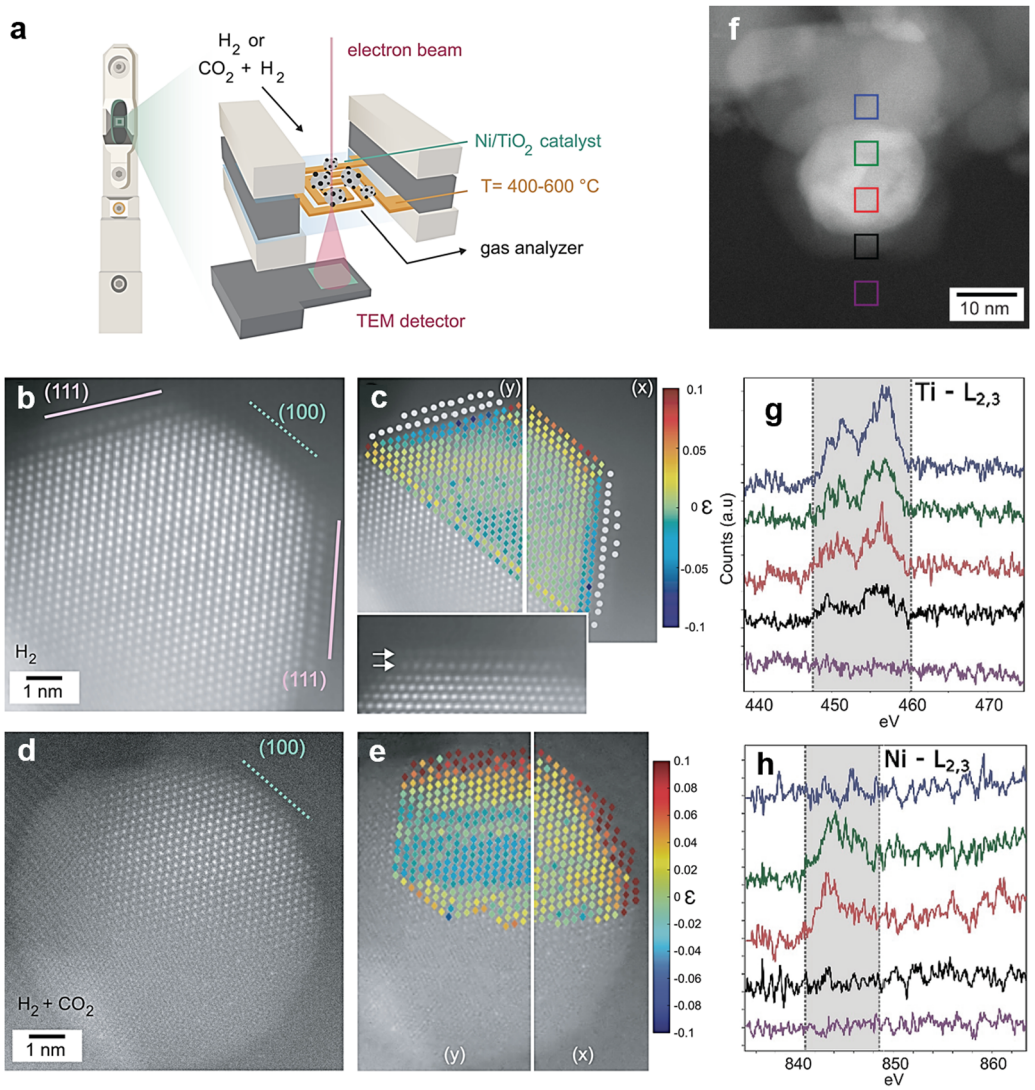

Fig. 11 (a) Schematic of the operando electron microscopy setup and windowed gas cell (climate G +, DENS solutions). (b) Representative atomic-resolution HAADF-STEM image of a Ni NP in a Ni/TiO_2 catalyst in H_2 at 400 °C. Solid lines indicate TiO_x-covered Ni atomic planes, and dashed lines indicate unoccupied facets. Ni (111) and Ni (100) facets are indicated by pink and green, respectively. (c) Estimated positions of Ti (gray) and Ni (color scale) atomic columns. (d) HAADF-STEM image of the same particle as in (b) upon exposure to a CO_2:H_2 (0.25 bar: 0.75 bar) mixture at 400 °C showing complete re-exposure of Ni and NP restructuring. (e) Estimated atomic column positions of Ni from the same particle shown in (d). Strain maps in the *x* and *y* directions resulting from the displacements with respect to the ideal atomic column positions. (f) High-resolution HAADF-STEM image of Ni/TiO_2 catalyst in H_2 at 600 °C showing a Ni NP encapsulated in a thick TiO_x shell. Colored squares correspond to the location where EELS spectra in (g) and (h) were acquired. (g and h) Core loss Ti $L_{2,3}$ and Ni $L_{2,3}$ EELS spectra. Reprinted with permission from ref. 83. Copyright © 2023, The American Association for the Advancement of Science.

imaging in Fig. 11(b) shows that the TiO_x layer encapsulates the Ni (111), and the estimated Ti and Ni atom positions are marked in Fig. 11(c), where the distances of interatomic Ti–Ti and Ni–Ti are around 2.95 ± 0.01 and 2.93 ± 0.09 Å, respectively. When changing gas condition from H_2 to CO_2 + H_2, the interface of Ni–Ti is lost from Fig. 11(d) and results in lower atomic coordination and higher mobility of surface atoms. Meanwhile, as shown in Fig. 11(d), Ni (111) is also lost and only shows some Ni (111). Also, Fig. 11(e) shows a high tensile strain over the entire NP. Fig. 11(f) shows Ni/TiO_2 at 600 °C with a completely encapsulated TiO_x overlayer. The *in-situ* EELS analysis confirms the formation of a TiO_x layer on Ni, which shows a Ti $L_{2,3}$ ionization edge signal throughout the entire Ni NP, (Fig. 11(g and h)).

5.3. Surface and interface disorders

Surface chemistry plays a critical role in determining the applications and performances of B-TiO_x catalysis.[82,83,268–271] During preparation, modification, and even applications of B-TiO_x, surface-disordered layers or defects such as O_v and Ti^{3+} of B-TiO_x are generated that could subtly affect catalytic reactions. For instance, the coordination and configuration of O_v on B-TiO_x affect water oxidation reactions.[272] According to the study by Yazdanpanah *et al.* in 2023, they demonstrated that the increase in the concentration of O_v can enlarge acid–base pairs density, which then enhanced the activity and selectivity of ketonization reaction.[273]

The most common surface defects of B-TiO_x are Ti^{3+} species, O_v, –OH, and surface/near-surface disorders that are commonly generated during synthesis and modification processes, which influence their B°, physicochemical property, and performance.[89,234,274–276] To identify these different surface states, standard measurements and analysis techniques are needed. As shown in Fig. 12(a), both the binding energy of core-level of Ti 2p and O 1s XPS are changed due to the defects from Ti^{3+}.[277] Meanwhile, electron paramagnetic resonance (EPR) or electron spin resonance (ESR) spectra techniques are often used to provide information, *i.e.* *g*-tensor values (g_x, g_y, g_z), for defects of B-TiO_x.[30,91] The EPR signals of g_x = 1.9930, g_y = 1.9930, and g_z = 1.9640 also indicate the presence of defects of B-TiO_x from Ti^{3+} in regular sites of the TiO_2 anatase phase, while the *g* values of g_x = 2.0040, g_y = 2.0129, and g_z = 2.0277 correspond to defects of oxygen ions with trapped holes (cation vacancy or surface exposure).[30] The intensity of EPR signal can also reflect the high concentration of surface defects, or alternatively, negligible intensity suggests nonexistent of surface defects.[126] For further insights into valence states and coordination environment of Ti on B-TiO_x, X-ray absorption fine structure (XAFS) spectroscopy can be invoked.[278]

The Ti K-edge X-ray absorption near edge structure (XANES) spectra of H–TiO_2, H–TiO_2–Ar, H–TiO_2–O_2 samples are shown in Fig. 12(b), the similar spectra indicate a similar local environment. Their Ti pre-edge peaks are located at 4969.4, 4972.0, and 4975.1 eV for the transitions of 1s/3d and 1s/hybridized p–d for the octahedral symmetry.

Among spectra of H–TiO_2, H–TiO_2–Ar and H–TiO_2–O_2 samples, H–TiO_2–Ar gives the highest pre-edge peak intensity, indicating a decreased Ti oxidation state and strengthened distorted local structures *via* Ar annealing treatment. This is consistent with the XPS result of Ti^{3+} on H–TiO_2–Ar. The chemical

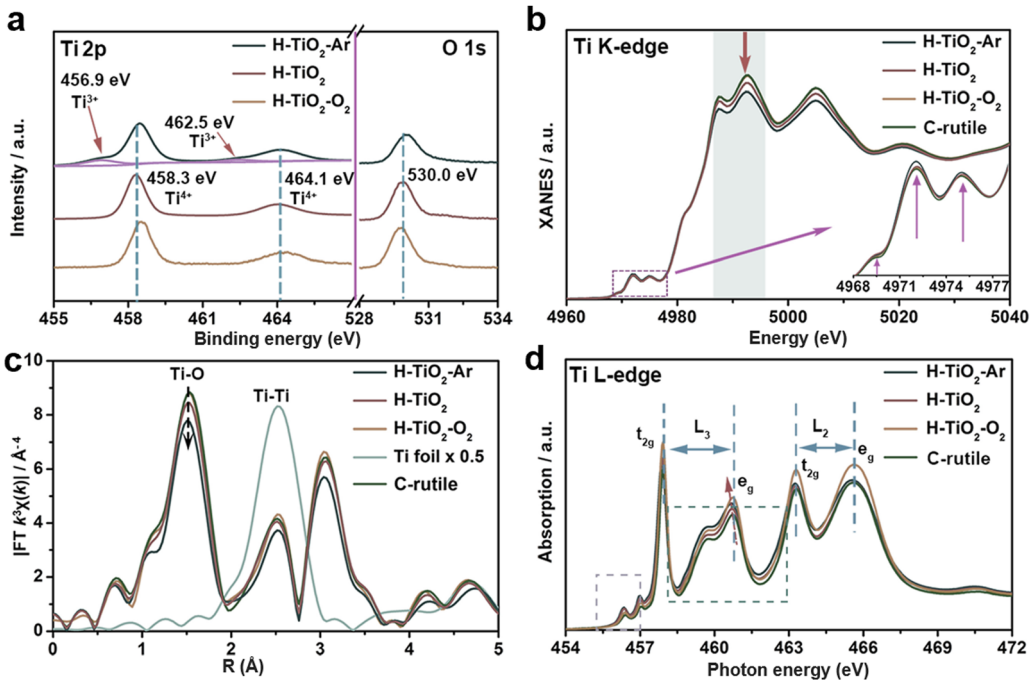

Fig. 12 Surface chemical characterization of samples of H–TiO_2 (Hydrogenated TiO_2), H–TiO_2–Ar (post-annealing H–TiO_2 in Ar), and H–TiO_2–O_2 (post-annealing H–TiO_2 in O_2). (a) XPS spectra of Ti 2p and O 1s. XANES spectra of (b) Ti K-edge, (c) k^3-weighted FT-EXAFS spectra, and (d) Ti L-edge XAFS spectra. Reprinted with permission from ref. 277. Copyright © 2021 Elsevier Inc.

environment of Ti is further examined using extended XAFS (EXAFS) spectroscopy, and the Fourier transform of EXAFS (FT-EXAFS) spectra is displayed in Fig. 12(c). The peak at 1.50 Å is ascribed to Ti–O, while the other one is for Ti–Ti. Ti L-edge spectra in Fig. 12(d) which provides information on the local electronic configuration. The H–TiO_2–Ar shows the lowest onset energy position of Ti L-edge from a lower Ti valence state.[277]

Many recent studies using DFT are employed to provide theoretical understanding on both defects of B-TiO_x and reaction pathways.[279] Here, we exemplify one of proposed mechanisms to support the importance of B° of B-TiO_x on the activity of a chemical reaction.

Fig. 13(a) shows the required energy for the H transfer on both bulk and surface O_v–O_v (0.95 and 0.84 eV) which are lower than that of surface lattice oxygen (O_v–O–O_v, 2.58 eV).[280] Indicating H preferentially transfers from the open channel rather than from a blocked one (Fig. 13b), which well supports the importance of controlling B° of B-TiO_x.[280] Recent observations also support H-transfer pathway over O_v–O_v because H co transfer in certain depth inside a metal oxide.

Chapman *et al.* combines machine learning, DFT, Group theory, and molecular dynamics (MD) to reveal the hydrogen incorporation and transport in TiO_x, which can be tailored through compositional engineering.[281] For this review, we only discuss on their work using atomic force neural network (AFNN). The AFNN-generated 1944 atom MD trajectories can analyze the local atomic geometries present across the TiO_x phase space, which is characterized using the PCA decomposition of the VGOP features. Fig. 13(c) shows TiO_x (x = 2, 1.95, 1.9, and 1.85) within this configuration space, which displays a clear separation between each case (TiO_2, $TiO_{1.95}$, $TiO_{1.9}$, and $TiO_{1.85}$), but also shows some overlap between them. For example, the TiO_2 sub-space shares some overlap with the $TiO_{1.95}$ sub-space but does not share any portion of the total space with $TiO_{1.9}$ and $TiO_{1.85}$. They argued that oscillations provide insight into the size of a given oxygen concentration's portion of the overall phase space, where the circularity of phase space serves as the basis. Fig. 13(d) shows the equilibrium configurations contained within each sub-space, as well as the outlier regions, which provides the probability of each region contained in the phase space. Overall, with the decrease of x from 2 to 1.85, the oscillations about a given chemistry's equilibrium point are reduced and the radius from the center of the approximated clustering is minimized. This seems to indicate that structures can deviate from the equilibrium configuration by a greater extent in TiO_2 than in $TiO_{1.85}$. The effect of oxygen concentration is studied by observing the probability O of 2F (OTi_2), 3F (OTi_3), and 4F (OTi_4) within the system. TiO_2 shows a higher rate of the existing of O sites over $TiO_{1.85}$ in 2F CN environment, where P(TiO_2) = 30% and P($TiO_{1.85}$) = 23%. It shows a linear trend existing of O for the case of 4F O atoms in Fig. 13(e) and (g), where in Fig. 13(e) the exist rate of TiO_2 and $TiO_{1.85}$ are 9% and 12%, separately. However, the oxygen concentration and the amount of 3F O present within the system is random (Fig. 13(f)).

The core–shell structures are of particular interests and have recently been reported extensively due to their unique electronic and structural interactions of the core component (inner layer) with the shell component (outer layer).[28,29] The core–shell structure involves at least one core and one shell layer, enabling the integration of multiple components into a functional system to overcome the demerits of a single component.[124,199,200,230,233,234,242] For example, the bandgap of a core–shell structured TiO_2 can be excitingly tuned between 1.0 to 2.8 eV rather than 3.0 eV (3.2 eV) of pristine TiO_2.

In this review, we discuss on the single-component core–shell structured B-TiO_x with disorders.[232] One example is shown in Fig. 14(a), where the single component core–shell structured TiO_2 is composed of a crystalline core and an amorphous shell, which extends the light absorption edge from around 400 nm to 1300 nm[3]. The single-component core–shell structured B-TiO_x is summarized into four types according to the introduction and distribution of Ti^{3+} species, as shown in Fig. 14(b): (i) a crystal core with Ti^{4+} and an amorphous shell with Ti^{4+}; (ii) a crystal core with Ti^{4+} and an amorphous shell with Ti^{3+}; (iii) a crystal core with Ti^{3+} and an amorphous shell with Ti^{4+}; and (iv) a crystal core with Ti^{3+} and an amorphous shell with Ti^{3+}.[28,231,232] For instance, the B-TiO_x nanotube composes of an anatase core and an amorphous shell with a thickness of 4 nm in Fig. 14(c), which is synthesized by the hydrogenation method under NH_3 gas. The nanotube possesses a strong light absorption enhancement in the wavelength range of 300–800 nm.[87] The core–shell structures and the thickness of disorder layers can be determined with the HRTEM.[73] Furthermore, the simulated density of states (DOS) reveals unprecedented effects of hydrogenation on TiO_2. As observed in Fig. 14(d) and (e), the bands of B-TiO_x after hydrogenation are severely broadened along with formation of states both below and above the VB in the shell, which are due to the existence of –OH and Ti^{3+}, respectively. The Ti^{3+} states in the shell of the B-TiO_x start just above the VB and fill most of the gap. Meanwhile, the comparison of the DOS of the B-TiO_x to the bulk crystalline anatase (Fig. 14(f)) clearly shows the overall upward shift and tailing of the VB.[282] The benefits of the core–shell structured TiO_2 for applications such as lithium-ion batteries, solar thermal energy, photocatalytic WS, *etc.*, will be addressed in Section 6.

An interface is a separating layer between two phases including gas–liquid (G–L) interface, gas–solid (G–S) interface, liquid–solid (L–S) interface, solid–solid (S–S) interface, and gas–liquid–solid (G–L–S) interface.[234,283–286] These interfaces clearly influence the transport of electrons and ions, the adsorption of reactants, the solubility and diffusion of gas in liquids, *etc.*, and determine the overall cell or chemical reaction performance in the end. Therefore, understanding the interface is important to achieve high stability and efficiency in reaction/device. For instance, the electrode–electrolyte interface is the key factor in influencing the capacity, stability, and performance of a Na-ion battery.[46]

In terms of B-TiO_x, the investigations of interface are accompanied by their studies of synthesis, modifications, and

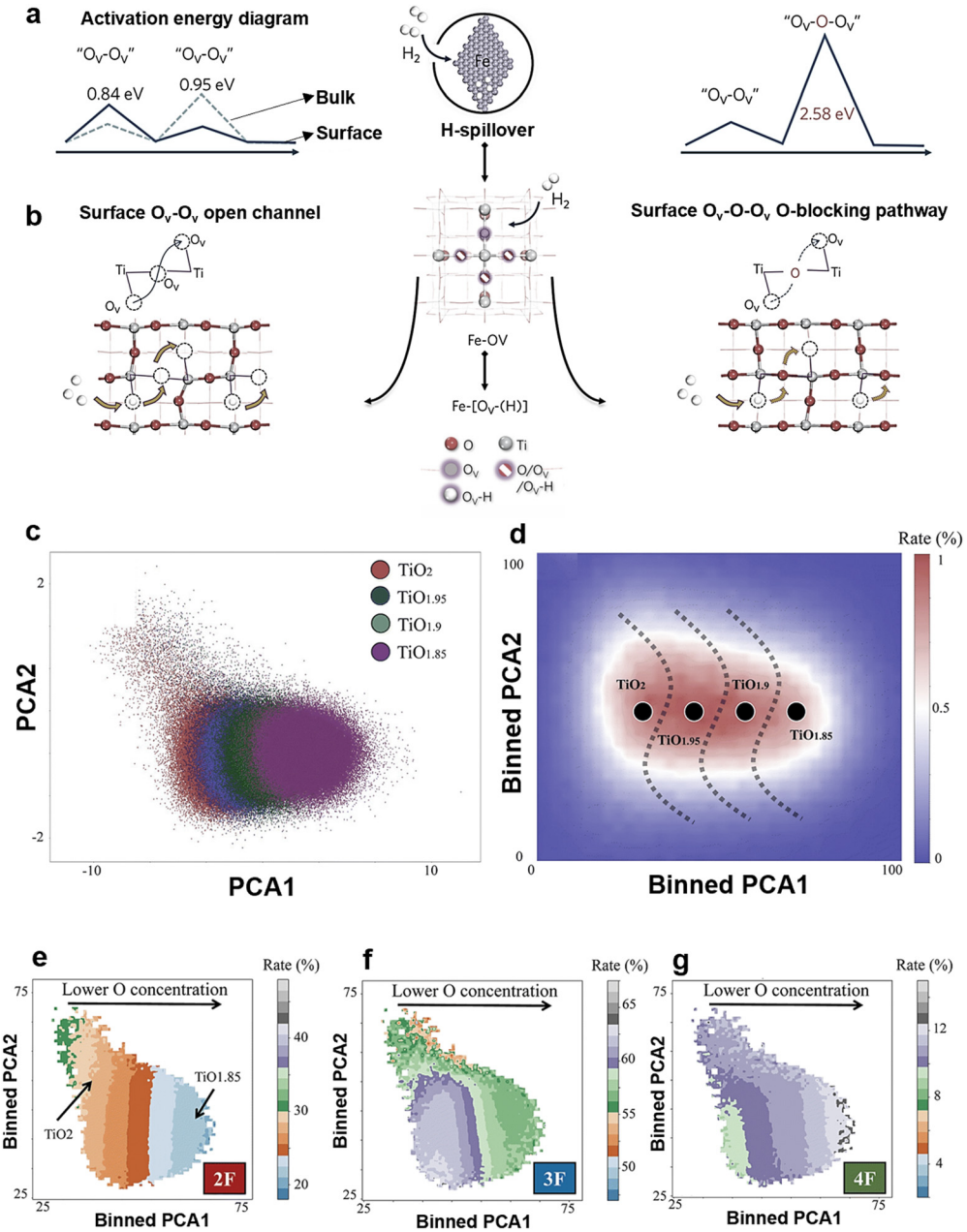

Fig. 13 (a) Schematic activation energy diagram of by O_v–O_v (left) and O_v–O–O_v (right), and (b) diagram of hydrogen transfer through cascade O_v–O_v (left) and O-obstructed O_v–O–O_v (right) pathways. The structures and activation energy barriers were obtained using DFT. Reprinted with permission from ref. 280. Copyright © 2020, American Chemical Society. (c) Principal Component Analysis (PCA)-decomposed TiO_x phase space, with colors representing varying oxygen concentrations. (d) 2D histograms of the PCA-decomposed TiO_x phase space, with occurrence rate (colors) overlayed as a third dimension. Occurrence rate is defined as the likelihood of a structure from a given PCA grid occurring in the overall phase space. Dashed lines in (d) provide visual context for the approximate boundary of each phase, where a bin contains greater than 50% of a specific phase. (e)–(g) 2D histograms of the PCA-decomposed TiO_x phase space, with coordination number (CN) probabilities (colors) overlayed as a third dimension. CN probabilities represent the likelihood of an atom having the specified CN within a structure that is contained within a given PCA grid for (e) 2F (OTi_2), (f) 3F (OTi_3), and (g) 4F (OTi_4) oxygen CN environments respectively. Reprinted with permission from ref. 281. Copyright © 2023 Royal Society of Chemistry (RSC).

applications. In the synthesis of B-TiO_x, there are two types of S–S interface including the phase interface and the interface between the core and shell formed by the same components such as the crystalline-amorphous homo-interface.[203,235,287,288] After modifications, the S–S interface is formed between B-TiO_x and other materials such as Au NPs and g-C_3N_4.[224] When employing B-TiO_x to construct a multi-junction material, a multiple S–S interface might form among different compositions.[224,236,241,289,290] In terms of their applications, the interfaces are often discussed among the B-TiO_x, the electrolyte (S or L), and the products (S, L, or G), as shown in Fig. 15(a) and (b). In the application of WS to H_2 and O_2 gases, for example, there will be the S–L–G interface among

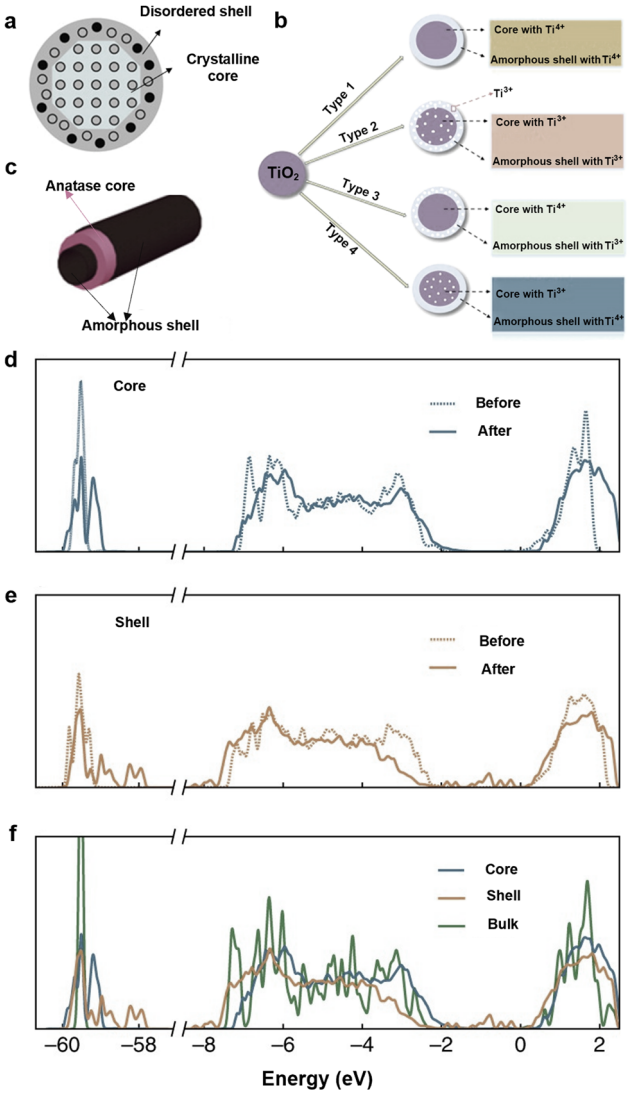

Fig. 14 (a) Schematic illustration of the core–shell structure TiO_2. Black dots represent dopants. Reprinted with permission from ref. 3. Copyright © 2011, The American Association for the Advancement of Science. (b) Scheme of four types of destructive core–shell structured TiO_2. Reprinted with permission from ref. 28. Copyright © 2019, Elsevier B.V. All rights reserved. (c) Scheme of a core–shell structured B-TiO_x nanotube. Reprinted with permission from ref. 87. Copyright © 2016, American Chemical Society. Computed DOS for the core (d), and the shell (e) of TiO_2 before and after hydrogenation treatment (f) DOS for the shell and core of B-TiO_x are compared to the DOS of bulk crystalline anatase TiO_2. Reprinted with permission from ref. 282. Copyright © 2020, Wiley-VCH GmbH.

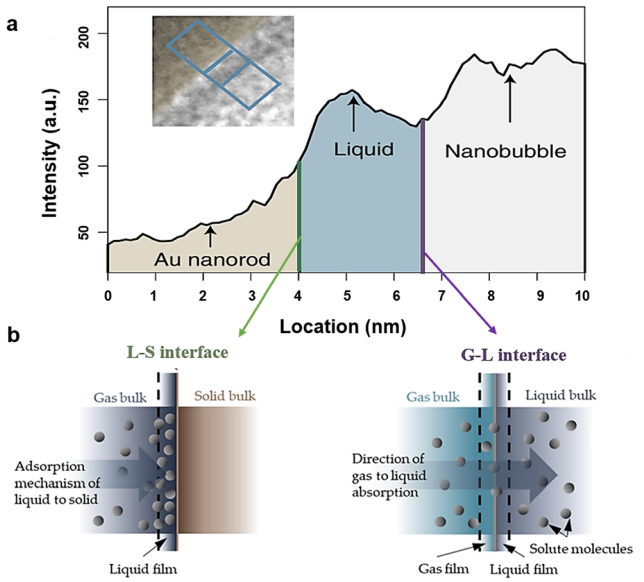

Fig. 15 (a) Solid (Au nanorod)–liquid (aqueous hydrobromic acid)–gas (oxygen gas) interface, along with an L–S interface and a G–L in (b). Reprinted with permission from ref. 295. Copyright © 2020, Wiley-VCH GmbH., and Reprinted with permission from ref. 294.

B-TiO_x (S), H_2O (L), and O_2 (G) and H_2 (G); and in the solid oxide fuel cell, the S–S interface is between the B-TiO_x electrode and the solid electrolyte.[224,241,291–295] To characterize interfacial features, techniques such as XRD, TEM, XPS, *etc.* are employed. An *in-situ* TEM images observes and records a reaction taking place on the S–L–G interface, *viz*, the O_2 nanobubbles (G) etching of Au nanorod (S) in aqueous hydrobromic acid (L) with the increasing of the reaction time.[294,295] Some cutting-edge TEM techniques reveal that when the distance between G and S is less than 1 nm. In addition, electrochemical impedance spectra (EIS) is used in electrochemical cells such as fuel cells and batteries, to understand the interfaces between the electrode and the electrolyte, and the interfaces of multilayers of the electrode, which will be introduced in Section 5.5.

5.4. Energy band structure and optical properties

As stated, both blackening processes and modification strategies can shift the valence band (VB) location of pristine material. Investigations of the band structure and the bandgap energy of semiconductors can therefore help not only in understanding the properties of materials, but also to instruct the future rational design of materials for practical applications. The energy bands of a semiconductor mainly include conduction band (CB), VB, Fermi level (E_f), and bandgap (E_g). The E_g of a semiconductor is defined as the gap between the top of the VB (E_v) and the bottom of the CB (E_c), which determines the solar capture and conversion ability of a semiconductor.[236]

To measure the location of the VB maximum, the X-ray photoelectron spectroscopy (XPS) is a common tool such as the measured VB values of both pristine TiO_2 film and B-TiO_x film are 3.13 and 1.94 eV, respectively.[265] In addition, the ultraviolet photoemission spectroscopy is used to confirm the work function (Φ), which is determined by the vacuum level to find the location of E_f that can be calculated according to eqn (1).

$$\Phi = h\nu - E_{\text{cut-off}} \quad (1)$$

The light absorption originated from the electron transmission from VB to CB and then the capacity of light absorption is closely associated with the application potential in solar energy conversion and storage. To measure the light absorption of B-TiO_x samples and to compare the optical properties among different samples in parallel, UV-Vis-NIR absorption/

reflectance spectroscopy can be a suitable technique. For instance, the UV-Vis-NIR absorption spectra of Pt/TiO_2–O_v, and TiO_2 are tested in the wavelength range of 200–800 nm and find that that the light absorbance of Pt/TiO_2–O_v is stronger than that of pristine TiO_2 in the whole wavelength range. If the absorption edge of material is located in a longer wavelength, it will enable a broader light absorption range.[120] Additionally, UV-Vis-NIR plots can estimate the bandgap energy using Tauc's relation along with eqn (2)

$$E_g\,(\mathrm{eV}) = h\upsilon - 1/\beta(\alpha h\upsilon)^{1/n} \quad (2)$$

where β is a constant known as the band tailing parameter, E_g is the energy of the optical band gap and n is the power factor of the transition mode, which is dependent on the crystalline or amorphous nature of the material.

In addition, the incident photon-to-current conversion efficiency (IPCE) recorded with the QE/IPCE measurement system can be used to monitor the ability of the semiconductor converting photons to electrons rather than light absorption – not all absorbed light can be converted into electrons. Typically, a high IPCE value enables a high PEC performance: Ru-doped B-TiO_x has a higher IPCE value in the range of 300–600 nm than TiO_2 that results in a 40-time higher H_2 production rate, 1.91 μmol h^{-1} cm^{-2}, than that of TiO_2.[90] If QE/IPCE equipment is absent, eqn (3) can be used to estimate the IPCE value of the photoelectrode at a given wavelength. Meanwhile, the IPCE is also can used to estimate the bandgap energy according to eqn (4)

$$\mathrm{IPCE}\ (\%) = (I_{\mathrm{ph}} \times h\nu/P \times \lambda) \times 100 \quad (3)$$

where I_{ph} is photocurrent density (mA cm^{-2}), P is the power density of light (mW cm^{-2}), $h\nu$ is the photon energy of the incident light (~1240 eV, nm) and λ is the wavelength of the light (nm).

$$E_g\,(\mathrm{eV}) = (\mathrm{IPCE}\ h\upsilon)^{1/\mathrm{n}} \quad (4)$$

The apparent QE (%) of the H-atom-involved reactions (H_2 evolution reaction and NH_3 generation) can be calculated *via* eqn (5).[296] For example, Li *et al.* reported the QE of Au-supported Fe_3O_4/B-TiO_x under the photocatalytic WS reaction conditions, and reported a QE of 88.7 ± 2.1% at 437 nm.[88] The same group also reported that the QE of a B-TiO_x based photocatalyst can reach 97% at 385 nm for the solar-driven seawater splitting.[297] Another research group has also previously reported a high QE of 46% at 584 nm, achieved in a solar-driven sacrificial H_2 evolution system on a mesoporous B-TiO_x.[298] Recently, it has been demonstrated that H_2 can be generated from methanol on a single-atom-modified TiO_2 photocatalyst, which exhibited a high apparent QE of 99.2% at 365 nm with a high-selectivity production of formaldehyde, leading to a nearly zero- carbon-emission process.[299]

$$E\,(\%) = N_{\mathrm{H}} \times \frac{N(\mathrm{generated\ molecules})}{N(\mathrm{Photons})} \times 100\% \quad (5)$$

where N_{H} is the number of evolved hydrogen atoms and N (Photons) denotes the number of incident photons.

5.5. Semi-conductivity

Semiconductor type (*i.e.*, n-type and p-type), charge carrier density, and charge carrier transport, separation, and recombination rate of B-TiO_x are important for designing and modifying materials towards applications. Surface defects and disorders of B-TiO_x show pronounced effect on physicochemical properties, *i.e.*, in facilitating the electrical conductivity and charge transport, efficiently suppressing the recombination of photoinduced charge carriers. Mott–Schottky (M–S), photoluminescence (PL), time-resolved photoluminescence (TRPL), EIS, *etc.* have been employed to identify such information directly or indirectly.

M–S measurement has often been used to identify the type of semiconductor conductivity and the junctions such as n–p–n junctions and to give information on the charge carrier densities. With respect to the semiconductive type: a straight line with a positive slope from M–S plot indicates a n-type characteristic and a negative slope reflects a p-type feature. The different absolute values of both slopes indicate a spectacular disparity in donor densities.[300] The carrier densities can be calculated in accordance with the eqn (6). For instance, the calculated charge carrier densities of both pristine TiO_2 and B-TiO_x according to eqn (6) are 1.24×10^{19} and 5.55×10^{21} cm^{-3}, respectively.[120] It can be proven that the blackening treatment increases around 2 magnitude orders of the charge carrier densities of TiO_2 which benefits the electrochemical devices.

$$N_{\mathrm{d}} = (2/e_0\varepsilon\varepsilon_0)\,[\mathrm{d}(1/C^2)/\mathrm{d}V] \quad (6)$$

where e_0, ε, ε_0, N_{d}, and $\mathrm{d}(1/C^2)/\mathrm{d}V$ represent the electron charge, the dielectric constant of the material, the permittivity of vacuum, the donor density, and the straight slope, respectively.

The recombination rate of the free charge carriers, *viz*, evaluating the separation and utilization efficiency of the photo-stimulated e^-/h^+ is one of the key parameters in determining their applications.[101] Typically, the e^-/h^+ pair recombination rate of B-TiO_x is lower than that of pristine TiO_2 that will result in a low peak intensity of the B-TiO_x in a PL spectrum.[157] To measure the accurate lifetime of the photoexcited e^-/h^+ pairs, TRPL is needed. For instance, the lifetime of e^- in a B-TiO_x recorded by TRPL is 2.56 ns, which is longer than that in the pristine TiO_2, 1.12 ns.[88]

The electrical conductivity of a semiconductor relates to the mobility of the charger carriers, which is influenced by the parameters of the blackening process and does also impact the performance of electrical devices and photoelectric cells, *i.e.*, supercapacitors.[183,235,301–304] A solid-state conductivity measurement is carried out to measure the resistivities of both pristine TiO_2 and B-TiO_x, 1170.47 and 15.53 kΩ, respectively, confirming a better electrical conductivity of B-TiO_x.[71] This higher electrical conductivity of B-TiO_x over pristine one attracts rising attention in the fields of electrochemistry and photo-electrochemistry.

The charge transfer resistance among interfaces such as the interface between the electrolyte and the electrode often reflects the charge carrier information of B-TiO_x, which is presented in Nyquist plots from EIS tests. In the Nyquist plot, a smaller arc represents a lower resistance at the interface, namely, a higher efficiency of the charge transfer.[107,305]

Herein, B-TiO_x enables a higher charge carrier density, faster separation and utilization efficiency, longer electron lifetime, higher electrical conductivity, and lower interface charge transfer resistance over the pristine one.[13]

5.6. Other characteristics

In addition to the abovementioned properties of B-TiO_x, other information such as chemical structure, phase and polymorph, crystallinity, and molecular interactions with adsorbates can be checked by Raman spectroscopy; the oxidation state and coordination environment of Ti can be determined using XANES technique; the absorption, emission, and photoconductivity of solid, liquid, and gas can be obtained from the Fourier transform infrared spectroscopy. Theoretical understanding are also expected such as the machine learning on PDF analysis for the oxide defect identification through feature extraction and supervised learning.[279]

6. Potential applications

Despite the significant annual market volume of 6 million tonnes for titanium dioxide (TiO_2), commercialization of black titanium oxide (B-TiO_x) has yet to be realized, with ongoing exploration of its potential market applications. The distinctive properties inherent to B-TiO_x underline its recent potential applications in solar energy capture, conversion, and storage devices, presenting promising avenues for utilization in electrical energy storage devices. In this section, the promising applications of B-TiO_x on 9 topics towards sustainable future in both energy and environment will be presented: water splitting, carbon dioxide reduction reaction, ammonia synthesis and decomposition, pollutant degradation, solar thermal energy, supercapacitor, ion battery, fuel cell and others (Scheme 1).

6.1. Water splitting

Water (H_2O) needs a Gibbs energy of 237 kJ mol^{-1} (1.23 V) to be split into H_2 and O_2, and a Gibbs energy of 354 kJ mol^{-1} (1.77 V) to be split into H_2 and H_2O_2, as shown in Fig. 18(b).[306] The energy can be derived from renewables such as solar energy in Fig. 18(a), to assist water splitting (WS) to form renewable H_2 to address the energy crisis.[306] The first report on WS to H_2 and O_2 appeared in 1972 and was tested in a PEC WS cell with a TiO_2 anode (active area, 1.0 cm^2) and a platinum black cathode in an acid solution (pH = 4.7) under light illumination.[307] To the first report on B-TiO_x as the photocatalyst for WS dated back to 2011.[3] Over more than 10 years of development, B-TiO_x and its composites have been studied for WS as photocatalysts, photoelectrocatalysts, and electrocatalysts to produce small molecular chemicals of H_2, O_2, and H_2O_2.[30,40,76,308–322] The progress

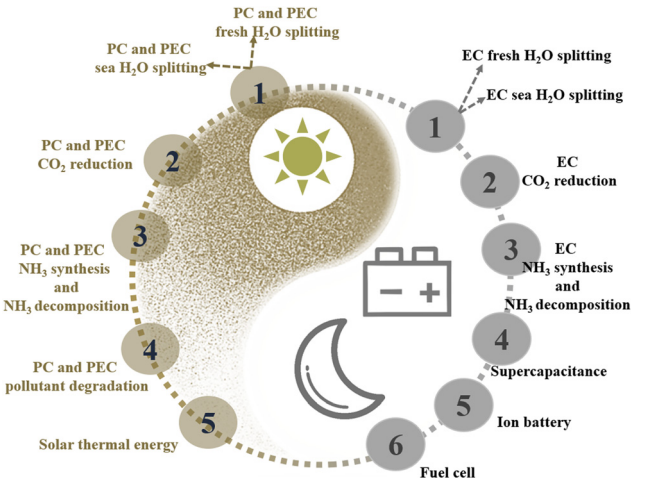

Scheme 1 Potential applications of black titanium oxide under light illumination and bias. PC: Photocatalytic, PEC: Photoelectrocatalytic, EC: Electrocatalytic.

and representative reports on these cells will be addressed in the following.

Water is required among all WS cells, an aspect that has been seldom considered until recently. The concerns arise from the low conductivity of H_2O and the limited amount of fresh H_2O.

(i) The conductivity of water:

Pure H_2O at the standard STP conditions has very limited ionic conductivity, where the conductivity of ultra-pure water is 5.5×10^{-6} S per m (Simens per meter), drinking water is 0.005–0.05 S per m, and sea water is 5 S per m where equilibrium ionic concentration is extremely low.[323] On the other hand, superheated water in sub or supercritical conditions could dramatically increase in ionic concentrations. As a result, WS at high temperature could be useful for exploitation in future since conductivity is important for the performance of both electrolysis and photo-electrolysis WS. The most common way to increase conductivity, is to use inorganic salts (acidic, neutral, and alkaline) such as NaOH/KOH, which are often added into H_2O to improve the ionic conductivity of electrolytes and split of H_2O into H_2/O_2 by electrochemical or photochemical means see Fig. 16(a).[321] Meanwhile, a question is raised on the both beneficial or undesirable effects (*i.e.* surface fouling, cost and scaleup issues) of the pH (the concentration of H^+/OH^-) of the electrolyte on the WS performance. For example, Fig. 16(b) and (c) show the concentration of KOH (1 M, 0.2 M, 0.1 M, and 0.05 M) on both the required electricity to split H_2O and the linear sweep voltammetry (LSV) performance.[324]

(ii) The use of seawater instead of freshwater:

Recently, seawater splitting (*S*WS) has gained increasing attention due to limited availability of fresh water (<1% of earth's water), while sea-H_2O makes up a large proportion (around 96.5% of earth's water).[320,325,326] While direct electrolysis of seawater has witnessed significant advancements, substantial challenges persist.[320,327–329]

Seawater contains a high percentage of aggressive chloride (Cl^-) ions, which requires the use of robust and efficient

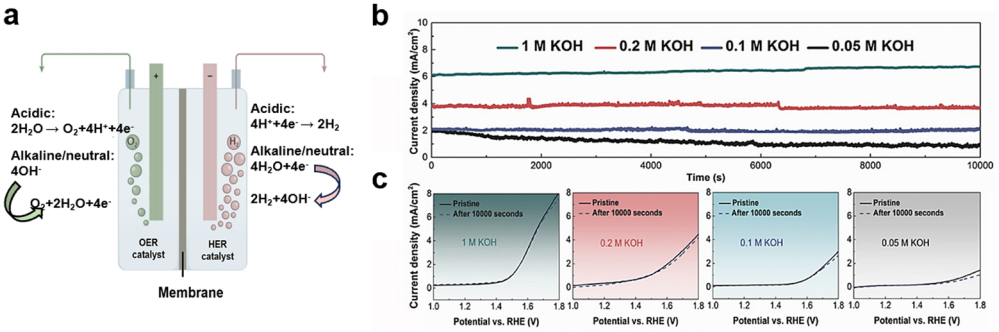

Fig. 16 (a) Schematic of a water electrolyser. Reprinted with permission from ref. 321. Copyright © 2022, Springer Nature Limited (b) Long-term stability tests in different KOH electrolyte concentrations (1, 0.2, 0.1, and 0.05 M) for oxygen evolution process, and (c) Polarization curves of samples in 1, 0.2, 0.1, and 0.05 M KOH before and after 10 000 s time stability tests. Reprinted with permission from ref. 324. © 2017 WILEY-VCH Verlag GmbH & Co. KGaA, Weinheim.

a

Ion	Cl^-	Na^+	SO_4^{2-}	Mg^{2+}	Ca^{2+}	K^+	HCO_3^-	Br^-	$B(OH)_3$	CO_3^{2-}
C (g/kg seawater)	20.058	11.177	2.812	1.331	0.427	0.414	0.112	0.070	0.020	0.016

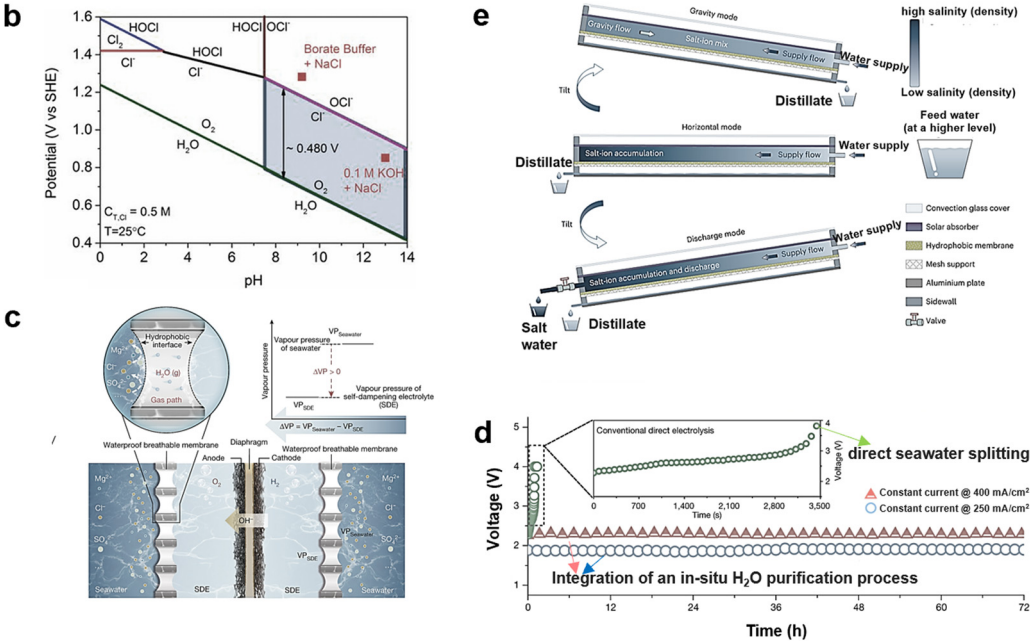

Fig. 17 (a) Table of ion concentrations (*C*) in standard seawater. Reprinted with permission from ref. 325. Copyright © The Royal Society of Chemistry 2021. (b) Pourbaix diagram containing oxygen and Cl^- redox reactions. Reprinted with permission from ref. 330. Copyright © 2016 WILEY-VCH Verlag GmbH & Co. KGaA, Weinheim. (c) Schematic of the integration of the water purification with membranes and water splitting process, and (d) electrolysis durability test at constant current densities of 250 mA cm^{-2} and 400 mA cm^{-2} of 72 h. The inset shows the stability test of conventional direct seawater splitting in seawater with commercial electrocatalysts. Reprinted with permission from ref. 333. Copyright © 2022, The Author(s), under exclusive license to Springer Nature Limited. (e) Schematic diagram of saltwater distillation. Reprinted with permission from ref. 331. Copyright © 2023, The Author(s), under exclusive license to Springer Nature Limited.

catalysts that can withstand Cl^- corrosion, especially for the anode. The relationship between the pH, Cl^- and the voltage are shown in Fig. 17(b): In acid electrolyte, pH < 7, Cl^- would be reduced to Cl_2, in base solution pH > 7, Cl^- would be oxidized to hypochlorite (HOCl or ClO^-).[330] In addition to Cl^-, other main soluble ions in seawater include sulfate (SO_4^{2-}), sodium (Na^+), magnesium (Mg^{2+}), calcium (Ca^{2+}), bicarbonate (HCO_3^-), and potassium (K^+). The corresponding concentrations are listed in the table in Fig. 17(a).[325] These ions might influence the activity and the stability of *S*WS (Fig. 17d). To solve it, in-directly *S*WS cells using membrane (Fig. 17(c)) or using distillation method (Fig. 17(e)) to pre-treat seawater would be solutions.[331] Despite that additional cost and energy requirement will be unavoidable, the in-direct *S*WS combing

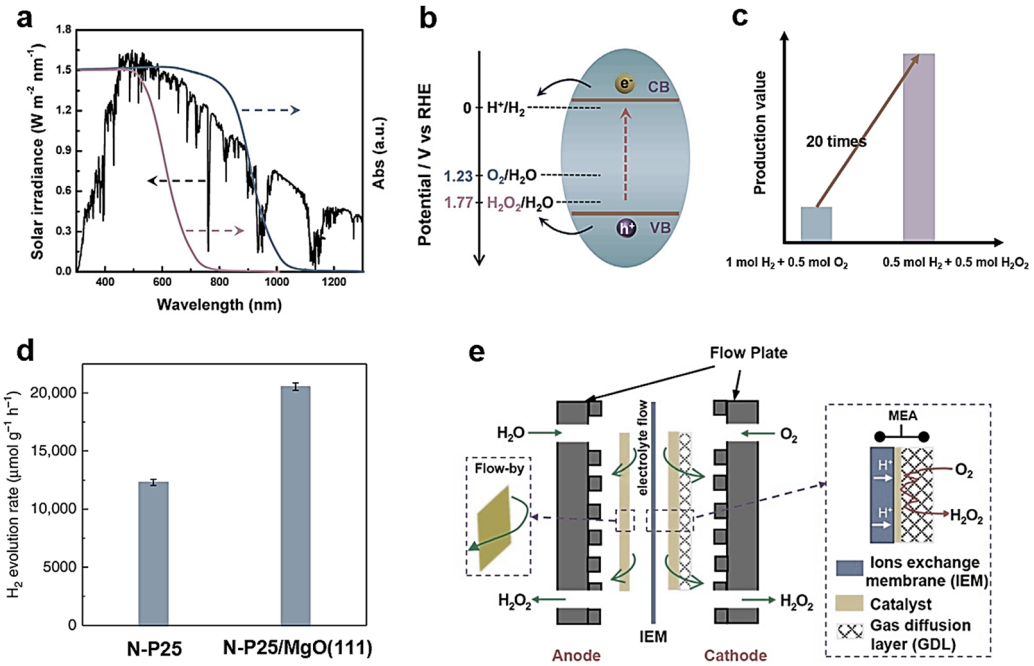

Fig. 18 (a) Light absorption of photocatalysts/photoelectrodes compared with solar spectrum (black) and (b) redox potentials of WS. Reprinted with permission from ref. 306. Copyright © 2022. The Author(s). (c) Comparison of economic benefits from different water oxidation processes. Reprinted with permission from ref. 334. This Copyright © 2019 American Chemical Society. (d) The H_2 evolution rates of N-P25 and N-P25/MgO (111). Error bars indicate the standard deviation. Reprinted with permission from ref. 296. Copyright © 2019. The Author(s). (e) The schematic diagram of the flow-by cell assembled with a gas diffusion electrode and a membrane separator for H_2O_2 production. Reprinted with permission from ref. 335. Copyright © 2021. The Author(s).

seawater purification technologies is still preferred regarding the activity and stability of WS.[332] *e.g.*, in Fig. 17(d), both the activity and stability of the WS cell integrated with a seawater purification process are much better than that of the direct SWS.[333]

6.1.1. Photocatalytic water splitting. In 2011, the inaugural study employed B-TiO_x as a photocatalyst, modified with 0.6 wt% Pt for water splitting (WS), and subsequently tested in an electrolyte comprising a mixture of H_2O and CH_3OH (in a 1 : 1 ratio). The experimentation was conducted under a 1-Sunlight simulator within a Pyrex glass setup, yielding an H_2 production rate of 10 mmol h^{-1} g^{-1}. The methanol in the electrolyte serves as the sacrificial reagent to react with the photogenerated h^+.[3,122,309] In parallel, PCWS has also been investigated using pure H_2O. For example, in Fig. 18(d), N-TiO_2/MgO (111) loading by Au yielded an H_2 production rate of 20 mmol g^{-1} h^{-1}.[296] At present, the state-of-the-art work in PCWS uses Fe_3O_4@SiO_2/B-TiO_x with a loading of 1.0 wt% as photocatalyst, which is carried out under a 1-Sunlight simulator (AM 1.5 G, 100 W cm^{-2}) and an external magnetic field of 180 mT at 270 °C, yielding an H_2 production rate of 21.2 ± 0.52 mmol g^{-1} h^{-1}, which corresponds to an STH of 11.9 ± 0.5%.[88]

Considering the limited freshwater availability (<1% earth's water), PC *S*WS seems more in line with future goal of green H_2 production.[336] In the limited scope of PC *S*WS systems reported so far, the reliance on sacrificial reagents is imperative, giving rise to sustainability concerns and resulting in the generation of carbon-containing by-products. Additionally, the presence of ionic species such as Cl^- and Mg^{2+} in seawater complicates the reaction mechanism, with early attempts revealing adverse effects on photocatalytic performance. Conversely, recent reports highlight that the presence of Cl^- ions can enhance reaction kinetics, thereby improving photocatalytic activity.[337] Evidently, conflicting perspectives on the impact of seawater prevail over this topic, necessitating a clear unraveling of the role of these ionic species and their interactions with catalyst particles. In 2024, Li *et al.* reported on a solar-driven PC *S*WS system for H_2 evolution.[297] The study highlights that photocatalytic performance can be significantly enhanced in natural seawater due to electrolyte-assisted charge polarization over an N-doped TiO_2 photocatalyst. Comprehensive and systematic characterizations, alongside computational studies, indicate that ionic species in seawater can selectively adsorb on photopolarized facets of opposite charge, which can prolong the charge-carrier lifetime by a factor of five particularly at elevated temperature, leading to an overall energy conversion efficiency of 15.9% at 270 °C.

H_2O_2 is an important chemical in *e.g.*, medical, and environmental applications, which can be produced by both H_2O reduction and oxidation. Recently, PCWS to H_2O_2 and H_2 rather than O_2 and H_2, has become increasingly attractive due to (i) the value of H_2O_2 is higher than O_2, (ii) the formation of H_2O_2 is a 2-e^- pathway that can moderate the sluggish of the 4-e^- pathway for O_2 evolution reaction, enabling a high performance of H_2 evolution (Fig. 18(c)).[221,338] An N, S-co-doped graphene

@B-TiO_x catalyst is used to produce H_2O_2 with a rate of 873 μmol L^{-1} h^{-1}.[339] However, the report of B-TiO_x in PC H_2O_2 production is still scarce due to the instability of H_2O_2 under light irradiation, and the low WS reaction selectivity between O_2 and H_2O_2.[335,340]

6.1.2. (Photo)electrochemical water splitting

Photoanode and anode. B-TiO_x stands as the pioneering and predominantly embraced catalyst for photoanodes in water-splitting (WS) cells. The first report using B-TiO_x as a photoanode for water oxidation reaction (WOR) to O_2 in a PECWS cell was appeared in 2011.[341] In that work, the photoanode was made of the B-TiO_x nanowire/FTO glass without loading noble metal with an active area of 0.20–0.25 cm^2, which was tested in 1 M NaOH (pH = 13.6) under the 1-Sunlight simulator, AM 1.5 G, 100 mW cm^{-2}. The photocurrent density at 0.4 V_{RHE} (Volt *versus* the reversible hydrogen electrode) is 1.97 mA cm^{-2} corresponding to an SHT of 1.63%, and the photocurrent density at 1.23 V_{RHE} is 2.8 mA cm^{-2}. Currently, the state-of-the-art photoanode composed of B-TiO_x for WS is B-$BiVO_4$/B-TiO_x with an active area of 1.5 cm^2. The photocurrent density is 6.12 mA cm^{-2} at 1.23 V_{RHE} measured in an electrolyte of 0.5 M potassium phosphate buffered to pH = 7 under 1-Sunlight simulator, AM 1.5 G, 100 mW cm^{-1}.[215] It is noteworthy that the reporting of the active areas for both photoanodes and photocathodes is crucial, as these two dimensions significantly impact the overall performance.

Very recently, B-TiO_x has been used to stabilize the Ru sites through structural-confinement and charge-redistribution for WOR, which extends the catalyst lifetime in a 0.5 M H_2SO_4 solution (pH = 0.3) by 10 orders of magnitude longer than that of commercial (com.) RuO_2/TiO_2 and better than com. IrO_2/TiO_2 (Fig. 19a).[269] As shown in Fig. 19(b), Ru/TiO_x retains stable for a 900-h test at @10 mA cm^{-2} with an overpotential of 174 mV, which is better than reported values shown in Fig. 19(c) in both activity and stability. Meanwhile, the safeguard function from TiO_x is further confirmed from comparing the Ru retention rate (%) among Ru/TiO_x, RuO_x/TiO_2, and RuO_2/TiO_2, 97.3%, 42.2%, and 20.7%, respectively.[269] The theoretical calculations are further used to confirm that TiO_x stabilizes the Ru active center from the introduction of O_v.

Photocathode and cathode. There is a limited number of publications utilizing B-TiO_x as a (photo)cathode in water-splitting (WS) cells. This scarcity can be attributed to the inherent instability of metal oxides in the coexisting environment of cathodic potential, initial atomic hydrogen (H*), and gaseous H_2.[196,222] However, very recently, B-TiO_x (photo)-cathode has shown remarkable progress in both the activity and the stability in WS cells for the H_2 evolution reaction. Hou *et al.* proposed a multi-step reduction method to form B-TiO_x, named R-TNT, which is then directly used as (photo)cathode in a WS cell to produce H_2 with a geometric area of 1 cm^2.[342] The overall current of R-TNT is −221 mA at −1.0 V_{RHE}, which is 17 000-times higher than that of pristine TiO_2 (TNT). The long-term stability is carried out at chronopotentiometry (CP) mode of −100, −50, and −10 mA, sequentially, with a decay of 1.3%, 5.2%, and 18.4%.

In terms of the production of H_2O_2 in PEC/EC cells, both theoretical and experimental investigations have been carried out intensively, also included in recent thorough reviews.[335,343] In an electrochemical cell, both WOR and water reduction reaction (WRR) can be carried out to form H_2O_2, as shown in Fig. 18(e).[334,335,344] B-TiO_x can work as both the anode catalyst for the WOR to H_2O_2 and as the cathode catalyst for the WRR to

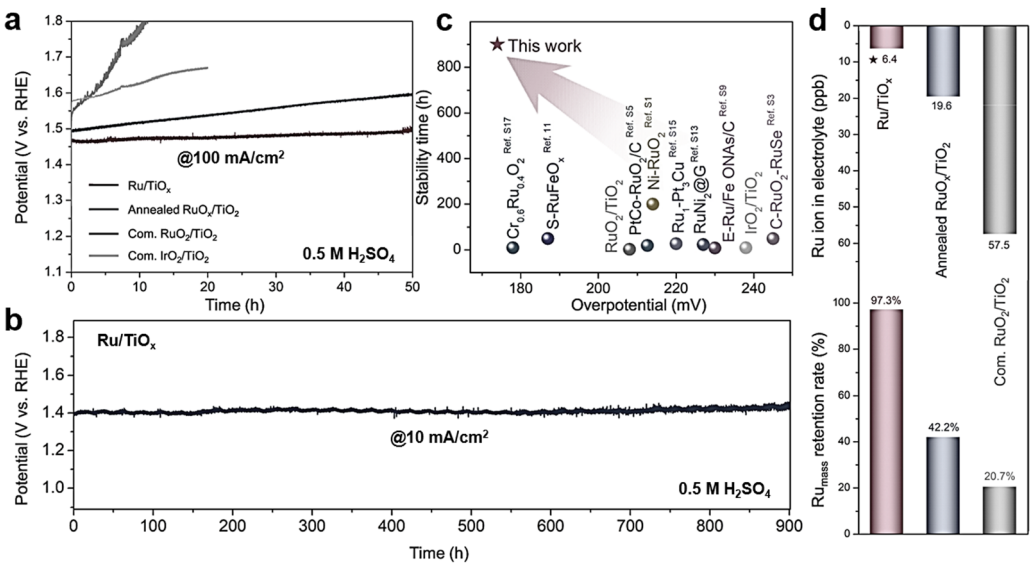

Fig. 19 (a) Chronoamperometric (CP) curves (No *iR* compensated) of samples of Ru/TiO_x, annealed RuO_x/TiO_2, com. RuO_2/TiO_2 and com. IrO_2/TiO_2 for OER at 100 mA cm^{-2} for 50 h, respectively. (b) CP curve of Ru/TiO_x for OER at 10 mA cm^{-2} for 900 h. (c) The overpotentials and durations of stability of Ru/TiO_x and state-of-the-art electrocatalysts in for oxygen evolution reaction in acidic media. (d) Inductively coupled plasma-mass spectrometry (ICP-MS) analysis for dissolved Ru ions in electrolyte and Ru mass percentage retained in Ru/TiO_x, annealed RuO_x/TiO_2 and com. RuO_2/TiO_2 catalyst after the CP test. Reprinted with permission from ref. 269. Copyright © 2023, The Author(s).

H_2O_2, which enables high faradaic efficiency of over 100%.[193,345,346] For instance, a catalyst of (1T-2H)-$MoSe_2$/B-TiO_x is constructed for WOR to produce H_2O_2 with a rate of 57 μM h^{-1}. A composite of B-TiO_x/TiC needs an overpotential of *ca.*10 mV to form H_2O_2 with an H_2O_2 production rate of 7.19 mol g^{-1} h^{-1} at 0.3 V_{RHE} and an H_2O_2 selectivity of 94.1% at 0.5 V_{RHE}.[347] In future, bifunctional B-TiO_x catalysts are foreseen to be designed to function WOR and WRR simultaneously for H_2O_2 for a high faradaic efficiency and a high yield. In 2022, one PEC *S*WS is demonstrated using Au-Gd-Co_2B@TiO_2 electrocatalyst, which requires an overpotential of 510 mV to reach 1000 mA cm^{-2} in alkaline seawater. The high activity of Au–Gd–Co_2B@TiO_2 is assigned to the high concentration of O_v at the interface of Co-Au surface. To date, research reports on B-TiO_x for seawater splitting are still limited.[348]

6.2. Carbon dioxide reduction

The emission of excessive carbon dioxide (CO_2) into the atmosphere leads to subtle climate change, manifesting in phenomena including the global warming. Currently, the amount of CO_2 released in atmosphere is still increasing: The global energy-related CO_2 emissions was 36.8 Gt that grew by 0.9% in 2022, and September 2023 is the warmest September since 1880 so far, which shows a global average surface temperature 1.72 °C above that during the years of 1880–1920.[349] Confronting this challenge, extensive research efforts have been devoted to the investigation and development of CO_2 capture and conversion techniques for its direct or indirect utilization (Fig. 20(a)).[350] Various approaches, including thermochemical, electrochemical, bio-electrochemical, and photocatalytic CO_2 reduction reaction (CO_2 RR), have been explored to transform CO_2 into value-added carbon products such as CO,[126,351,352] CH_4,[65,351,353–355] CH_3OH,[353,356–360] HCOOH,[359,361] C_2H_5OH,[360,361] CH_3CHO,[362] CH_3COOH,[359] *etc.* A flowchart in Fig. 20(b) shows the combination of photocatalytic CO_2 RR and carbonylation reaction to produce fine chemicals or drugs.[363] These different carbon-based chemicals from CO_2 RR require different energy inputs corresponding to their thermodynamics (Fig. 20(c)), *i.e.*, which can be provided from batteries or solar cells generated from renewables.[364,365]

The utilization of B-TiO_x in CO_2 RR has witnessed a significant surge, particularly in photocatalytic (PC) and photoelectrolytic (PEC) processes, which is attributable to its advantageous properties in efficiently capturing solar energy and fine-tuning energy bands.[32,34,367–369] An latest review on B-TiO_x based materials for photocatalytic CO_2 RR was presented in 2022.[34]

The photocatalytic CO_2 RR mechanism displayed in Fig. 20(c) shows the absorption of photons, and the generation of charge carries.[364] Similar with PCWS, the migrating e^- can reduce the adsorbed CO_2 into valuable carbon products, and along with the required potential energies for these redox (E_v *vs.* NHE at pH = 7), while h^+ will oxidize H_2O to O_2. The PEC CO_2 RR cell (Fig. 20(e)) produces carbon fuels and O_2 in photocathode and photoanode *via* CO_2 RR and HOR, respectively.[366] When compared with PC CO_2 RR, PEC CO_2 RR has more choices in semiconductors in tuning their band position of B-TiO_x, which can better meet the requirement of suitable band states and redox potential for CO_2 RR with the assistance of an external bias. When compared to EC CO_2 RR (Fig. 20(d)), PEC can decrease the overpotentials toward CO_2 RR under light irradiation and can provide better control over product selectivity.[366] For example, a PEC H-cell is integrated with a TiO_2 anode for WOR to O_2 and a Pt-reduced graphene oxide cathode for CO_2 RR into HCOOH, which uses both solar energy and renewable electricity as the driving force. The photovoltage provided by the anode can compensate and confer cathodic potential for CO_2 RR by maintaining the reactions taking place on both electrodes' surfaces.[361] It is worth noting that in both PC and PEC CO_2 RR in using B-TiO_x, the conduction band (CB) position must be situated below the reduction potential of CO_2/carbon products. This arrangement is essential for the activation of CO_2 and cleavage of C=O bonds. Simultaneously, the valence band (VB) position of B-TiO_x should be above the oxidation potential of H_2O (refer to Fig. 20(c)). In other words, the B-TiO_x and its composites should possess a suitable band structure for both PC and PEC CO_2 RR.[370]

The complex CO_2 photoreduction procedures make a substantial difference to their experimental activity and selectivity. In terms of the experimental activity, it is important to design effective B-TiO_x based materials combining modification strategies such as doping and defect engineering to simultaneously boost CO_2 RR without any sacrificial reagents. Besides, energy inputs (*i.e.*, external potential) should be tuned to realize CO_2 RR at reasonable rates. Aside from B-TiO_x, the CO_2 RR performance is also largely influenced by the concentration of reactants, the adsorption of intermediates, reaction pathways, the electrolyte proton availability, *etc.* For example, neutral and alkaline pH solutions are preferred to improve the kinetics of CO_2 RR and to avoid the HER because of the prevalence of H^+ ions in acidic conditions. Catalysts with high overpotential for HER and a contrarily lower overpotential for CO_2 RR are desirable. Moreover, there is a wide range of carbon products from CO_2 RR, commonly low molecular weight hydrocarbons with 1–4 carbon atoms C_1-C_4. Meeting market demand, as outlined in Table 3, and concurrently reducing the cost of separating carbon chemicals underscores the importance of achieving high selectivity in CO_2 RR towards specific target products.[371]

For CO_2 RR, both the reactant molecule adsorption and the chemical bonds activation are very critical.[372–374] As mentioned, B-TiO_x has many surface defects such as Ti^{3+} species, O_v, *etc.*, which can potentially serve as both adsorption and activation sites for the CO_2 molecule leading to potential reduction reactions. For instance, Funk *et al.* reported that CO_2 adsorption decreases with increasing defect density of O_v and increases with increasing O_2 re-exposure, and also pointed that the defects are the active sites for breaking bonds of reactants of adsorbed O_2 and H_2O.[373] Meanwhile, the adsorption geometry of CO_2 and O_v can critically affect the CO_2 RR pathway to diverse products. The CO_2 adsorbed on O_v sterically inhibits the attack of the proton to the carbon. Therefore, the most feasible reaction pathway for the CO_2 undergoing this

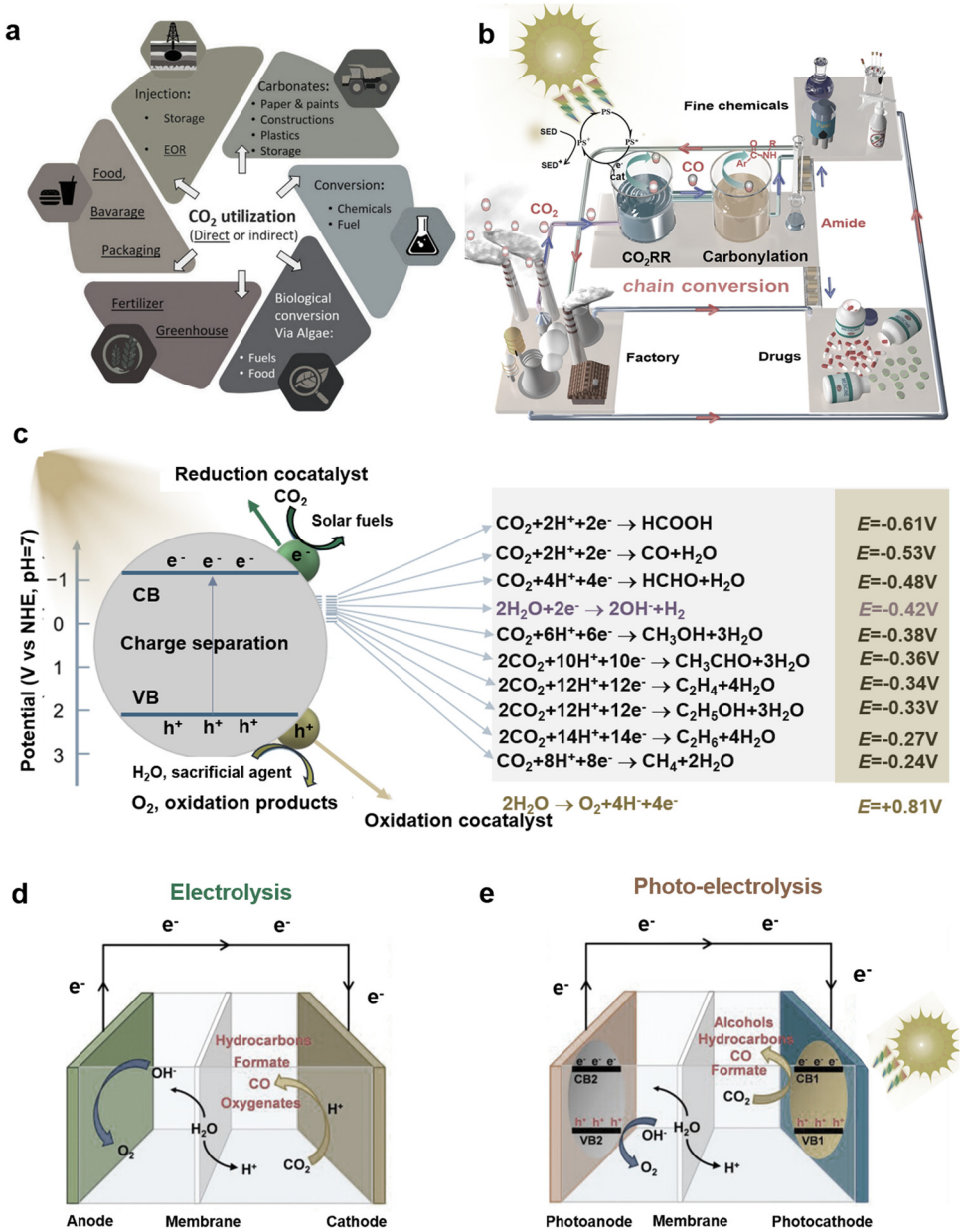

Fig. 20 (a) Schematic of direct and indirect utilization of CO. Reprinted with permission from ref. 350. This article is licensed under a Creative Commons Attribution 3.0 License. (b) Schematic illustration of photocatalytic CO_2 RR and carbonylation reaction for the utilization of that reduction carbon product. Reprinted with permission from ref. 363. Copyright © 2022, The Author(s). (c) Schematic illustration of required potential energy for photocatalytic CO_2 RR for solar fuels and H_2O oxidation reaction. Reprinted with permission from ref. 364. Copyright © 2022, The Author(s) under exclusive license to Tianjin University and Springer-Verlag GmbH Germany, part of Springer Nature. (d) and (e) Schematic illustration of the working principles of the electrolysis CO_2 conversion cell and the photo-electrolysis CO_2 conversion cell. Reprinted with permission from ref. 366. © 2022 The Authors. Advanced Science published by Wiley-VCH GmbH.

adsorption mode is the deoxygenation into CO. While, the hydride-like Ti–H–Ti enables TiO_2 to act as a hydride reagent during the photocatalytic CO_2 RR to preferentially generate formic acid.[374]

The reaction pathway is contingent upon the catalysts and prevailing reaction conditions, giving rise to notably diverse product distributions. Understanding the generation of these different types of carbonaceous compounds is important for designing catalysts with a high selectivity such as toward the propane rather than ethane.[375–377] One example of such a reaction pathway for CO_2 RR is shown in Fig. 21 CO_2 RR involving e^- and H^+, and thus the rate-determining steps of these products are governed by the e^- or H^+ transfer in 9 different ways. CO and HCOOH are produced by the transfer of $2e^-$ and H^+, CH_3OH and CH_4 formations require 6 and $8e^-$ and H^+, and the production of CH_3CH_2OH needs $12e^-$ and H^+ for the reaction with $CO_2^{\bullet-}$intermediate. Besides, the reaction mechanism of multistep intermediates to final products plays a

Table 3 Industrial values and market prices of several carbon fuel products. Reprinted with permission from ref. 371. © 2022 The Authors. Published by Elsevier Inc

	Products	Industrial values	Market prices ($$ per kg)
C_1	Carbon monoxide	Fischer–Tropsch synthesis	0.06
	Methane	Combustion fuel, dry reforming to syngas	0.18
	Methanol	Gasoline additive, direct methanol fuel cell	0.58
	Formic acid	Direct formic-acid fuel cell	0.74
C_{2+}	Ethylene	Polyethylene and ethylene glycol production	1.3
	Ethane	Ethylene production	0.26
	Propane	Domestic combustion fuel	0.9
	Ethanol	Chemical solvent and fuel, medical use	1.0
	Ethylene glycol	Poly(ethylene terephthalate) production	0.75
	Diesel	Aviation fuel	1.42
	Gasoline	Fuel for internal combustion engines	1.32

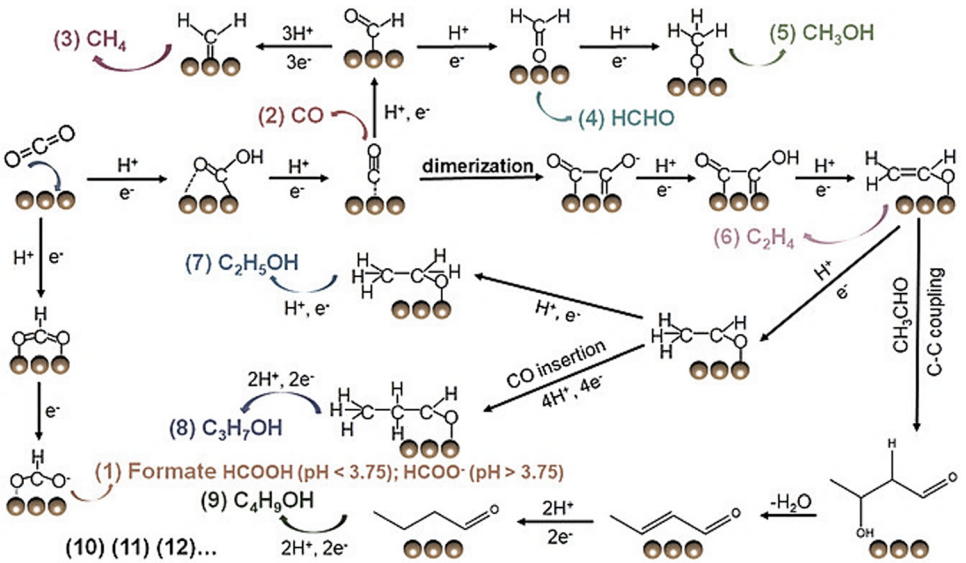

Fig. 21 Possible CO_2 reduction reaction (CO_2 RR) pathways for the hydrocarbons. Reprinted with permission from ref. 366. © 2022 The Authors. Advanced Science published by Wiley-VCH GmbH.

key role in breaking through the kinetics bottleneck. It is generally believed that the pathway and selectivity of the final products are relative to the interaction of surface adsorbates, the replenishment of e^- and H^+, and the step of hydrogenation and deoxygenation, while product selectivity would decrease dramatically when generating the molecules that require more e^-.[208] For example, the formation of CH_4 (−0.24 V) is thermodynamically more feasible than that of CO (−0.53 V), which means that if sufficient e^- and H^+ are provided, the formation of CH_4 will be preferred. On the other hand, surface structure, morphology, composition, CB location, *etc.* of B-TiO_x catalysts and applied external voltage can affect both the overall selectivity and the activity of the CO_2 RR.[356,378–380] Another case is the CO_2 RR into CO and CH_4, where the MoS_2/TiO_2 composition give production rates of 1.6 μmol g^{-1} h^{-1} for CH_4 and 3.3 μmol g^{-1} h^{-1} for CO; whereas under the same conditions, the pristine TiO_2 give 6.7 μmol g^{-1} h^{-1} for CH_4 and 0.9 μmol g^{-1} h^{-1} for CO.[226] The effect of the atmosphere (air and inert condition) and the temperature (300 °C, 450 °C and 600 °C) during the post-annealing of TiO_2 on the performance of photocatalytic CO_2 RR to CO is investigated, giving production rates of 59.54 (air, 450 °C), 172.61 (reductive condition, 300 °C), 179.97 (reductive condition, 450 °C) and 185.39 μmol g^{-1} h^{-1} (reductive condition, 600 °C).[126]

Recently, TiO_2 as a kind of reducible oxide has regained attention from the CO_2 hydrogenation pathway. In 2023, Monai *et al.* presented a study elucidating the reconstruction of Ni/TiO_x catalysts. This involved complete removal of TiO_x under CO/CO_2 hydrogenation conditions at 400 °C (refer to Fig. 22(a)). Interestingly, the process led to the establishment of interfacial sites featuring Ni–TiO_x, identified as strong metal-support interaction (SMSI), during the reaction at 600 °C (refer to Fig. 22(c)). This SMSI phenomenon was found to enhance C–C coupling by providing a reservoir for C-species, thereby augmenting C–C coupling activity. The catalytic CO/CO_2 hydrogenation performances over 400 °C/600 °C–Ni/TiO_2 catalysts were tested at 200–400 °C under 5 bar and shown in Fig. 22(a) and (b). 400-Ni/TiO_2 sample gives a higher overall catalytic activity, C1 in Fig. 22(c), C_2-C_4 in Fig. 22(d), and total yield in Fig. 22(f), but lower C_1 (Fig. 22c) and obviously lower C_2-C_4 (Fig. 22d) stability over 600-Ni/TiO_2. Meanwhile, the selectivity

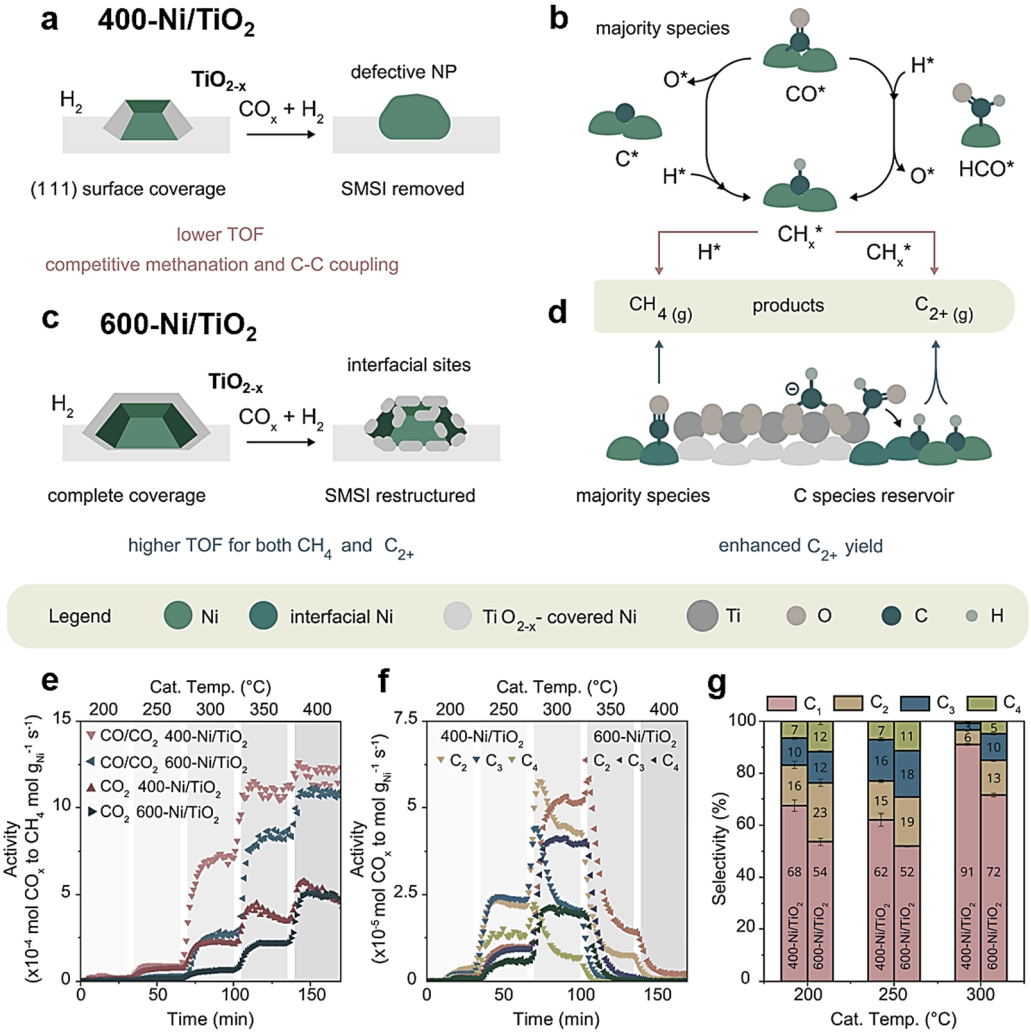

Fig. 22 Model for TiO_x overlayer formation after 400 and 600 °C reduction and restructuring under reaction conditions (a) 400 °C reduction, (b) the hydrogenation reaction mechanism on 400-Ni/TiO_2, (c) 600 °C reduction, and (d) the hydrogenation reaction mechanism on 600-Ni/TiO_2. (e) Catalytic activity for CO_2 (dark shade) and CO/CO_2 methanation (light shade), (f) C–C coupling activity in the CO/CO_2 hydrogenation reaction, and (g) selectivity to hydrocarbons (C_1–C_4) in the CO/CO_2 hydrogenation reaction over 400-Ni/TiO_2 and 600-Ni/TiO_2. Reprinted with permission from ref. 83. Copyright © 2023, The American Association for the Advancement of Science.

of C_{2+} is 14–20% higher under the CO/CO_2 hydrogenation experiments at 200, 250, and 300°C for 600-Ni/TiO_2 catalyst because of the formed interface between Ni and TiO_x.[83]

6.3. Ammonia synthesis and decomposition

The atmospheric dinitrogen (N_2) can be fixed into ammonia (NH_3), nitric oxide, and nitrogen dioxide.[381–385] Among them, NH_3, as the second most produced chemical in human society, is an important raw material to produce fertilizers, plastics, explosives, nitric acids, and intermediates for dyes and pharmaceuticals. In addition, NH_3 is anticipated to be the most promising future energy carrier since it contains no carbon in its molecule with high hydrogen content. To synthesize NH_3, conventional Haber–Bosch (H–B) process has been employed under an elevated temperature of around 400 °C and an elevated pressure of around 150 bar, which gives an annual global production of more than 170 Mt (235 Mt in 2021), along with the consumption of about 1.0% of total world energy production and the 1.4% of global CO_2 emission. To moderate the energy and environmental issues in the H–B process, new routes have been intensively studied to synthesize green NH_3 such as (photo)electrosynthesis of NH_3.[386–390]

NH_3 has been considered as a H_2 carrier for the transportation and storage of H_2 at high quantity, which is instead of employing a direct transport and storage of compressed H_2 gas or liquid-H_2 with inferior hydrogen carrying capacity. There are several advantages to use NH_3 as a medium (i) the annual global production of NH_3 is large, (ii) liquefication of NH_3 requires only a pressure of 8.6 bar at 20 °C, much lower than 700 bar at 25 °C for H_2, (iii) NH_3 has a high hydrogen capacity, 121 kg H_2 m^{-3} at 10 bar, and a gravimetric hydrogen density of 17.8 wt%, *etc.*

In this part, we will present the recent progresses in both NH_3 synthesis and NH_3 decomposition using B-TiO_x as the

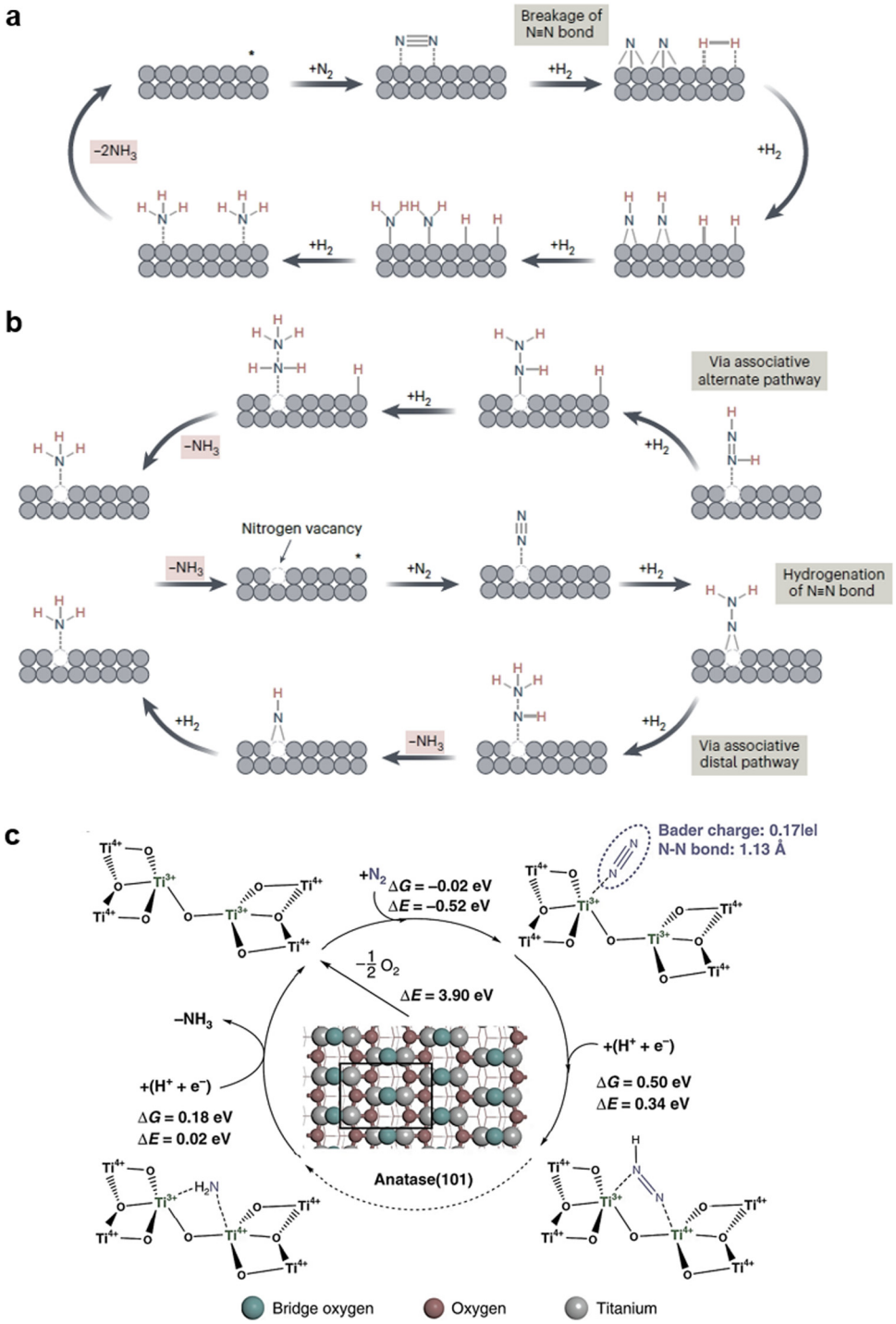

Fig. 23 Mechanisms for ammonia synthesis: (a) dissociation mechanism, and (b) association mechanism, showing the distal pathway (H on the distal N) and alternating pathway (H on both the distal N and the N proximal to the surface site). The reactions initiate at '*'. Reprinted with permission from ref. 392. Copyright © 2023, Springer Nature Limited. (c) Single Ti^{3+} on anatase TiO_2 (101) surfaces with O_v for ammonia synthesis. ΔG refers to the free energy, and ΔE refers to the electronic energy. Reprinted with permission from ref. 394. Copyright © 2019, The Author(s).

catalyst, with a focus of cycling NH_3 for energy transport using renewable energy sources such as solar power.

6.3.1. Ammonia synthesis. Although the N_2 reduction reaction (NRR) to NH_3 is more favorable than H_2 evolution reaction from thermodynamic considerations, N_2 dissociation needs extremely high kinetic barrier to overcome (Fig. 24a). For example, Fig. 24(a) shows a potential of −3.2 V *vs.* NHE at pH = 0 to activate N_2 with H^+.[391] Accordingly, active sites are required to reduce the activation barrier and renewables such as solar energy are needed to establish the required

conditions for the N_2 activation *i.e.* using extreme temperature/pressure.

Even though new pathways in synthesis of NH_3 has been intensively studied to lower the energy consumption and reduce CO_2 emission, currently, about 90% of NH_3 production still relies on the H–B process. The NH_3 synthesis *via* H–B process is understood to follow the dissociative mechanism shown in Fig. 23(a). The first step of the H–B process is the breakage of the N≡N bond that is also the rate-limiting step of N_2 dissociation on the metal sites, followed by subsequent hydrogenation of atomic N to form NH_3 before desorbing form the surface.[392,393] In contrast, new approaches for the synthesis of NH_3 are inspired by the biological enzymes that conduct N_2 fixation under mild conditions, which is adopted the associative pathway where the cleavage of N_2 is not rate-limiting step. Both experimental studies and DFT calculations show that the fixation of N_2 to produce NH_3 can proceed *via* the associative mechanism with the addition of protons proceeds by the distal pathway and the alternating pathway, in Fig. 23(b), and the details has been well discussed by Ye and Tsang in 2023.[392]

Both Ti^{3+} and O_v can serve as active sites (*i.e.*, nitrogen-adsorption sites) to increase the donation of electrons to the anti-bonding π^* orbitals of N_2, and then to effectively weaken and promote the cleavage of the N≡N bonds.[394,395] For instance, Li *et al.* reported that the O_v favoring the chemisorption and activation of N_2 and the formation of Ti^{3+}. Meanwhile, Cao *et al.* revealed that adjacent bi-Ti^{3+} sites on anatase TiO_2 (101) can chemisorb and active N_2 molecules, but both bi-Ti^{3+} sites on rutile TiO_2 (110) and single and isolated Ti^{3+} on anatase TiO_2 (101) cannot.[394] In terms of the reaction mechanism of B-TiO_x for NH_3 formation, in general, it follows the distal pathway, where hydrogenation takes place on the adsorbed N atoms without previous cleavage of N≡N but to form *NH_x intermediates directly (Fig. 23c).[393,394] As a result, the NH_3 synthesis can be operated under mild conditions.

In addition, the B-TiO_x discussed in this review exhibits promise in both solar energy capture and the regulation of Ti^{3+} and O_v concentrations through various strategies (see Fig. 24(b)).[394] This versatility is advantageous for the photoreduction of N_2, even under ambient conditions, with the added benefit of no CO_2 emission.[107,115,133,181,396–401] For example, a bamboo-like B-TiO_x film offers large surface area and O_v. Even without loading of noble-metal co-catalysts, the film can be used for fixing N_2 into NH_3 under ambient conditions driven by Vis-NIR light, yielding an NH_3 generation rate of 48.3 mg m^{-2} h^{-1}, *viz*, 178 μmol g^{-1} h^{-1}.[107] As shown in Fig. 24(c), the apparent QE (%) values of B-TiO_x are measured at monochromatic wavelengths of 365, 405, 450, 532, 650, and 780 nm, delivering values at 0.39%, 0.12%, 0.11%, 0.15%, 0.24%, and 0.07%, respectively. At the same time, the QE% curve indicates that the synthesis of NH_3 can be triggered at visible wavelengths longer than the absorption edge of pristine TiO_2 at *ca.* 400 nm.[107] The concept of lattice strain and geometry-modified nanoreactors, B-TiO_x nanotubes, is interestingly demonstrated in the synthesis of

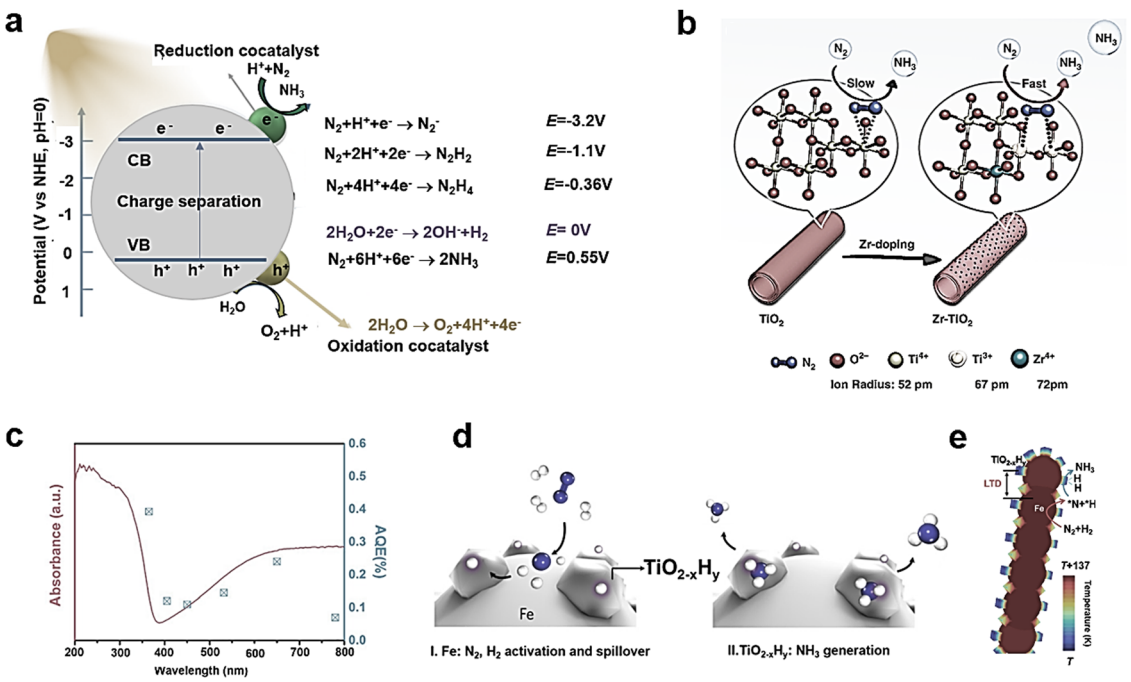

Fig. 24 (a) Schematic illustration of required potential energy for photocatalytic nitrogen reduction reactions and a water oxidation reaction. Reprinted with permission from ref. 391. Copyright © 2021 Elsevier Inc. (b) The formation of O_v and Ti^{3+} sites on the Zr-doping TiO_2 for NH_3 synthesis. Reprinted with permission from ref. 394. Copyright © 2019, The Author(s). (c) The apparent QE% of NH_3 evolution using B-TiO_x under the monochromatic lamp irradiation at different wavelengths. Reprinted with permission from ref. 107. Copyright © 2020 Elsevier B.V. All rights reserved. (d) Diagram of N_2 and H_2 activation and H transfer for NH_3 generation over $TiO_{2-x}H_y$/Fe catalyst. Reprinted with permission from ref. 280. Copyright © 2020, American Chemical Society. (e) Local temperature difference of illuminated $TiO_{2-x}H_y$/Fe steady-state non-equilibrium temperature distribution at 726 nm and the proposed dual-temperature-zone NH_3 synthesis of $TiO_{2-x}H_y$/Fe. Reprinted with permission from ref. 402. Copyright © 2019 Elsevier Inc.

NH_3, which reports a generation rate of 5.50 μg h^{-1} cm^{-2} (16.67 μg h^{-1} mg^{-1}) and a FE(%) of 26% under ambient aqueous conditions.[115] In efforts to enhance the yield rate of NH_3, reported strategies include the utilization of Ru single atoms to modify B-TiO_x, resulting in a notable rate of 22.2 mol g^{-1} h^{-1} in the reduction of NO_3^- to NH_3.[176] Intriguingly, a dual temperature zone catalyst of $TiO_{2-x}H_y$/Fe (Scheme in Fig. 24(d)), was designed to effectively synthesis of NH_3, where Fe as the hot zone to activate N_2 and $TiO_{2-x}H_y$ as the cooling zone to hydrogenate N to NH_3 relying on its O_v.[280] Under solar illumination, the apparent temperature of $TiO_{2-x}H_y$/Fe reaches 495 °C but with local temperature difference up to 137 °C between the Fe and $TiO_{2-x}H_y$ owing to the plasmonic local heating (Fig. 24(e)). The designed catalysts have surpassed the yields achievable through thermal catalysis in the solar-driven synthesis of NH_3.[402]

6.3.2. Ammonia decomposition. NH_3 as a medium for H_2 transport and storage shows its importance to the recent green H_2 technologies.[392] Thus, NH_3 decomposition to H_2 with low energy cost and high H_2 purity has attracted increasing investigations.[403] While several reports employ TiO_2 or doped TiO_2 as support for transition or noble metals in catalytic ammonia decomposition, there is currently no documented reference of directly utilizing B- TiO_2 for this reaction.

6.4. Environmental pollutant treatment

The degradation of both inorganic and organic pollutants such as organic dyes and toxic gas of carbon monoxide (CO), holds significant importance in addressing environmental challenges.[404–411] Toxic gases purification is becoming a distinctly growing concern. This process often involves gas capture and catalytic degradation, the B-TiO_x based materials are unfortunately not suited for gas capture. Thus, we focus on the summary on the degradation of pollutants in liquid solutions that is categorized into advanced oxidation process (AOP) and advanced reduction process (ARP). The AOP has been intensively studied using free radicals to degrade pollutants, meanwhile, ARP has been used as a new approach for removing oxidative pollutants from aqueous solution for water cleaning.[412]

B-TiO_x, as an environmentally friendly material, has been an attractive candidate for both AOP and ARP processes,[37,113,409–411] and also earns bonuses from its advantages, such as high absorption capacity in a broad wavelength range.

6.4.1. Advanced oxidation process. B-TiO_x has been a promising catalyst for the degradation of both organic pollutants such as methylene blue (MB) and rhodium boride (RhB), and inorganic pollutants such as Cr (VI) during AOP. This replies on surface defects functioning as traps, reducing e/h recombination and forming mid-gap/localized-donor states, which eventually narrows the band gap.[95,128,197,228,412–415] The reaction kinetics, mechanisms, and performances of using B-TiO_x in AOP have been studied. For example, the Co–B-TiO_x catalyst can activate peroxymonosulfate (PMS), leading to the formation of the radical $SO_4^{\bullet-}$ as a principal oxidant for the degradation of 4-chlorophenol (4-CP). In terms of degradation rate and efficiency of 4-CP among TiO_2, B-TiO_x, Co–TiO_2, and Co–B-TiO_x, the latter gave the best performance for the degradation of 4-CP with the highest Cl^- production rate.[89] Hou *et al.* investigated the degradation rates of MB, RhB, and Cr(VI) by tuning the concentration of Ti^{3+} of B-TiO_x samples and found that B-TiO_x modified with 0.05 g KBH_4 (B-TNT-0.05) achieved the highest PEC dye removal efficiency. In addition, it proved that the suitable concentration of Ti^{3+} (or reduction chemicals) is important to the overall performance.[136]

Beyond surface defects, the difference between PEC and PC techniques for the degradation of pollutants, such as MB, RhB, and Cr (VI), using the same B-TiO_x catalyst has been discussed. It confirmed that the PEC removal efficiencies are higher than that of PC ones because of the additional power from external voltage.[117] With respect to the high performance of the PEC process, the working principle has been addressed and can be divided into two regimes according to the applied potential: (i) at low bias, it worked as the electro-assisted photocatalysis; (ii) at high bias, it worked as a combination of electro-assisted photocatalysis and electrochemical oxidation.[117] A PEC degradation mechanism (Fig. 25(a)) has been proposed that Ti^{3+} serves as the active species for tetracycline (TC) degradation, while, the visible-light light capture can be effectively enhanced from both the unique nanotubes, the narrowed bandgap, and the junctions in enhancement of visible-light harvesting ability.[416]The proposed TC degradation pathway is displayed in Fig. 25(b), but we would like to stress the importance of $^{\bullet}O_2^-$ and h^+ for the oxidation of TC, *via* continuously attacking TC and intermediate products such as P4 and P5.[416]

6.4.2. Advanced reduction process. On the basis of the ARP process, the B-TiO_x films have been employed to treat Cr(VI) in the leather wastewater. Under visible light irradiation (100 mW cm^{-2}, 300 W Xe light with 420 nm cut-filter) with unadjusted pH, they gave a Cr(VI) reduction rate of 96.2%, which is higher than the 56.3% of commercial P25.[417,418] However, the database of this process is still limited to provide a broad range analysis in parallel.

6.5. Solar thermal energy

Solar thermal energy (STE) involves harnessing solar energy to generate thermal energy, which finds applications in both industrial and residential sectors. Examples include solar cookers and solar-driven interfacial water evaporation systems.[419]

Undoubtedly, a photothermal material with a dark color is of considerable interest as an absorber/collector for STE applications.[369,420] B-TiO_x has attracted enormous attention in this area due to its significantly extended absorption of solar energy, ranging from UV to NIR.[125,147,150,421–426] For instance, illuminated by the simulated solar irradiation (AM 1.5 G, Xe lamp) for 60 s, the temperature of the B-TiO_x material increases from RT to 37 °C, while pure TiO_2 increases to 28 °C.[125] This has been attributed to the significant enhancement of Vis and NIR photo-absorption of B-TiO_x originated from the unique oxygen-deficient shells. To further modify B-TiO_x, a hierarchical tandem heterojunctions visible-light photocatalyst, B-TiO_x/MoS_2/Cu_2S, was designed and prepared. In this hierarchical

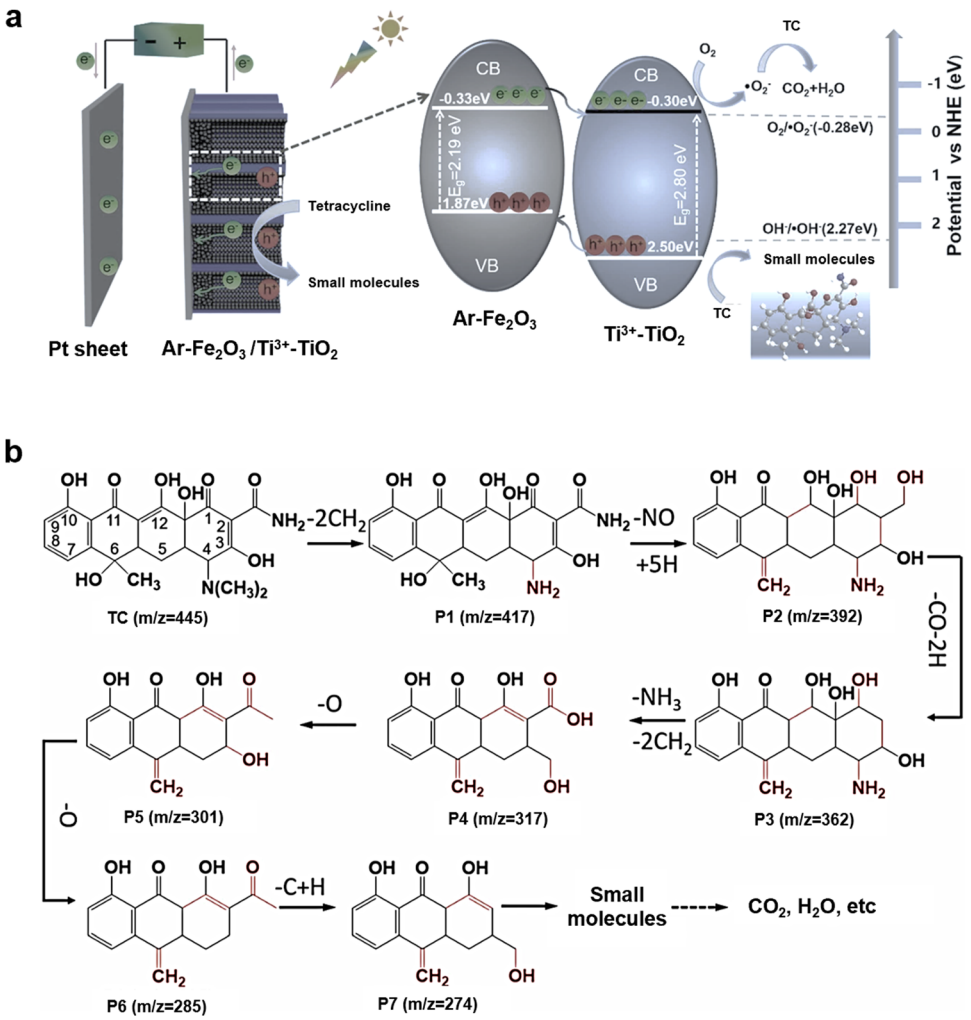

Fig. 25 (a) Proposed mechanism diagrams in Ar–Fe_2O_3/Ti^{3+}–TiO_2-NTs, and (b) Proposed TC pathway by the Ar–Fe_2O_3/Ti^{3+}–TiO_2-NTs photoelectrode. Reprinted with permission from ref. 416. © 2022 Elsevier B.V. All rights reserved.

structure, the mesoporous B-TiO_x can serve as the host to assemble MoS_2 and Cu_2S. MoS_2 acted mainly as the co-catalyst that can effectively transfer and separate photo-generated charge carriers due to suitable band alignments. The introduction of MoS_2 and Cu_2S extended the photo-response to near infrared region. In addition, both MoS_2 and Cu_2S with narrow band gap could convert solar light into heat energy. As a result, the light absorption of the B-TiO_x/MoS_2/Cu_2S in the wavelength of around 200–800 nm is stronger than both B-TiO_x and B-TiO_x/MoS_2.[225] The temperature change of the B-TiO_x, B-TiO_x/MoS_2, and B-TiO_x/MoS_2/Cu_2S was recorded with an infrared thermograph under light irradiation ($\lambda > 400$ nm). After 5 min irradiation, the temperature rose from 25 °C to 49.9 °C (B-TiO_x), 53.3 °C (B-TiO_x/MoS_2), and 58.2 °C (B-TiO_x/MoS_2/Cu_2S), respectively. Furthermore, the photothermal conversion of B-TiO_x is often assigned to the high probability of non-radiative relaxation occurring in the Ti 3d orbitals.[107] Given the low bandgap energy of B-TiO_x, the majority of photons from solar light have significantly possessed higher energy than the bandgap threshold. Consequently, above-bandgap electron–hole pairs are generated. These electron–hole pairs subsequently relax to the band edges, releasing excess of energy in form of heat, likely facilitated through an acoustic-phonon scattering mechanism.[427] This is in stark contrast to conventional wide-bandgap semiconductors, where most of absorbed light energy is typically re-emitted as photons following the recombination of electron–hole pairs near the bandgap edge.

Solar steam interfacial evaporation represents a promising strategy for seawater desalination and wastewater purification owing to its environmentally friendly characteristics.[123,332] It has been reported recently that metallic λ-Ti_3O_5 powder, also categorized as B-TiO_x, exhibits a high solar absorptivity of 96.4%, which is attributed to Ti–Ti dimer-induced flat-bands around the Fermi level.[419] This work has emphasized the critical role of tuning joint densities of states in enhancing solar absorption of photothermal materials, which has been previously overlooked in this field. Combined with the low thermal conductivity of λ-Ti_3O_5, this novel characteristic ensures efficient solar-to-heat conversion and high thermal localization. As a result, an unprecedentedly high-water

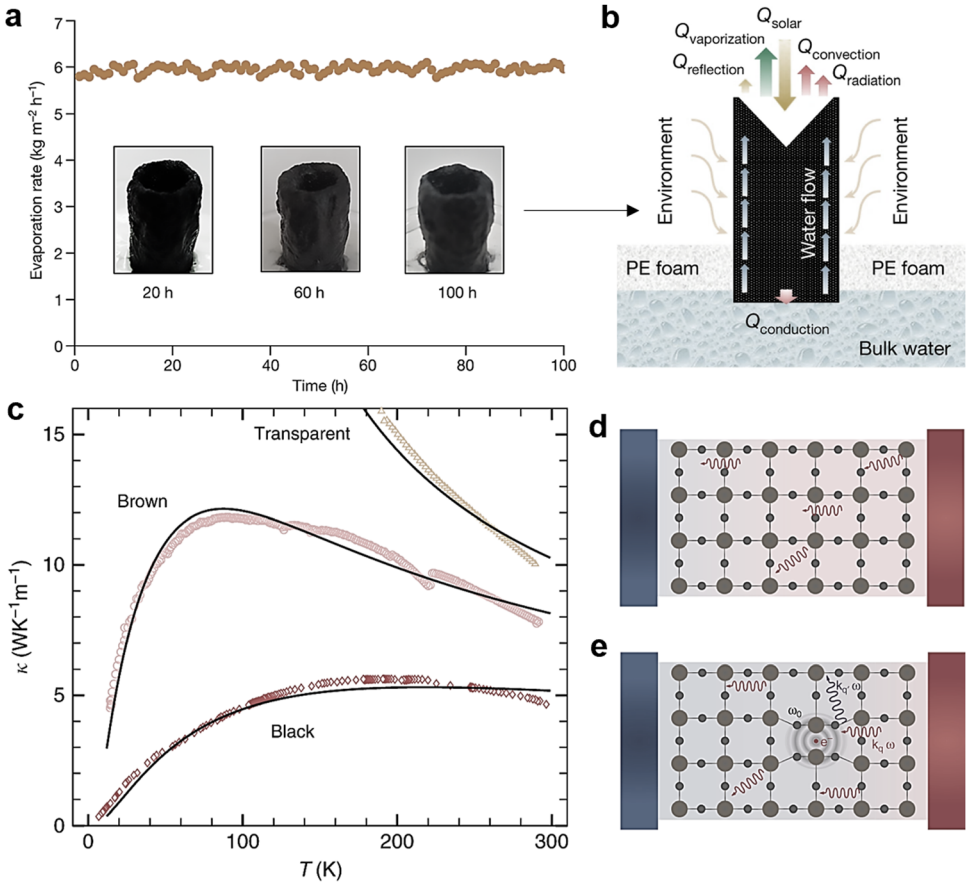

Fig. 26 (a) Evaporation rates of 3.5 wt% saline water as a function of time for the 3D-SSE containing 6 wt% λ-Ti_3O_5 powders under 1 sun of irradiation, and photographs of the 3D-SSE at 20 h, 60 h and 100 h without salt precipitation. (b) Schematic diagram of 3D-SSE system. Reprinted with permission from ref. 419. Copyright © 2023, The Author(s), under exclusive licence to Springer Nature Limited. Thermal conductivity of anatase single crystals (c) Temperature dependence of the thermal conductivity of three anatase TiO_2 single crystals, respectively, from higher to lower κ, test curves and fitted curves (solid lines). Sketches of the difference between heat propagation in (d) pristine single-crystal and in (e) crystal with oxygen vacancies. The color gradients from red to blue illustrate temperature differences across the material. Reprinted with permission from ref. 428. Copyright © 2019, The Author(s).

evaporation rate of 6.09 kg m^{-2} h^{-1} (Fig. 26a) was achieved under a 1-Sun irradiation without salt precipitation in the 3D-SSE system (Fig. 26b).[419]

To some extent, thermal conductivity is related to STE. Fig. 26(c) displays the measurement of the thermal conductivity of TiO_2 crystals in the temperature range of 0–300 K using a 4-points measurement method. It has been demonstrated that an increase in the concentration of O_v results in a dramatic decrease in thermal conductivity, leading to high thermal localization. The difference between heat propagation is proposed and sketched in both pristine single-crystal (Fig. 26d) and crystal containing O_v (Fig. 26e).[428]

6.6. Supercapacitance

Energy storage in supercapacitors is a mature technology, which has unique features in high power density, wide operating temperature range of −40 °C to 220 °C, and long cycle in millions, though further improvements in these aspects are needed.[130,286,429,430] Besides, investigations on assembling high-performance supercapacitors with low cost, high surface area, and high electrical conductivity materials have been under continuous investigation.

TiO_2 has been an obvious candidate for assembling as supercapacitors because of its low cost and chemical stability. However, it is a low electrical conductivity material that hinders its application in supercapacitor. To improve its electrical conductivity for a high-performance supercapacitor, blackening processes have been adapted to modify TiO_2.[431,432] For instance, reductive chemical of $NaBH_4$ can be used to introduce O_v to form B-TiO_x, which exhibits an improved electrical conductivity. Furthermore, B-TiO_x can be used to construct supercapacitors with high-power density, a fast charge/discharge rate, long-term life cycles, *etc.*[21,94,110,137,194,291,300,433–437] For example, the supercapacitor assembled with B-TiO_x gives a capacitance of 14.3 mF cm^{-2}, which is 14 times higher than that of the supercapacitor assembled with pristine TiO_2.[110] This low-cost material with high charge capacity value generally serve as a reference for further improvement in superconductors.

6.7. Ion battery

In addition to supercapacitors, an alternative avenue for utilizing renewable energy involves electrochemical storage of chemical energy, subsequently converting it into electrical energy through ion batteries.[130,144,264,438–440]

B-TiO_x has gained the unflagging attention from ion batteries such as sodium (Na)-ion batteries, lithium (Li)-ion batteries, magnesium (Mg)-ion batteries, *etc.* because of its low scalability of the preparation procedure, appreciable capacity, and long-term stability upon reversible operation.[130,144,283,441–448] In ion batteries, B-TiO_x has been used as both the cathode and the anode materials. Fig. 27(a) shows B-TiO_x as the cathode material in a Li–O_2 (oxygen) battery, which gives a capacity of 5761 mA h g^{-1}, higher than that of Li–O_2 batteries with other two cathodes, *i.e.*, gray TiO_2 and carbon nanotube (CNT) with 3620 and 1794 mA h g^{-1}, respectively. The good performance of the Li–O_2 battery has been assigned to the surface defects (O_v and Ti^{3+}) of B-TiO_x enabling a high electrical conductivity that further promotes the catalytic activity.[449] The charge/discharge rate capabilities of B-TiO_x assembled Li–O_2 batteries have been measured at the current densities of 100, 200, and 500 mA g^{-1} corresponding to the performances of 5761/4945, 4220/4015 and 2796/2579 mA h g^{-1}, respectively (Fig. 27(b)).[449] The long-term stability of these three Li–O_2 batteries under the same conditions are shown in Fig. 27(c): 108-cycle-stable for B-TiO_x, 40-cycle-stable for gray TiO_2, and 10-cycle-stable for CNT.[449] In the aspect of modelling, DFT simulations confirmed the function of O_v and Ti^{3+} of B-TiO_x in promoting the reversible capacity and in retaining capacity after long-term cycles of Mg-ion batteries.[447] Other important features such as operation at a low temperature of −20 °C has been particularly reported, where the B-TiO_x-ion battery retained 84% capacity after 100-cycle charge–discharge tests.[450]

6.8. Fuel cell

Fuel cells operate akin to batteries, where the production of electricity is continuously sustained by chemical consumption. In the case of low-carbon chemicals, such as green H_2 and NH_3, their utilization in fuel cells further contributes to the advancement of a sustainable society. For example, hydrogen fuel cells use H_2 to produce electricity for cars without CO_2 emissions.

B-TiO_x has the major advantages of reasonable electrical conductivity, decreased mass transfer barrier, and large amounts of anchoring sites provided by O_v and –OH groups that arose interests to both the cathode and the anode materials for fuel cells.[451–453] For example, a proton exchange membrane (PEM) fuel cell used B-TiO_x as both anode (B-TiO_x-Anode) and cathode electrode for H_2–O_2 reaction, which gives a maximum power density of 403 and 52 mW cm^{-2}, respectively.[452] For the B-TiO_x-Anode, after a 100-h stability test at the constant voltage of 0.45 V, the corresponding current density is still stable at

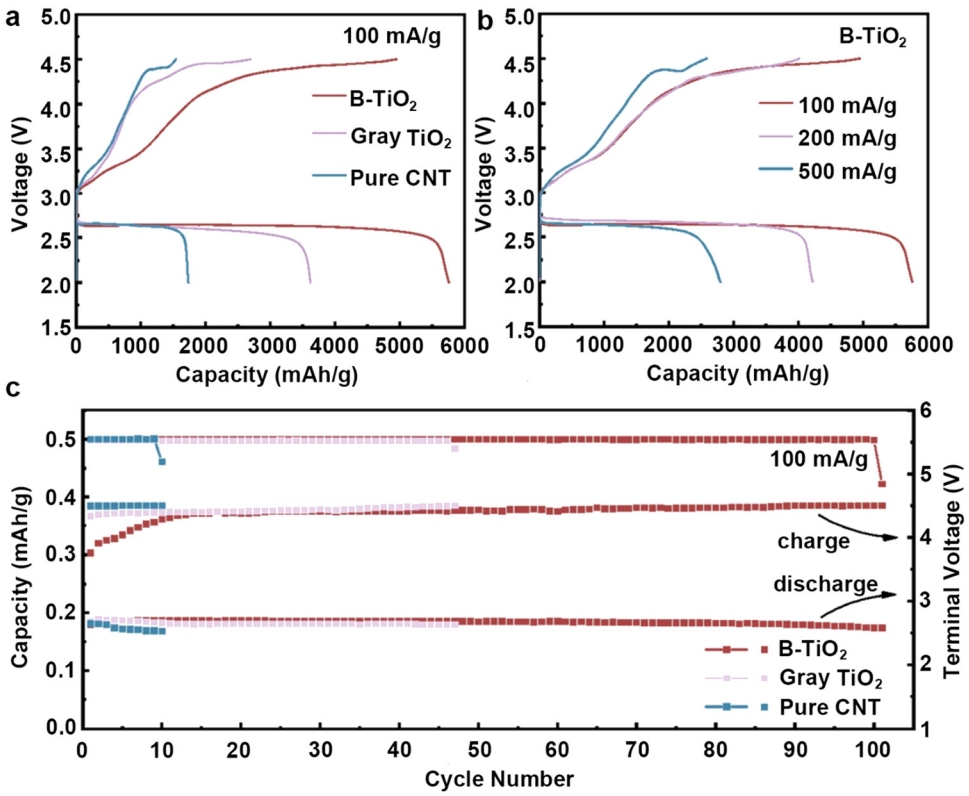

Fig. 27 (a) The initial discharge/charge profiles of B-TiO_x, gray TiO_2, and pure CNT cathodes at a current density of 100 mA g^{-1}, (b) the initial discharge/charge profiles of the B-TiO_x cathode at different current densities, and (c) cyclability and the terminal voltage of the B-TiO_x, gray TiO_2, and pure CNT cathodes. Reprinted with permission from ref. 449. Copyright © 2020, Elsevier Ltd and Techna Group S.r.l.

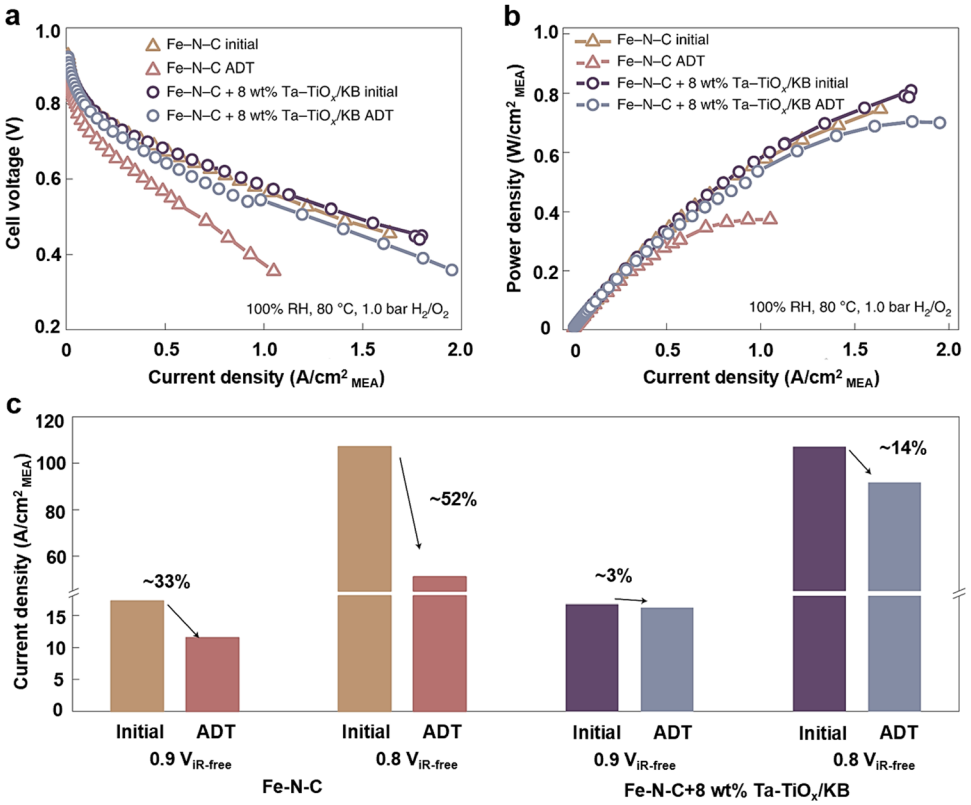

Fig. 28 (a) Polarization–discharge voltage curves as a function of current density plots, (b) polarization–discharge power density curves as a function of current density plots for cells before and after the accelerated durability test (ADT). (c) Current density decay comparison for cells with and without Ta–TiO_x/KB after the ADT. The *y*-axis break is used to enhance readability for small current density values. Reprinted with permission from ref. 455. Copyright © 2022, The Author(s), under exclusive license to Springer Nature Limited.

1500 mA cm^{-2} without obvious decay, and the polarization curves (before and after 100-h running) are measured to demonstrate their stability results.[454] Highly active and durable catalysts for the oxygen reduction reaction (ORR) are important to PEM fuel cells. In 2022, an active protective strategy, using Ta–TiO_x nanoparticles as radical scavengers for radicals and H_2O_2, was demonstrated to protect Fe–N–C catalysts from degradation.[455] The cell voltage (Fig. 28a) and power density (Fig. 28b) polarization plots as a function of different current density were shown with (Fe–N–C + 8% Ta–TiO_x/KB) and without scavenger (Fe–N–C) under an accelerated durability test (ADT) to confirm the reliability of Ta–TiO_x.[455] After the ADT, the PEM fuel cell with the Ta–TiO_x/KB scavengers showed a current density of 0.63 A cm^{-2} at 0.6 V and gave a highest power density of 700 mW cm^{-2}, while these of catalyst without scavengers gave 0.39 A cm^{-2} at 0.6 V, and 370 mW cm^{-2}. Fig. 28(c) compares the current density of the cells with and without the Ta–TiO_x/KB scavengers at internal resistance-compensated voltages ($V_{iR\text{-}free}$) of 0.8 $V_{iR\text{-}free}$ and 0.9 $V_{iR\text{-}free}$. The cell with Ta–TiO_x scavengers at 0.8 $V_{iR\text{-}free}$ decreases the decay from 33% to 3%, and at 0.9 $V_{iR\text{-}free}$ shows a decrease of decay from 52% to 14%. These findings showed that the Ta–TiO_x scavengers play a prominent role in the improvement of the PGM-free cathode durability and demonstrated a new function of B-TiO_x to stabilize catalysts. However, at present, the investigations of B-TiO_x-based materials in fuel cells are still in infancy stage and further knowledge is being actively pursued.

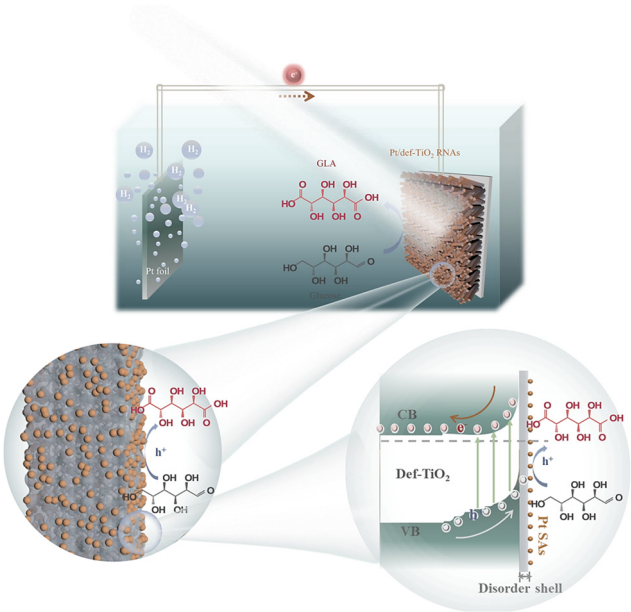

Fig. 29 B-TiO_x is used for PEC oxidation of glucose to glucaric acid (GLA). Reprinted with permission from ref. 213. Copyright © 2023, The Author(s).

6.9. Other applications

In addition to the aforementioned applications of B-TiO_x in energy conversion and storage systems, and waste treatments, other applications such as PEC biomass conversion (Fig. 29),[213] solar cells,[100,456,457] sensors,[458–461] stem cell capture,[71] betavoltaics,[37,105] smart windows,[462] self-cleaning face masks,[463,464] and others[465,466] have also been investigated. Although these cases are limited in number, their contributions enrich applied fields and research databases, providing valuable insights into the understanding of B-TiO_x from diverse perspectives. For instance, dye-719 sensitized solar cells are fabricated with pristine TiO_2 and B-TiO_x, separately, yielding performances of 2.26% (pristine) and 1.25% (black), which is due to the downshift of the conduction band of B-TiO_x during the blackening process.[100]

7. Conclusions and perspectives

Over the past decade, significant strides have been made in the research of black titanium oxide (B-TiO_x), encompassing its synthesis, modification, characterization, and application. Notable achievements include the development of energy and time-efficient synthesis methods for B-TiO_x. The focus now shifts towards reducing costs, scaling up production, and refining the controllability of the reduction process. Additionally, addressing the fundamental challenges in understanding the mechanisms by which B-TiO_x enhances performance, through *in situ* or operando characterizations, is an ongoing effort. As highlighted in this review, B-TiO_x has demonstrated considerable promise in solar energy utilization, particularly in applications such as green hydrogen production, CO_2 reduction, and ammonia synthesis. Despite its potential, B-TiO_x remains underexploited in electrochemical cells, where its high charge carrier density, rapid electron transport, and affordability could offer significant advantages. The continued exploration of B-TiO_x's applications is expected to play a pivotal role in the development of sustainable energy solutions and environmental remediation. Looking ahead, there is a clear need for *in situ* techniques that operate across multiple scales to uncover the local structural nuances of B-TiO_x during its synthesis, modification, characterization, and application. Advanced diagnostic methods, including cutting-edge synchrotron and high-intensity light sources with superior spatial and temporal resolution, are essential for detailed manipulation of the material's blackness, including the degree and depth, as well as local order–disorder and strain–stress features. These insights are crucial for establishing correlations with catalytic activity, selectivity, and device performance. Furthermore, large-scale demonstrations, supported by predictive models and long-term stability assessments, are vital for transitioning B-TiO_x from the laboratory to real-world applications. The successful commercialization of B-TiO_x will hinge on these comprehensive evaluations, ensuring that this promising material class can meet the demands of a sustainable future.

The remarkable physicochemical attributes of B-TiO_x have spurred the advancement of blackening methods, concurrently catalyzing its deployment in renewable energy harnessing, conversion, and both direct and indirect storage into chemical forms or electricity. As laboratory-scale synthesis, modification, and application techniques evolve, the imperative now shifts to scaling up these processes. This escalation is critical to ensure a seamless transition from lab to market, meeting the commercial demand and facilitating widespread adoption.[190,467,468] Besides, safety issue, long-term stability, scale-up effect, material cost, and time-cost are needed to be considered and evaluated based on both experiments, theoretical calculations, and models.[469] For example, if considering the future industrial issues such as the waste reprocessing costs, manufacturing costs, and the installation, the metal substrates such as titanium metal is highly competitive with the conventional transparent conductive glasses.[157,470,471]

The blackening of titanium dioxide has gained widespread acceptance for its utility, yet a deeper understanding of B-TiO_x remains a necessity. Employing *in situ* techniques across multiple scales is invaluable for observing, recording, and comprehending the material's formation, modification, and application processes. These techniques are instrumental in elucidating the material's properties, thereby enabling the manipulation of physicochemical characteristics, such as bandgaps, through precise control of the blackening process. Such insights facilitate a balance between cost-efficiency and performance from a commercial standpoint. Additionally, the significance of the reduced metal oxide layers, TiO_x, is recognized for their association with highly active catalytic reactions.[83] To investigate the formation and influence of thin reducible metal oxide layers on catalytic activity, a combination of *in situ* and ex-situ analytical tools should be utilized. *In situ* techniques, including transmission electron microscopy (TEM), X-ray absorption spectroscopy (XAS), and near ambient pressure X-ray photoelectron spectroscopy (NAP-XPS), are essential for real-time observation of the material under reaction conditions. *Ex situ* methods, such as electron energy loss spectroscopy (EELS) and pair distribution function (PDF) analysis, provide detailed post-reaction insights into the material's structure and electronic properties. Complementing these experimental approaches with density functional theory (DFT) calculations allows for a comprehensive understanding of the material at the atomic level, enabling the correlation of structural features with catalytic performance.[472] Thus, further *in situ* investigations are constantly on call for providing further details in deepening the understanding of B-TiO_x. The formation, and the thickness of reducible metal oxide TiO_2, *viz*, B-TiO_x, in different reaction conditions is in correlation with the description of B° that can use *in situ* STEM combined with *in situ* EELS. Different blackening methods lead to different B° of B-TiO_x nanotube/sphere/discs/layers, such as disorder structures and geometric and strain–stress effects, where PDF may be invoked to reveal.

Very recently, Li *et al.* have pioneered the development of a NAP-XPS technique using trimethylphosphine (TMP) as a surface probe.[297] This approach has been employed to

demonstrate facet-dependent charge accumulation in a N-doped TiO_2 photocatalyst under photoexcitation. The rationale behind this lies in the ability of the nucleophilic TMP molecule to form stable adducts with exposed Lewis acid (LA) sites on the surface, such as the five-coordinated Ti^{4+}. The interaction between TMP and the surface LA sites is very sensitive to the changes in the surface chemical micro-environment and local electron density, resulting in shifts in binding energy on P 2p XPS spectra. It should be emphasized that this technique offers truly surface sensitivity, as TMP molecules can only adsorb on the topmost surface. This contrasts with conventional laboratory based XPS, which provides information on both the surface and subsurface regions. Likewise, it has been demonstrated that the surface features of modified TiO_2 materials can also be investigated by the probe-assisted solid state nuclear magnetic resonance technique.[473] Foo *et al.* has recently reported a comprehensive structural study of N-doped TiO_2 using variable-temperature synchrotron X-ray powder diffraction.[246] Their findings revealed an unusual anisotropic thermal expansion, shedding light on the intricate relationship between subsurface oxygen vacancies, nitrogen doping levels, and photocatalytic activity.

Moreover, the extent of reductive conditions, such as the duration of blackening treatment, can be fine-tuned to regulate the thickness or depth of the blackened layers, thereby affecting their physicochemical properties. To maintain coherence with these alterations, *in situ* preparation and modification techniques should evolve in tandem with *in situ* characterization methods. A mechanistic analysis that integrates DFT, molecular dynamics, and machine learning can provide a comprehensive framework from simulation to the calculated preparation and application of materials. This approach not only enhances our understanding of the materials but also accelerates the development process, reducing the time required to transition from laboratory research to market-ready technologies.

Author contributions

Hou X. L.: conceiving the topic, literature search, data collection and analysis, writing – original draft and writing – review & editing. Li Y. Y.: discussion and writing – review & editing. Zhang H.: discussion and writing – review & editing. Lund P. D.: writing – review & editing. Kwan J.: writing – review & editing and supervision. Tsang S. C. E.: conceiving the topic, discussion, writing – review & editing and overall supervision.

Data availability

No primary research results, software or code have been included and no new data were generated or analysed as part of this review.

Conflicts of interest

None of the authors has any competing financial or other conflict of interest.

Acknowledgements

Financial support by Engineering and Physical Science Research Council (EPSRC), UK (EP/W012316/1) and (EP/X525777/1) is kindly acknowledged. The authors also thank to Miss Qin Yi in providing the image for the TOC.

References

1 C. Zhang, Y. Xie, H. Zhang, Y. Gu and X. Zhang, *Energy*, 2023, **262**, 125453.
2 BP's Statistical Review of World Energy, 2022.
3 X. Chen, L. Liu, P. Yu and S. Mao, *Science*, 2011, **331**, 746–750.
4 T. Rajaraman, S. Parikh and V. Gandhi, *Chem. Eng. J.*, 2020, **389**, 123918.
5 S. Ullattil, S. Narendranath, S. Pillai and P. Periyat, *Chem. Eng. J.*, 2018, **343**, 708–736.
6 X. Chen, L. Liu and F. Huang, *Chem. Soc. Rev.*, 2015, **44**, 1861–1885.
7 E. Ivanova, J. Hasan, H. Webb, G. Gervinskas, S. Juodkazis, V. Truong, A. Wu, R. Lamb, V. Baulin, G. Watson, J. Watson, D. Mainwaring and R. Crawford, *Nat. Commun.*, 2013, **4**, 2838.
8 Y. Yu, Z. Zhang, X. Yin, A. Kvit, Q. Liao, Z. Kang, X. Yan, Y. Zhang and X. Wang, *Nat. Energy*, 2017, **2**, 1–7.
9 J. Lv, T. Zhang, P. Zhang, Y. Zhao and S. Li, *Nanoscale Res. Lett.*, 2018, **13**, 1–10.
10 H. Kim, S. Uddin, D.-H. Lien, M. Yeh, N. Azar, S. Balendhran, T. Kim, N. Gupta, Y. Rho, C. Grigoropoulos, K. Crozier and A. Javey, *Nature*, 2021, **596**, 232–237.
11 X. Wang, R. Raghupathy, C. Querebillo, Z. Liao, D. Li, K. Lin, M. Hantusch, Z. Sofer, B. Li, E. Zschech, I. Weidinger, T. Kuhne, H. Mirhosseini, M. Yu and X. Feng, *Adv. Mater.*, 2021, **33**, e2008752.
12 H. Shi, S. Fu, Y. Liu, C. Neumann, M. Wang, H. Dong, P. Kot, M. Bonn, H. Wang, A. Turchanin, O. Schmidt, A. Shaygan Nia, S. Yang and X. Feng, *Adv. Mater.*, 2021, **33**, e2105694.
13 Z. Tian, P. Zhang, P. Qin, D. Sun, S. Zhang, X. Guo, W. Zhao, D. Zhao and F. Huang, *Adv. Energy Mater.*, 2019, **9**, 1901287.
14 X. Xu, Y. Xu, F. Xu, G. Jiang, J. Jian, H. Yu, E. Zhang, D. Shchukin, S. Kaskel and H. Wang, *J. Mater. Chem. A*, 2020, **8**, 1636–1645.
15 R. Fernández-Climent, S. Giménez and M. García-Tecedor, *Sustainable Energy Fuels*, 2020, **4**, 5916–5926.
16 G. Wang, Y. Ling, H. Wang, X. Yang, C. Wang, J. Zhang and Y. Li, *Energy Environ. Sci.*, 2012, **5**, 6180–6187.
17 Y. Zhang, J. Tang, G. Wang, M. Zhang and X. Hu, *J. Cryst. Growth*, 2006, **294**, 278–282.
18 X. Chen and S. Mao, *Chem. Rev.*, 2007, **107**, 2891–2959.
19 Y. Ma, X. Wang, Y. Jia, X. Chen, H. Han and C. Li, *Chem. Rev.*, 2014, **114**, 9987–10043.
20 X. Chen and A. Selloni, *Chem. Rev.*, 2014, **114**, 9281–9282.

21 J. Chen, Z. Xia, H. Li, Q. Li and Y. Zhang, *Electrochim. Acta*, 2015, **166**, 174–182.
22 X. Hou, Y. Zhao and Y. Li, *Int. J. Hydrogen Energy*, 2023, **48**, 14279–14286.
23 H. Brahmi, R. Neupane, L. Xie, S. Singh, M. Yarali, G. Katwal, S. Chen, M. Paulose, O. Varghese and A. Mavrokefalos, *Nanoscale*, 2018, **10**, 3863–3870.
24 V. Zuñiga-Ibarra, S. Shaji, B. Krishnan, J. Johny, S. Sharma Kanakkillam, D. Avellaneda, J. Martinez, T. Roy and N. Ramos-Delgado, *Appl. Surf. Sci.*, 2019, **483**, 156–164.
25 N. Rahimi, R. Pax and E. Gray, *Prog. Solid State Chem.*, 2019, **55**, 1–19.
26 J. Zheng, S. Bao, X. Zhang, H. Wu, R. Chen and P. Jin, *Appl. Catal., B*, 2016, **183**, 69–74.
27 W. Fang, M. Xing and J. Zhang, *J. Photochem. Photobiol., C*, 2017, **32**, 21–39.
28 H. Hu, Y. Lin and Y. Hu, *Chem. Eng. J.*, 2019, **375**, 122029.
29 Z. Li, J. Dong, Y. Zhang, T. Zhuang, H. Wang, X. Du, X. Cui and Z. Wang, *Compos. Sci. Technol.*, 2022, **218**, 109198.
30 A. Naldoni, M. Altomare, G. Zoppellaro, N. Liu, S. Kment, R. Zboril and P. Schmuki, *ACS Catal.*, 2019, **9**, 345–364.
31 S. Kim, Y. Cho, R. Rhee and J. Park, *Carbon Energy*, 2020, **2**, 44–53.
32 A. Chatzitakis and S. Sartori, *Chem. Phys. Chem.*, 2019, **20**, 1272–1281.
33 Z. Li, S. Wang, J. Wu and W. Zhou, *Renewable Sustainable Energy Rev.*, 2022, **156**, 111980.
34 J. Wang, R. Guo, Z. Bi, X. Chen, X. Hu and W. Pan, *Nanoscale*, 2022, **14**, 11512–11528.
35 Z. Xiu, M. Guo, T. Zhao, K. Pan, Z. Xing, Z. Li and W. Zhou, *Chem. Eng. J.*, 2020, **382**, 123011.
36 P. Sun, Z. Cao, Y. Zeng, W. Xie, N. Li, D. Luan, S. Yang, L. Yu and D. Lou, *Angew. Chem., Int. Ed.*, 2022, **61**, e202115649.
37 L. Placa, P. Vital, L. Gomes, A. Roveda, Jr., D. R. Cardoso, C. Martins and H. Wender, *ACS Appl. Mater. Interfaces*, 2022, **61**, 43259–43271.
38 R. Katal, S. Masudy-Panah, M. Tanhaei, M. Farahani and H. Jiangyong, *Chem. Eng. J.*, 2020, **384**, 123384.
39 Y. Liu, L. Tian, X. Tan, X. Li and X. Chen, *Sci. Bull.*, 2017, **62**, 431–441.
40 Y. Li and E. Tsang, *Mater. Today Sustainability*, 2020, **9**, 100032.
41 X. Hou, H. Zhang, R. Raju, Y. Li and P. Lund, *J. Power Sources*, 2023, **580**, 233281.
42 R. Vadakkekara and S. Jadkar, *ACS Appl. Energy Mater.*, 2021, **5**, 674–684.
43 L. Yang, Y. Peng, Y. Yang, J. Liu, Z. Li, Y. Ma, Z. Zhang, Y. Wei, S. Li, Z. Huang and N. Long, *ACS Appl. Nano Mater.*, 2018, **1**, 4516–4527.
44 A. Ziarati, A. Badiei and R. Luque, *Appl. Catal., B*, 2018, **238**, 177–183.
45 O. Secundino-Sánchez, J. Díaz-Reyes, J. Sánchez-Ramírez, J. Arias-Cerón, M. Galván-Arellano and O. Vázquez-Cuchillo, *Catal. Today*, 2022, **392–393**, 13–22.
46 K. Lan, Y. Liu, W. Zhang, Y. Liu, A. Elzatahry, R. Wang, Y. Xia, D. Al-Dhayan, N. Zheng and D. Zhao, *J. Am. Chem. Soc.*, 2018, **140**, 4135–4143.
47 L. Sheng, T. Liao, L. Kou and Z. Sun, *Mater. Today Energy*, 2017, **3**, 32–39.
48 J. Lin, Y. U. Heo, A. Nattestad, Z. Sun, L. Wang, J. Kim and S. Dou, *Sci. Rep.*, 2014, **4**, 5769.
49 N.-W. Lee, J.-W. Jung, J.-S. Lee, H.-Y. Jang, I.-D. Kim and W.-H. Ryu, *Electrochim. Acta*, 2018, **263**, 417–425.
50 S. Rej, S. Hejazi, Z. Badura, G. Zoppellaro, S. Kalytchuk, Š. Kment, P. Fornasiero and A. Naldoni, *ACS Sustainable Chem. Eng.*, 2022, **10**, 17286–17296.
51 H. Shi, X. Wang, M. Zheng, X. Wu, Y. Chen, Z. Yang, G. Zhang and H. Duan, *Adv. Mater. Interfaces*, 2016, **3**, 1600588.
52 K. Lan, Q. Wei and D. Zhao, *Angew. Chem., Int. Ed.*, 2022, **61**, e202200777.
53 Y. Zeng, Y. Wang, S. Zhang and Q. Zhong, *Phys. Chem. Chem. Phys.*, 2018, **20**, 22744–22752.
54 C. Xu, T. Liu, W. Guo, Y. Sun, C. Liang, K. Cao, T. Guan, Z. Liang and L. Jiang, *Adv. Eng. Mater.*, 2020, **22**, 1901088.
55 J. Macak, H. Tsuchiya, A. Ghicov, K. Yasuda, R. Hahn, S. Bauer and P. Schmuki, *Curr. Opin. Solid State Mater. Sci.*, 2007, **11**, 3–18.
56 J. Macak, H. Tsuchiya and P. Schmuki, *Angew. Chem., Int. Ed.*, 2005, **44**, 2100–2102.
57 B. Yin, Q. Qian, Z. Xiong, H. Jiang, Y. Lin and D. Feng, *Nanotechnology*, 2019, **30**, 155702.
58 N. Liu, X. Chen, J. Zhang and J. Schwank, *Catal. Today*, 2014, **225**, 34–51.
59 S. Perera, R. Mariano, K. Vu, N. Nour, O. Seitz, Y. Chabal and K. Balkus, *ACS Catal.*, 2012, **2**, 949–956.
60 G. Yang, B. Yang, T. Xiao and Z. Yan, *Appl. Surf. Sci.*, 2013, **283**, 402–410.
61 L. Yuan, S. Meng, Y. Zhou and Z. Yue, *J. Mater. Chem. A*, 2013, **1**, 2552–2557.
62 F. Zhuge, J. Qiu, X. Li, X. Gao, X. Gan and W. Yu, *Adv. Mater.*, 2011, **23**, 1330–1334.
63 J. Zhang, Y. Kusumawati and T. Pauporté, *Electrochim. Acta*, 2016, **201**, 125–133.
64 H. Ali-Loytty, M. Hannula, J. Saari, L. Palmolahti, B. Bhuskute, R. Ulkuniemi, T. Nyyssonen, K. Lahtonen and M. Valden, *ACS Appl. Mater. Interfaces*, 2019, **11**, 2758–2762.
65 M. Liu, L. Zheng, X. Bao, Z. Wang, P. Wang, Y. Liu, H. Cheng, Y. Dai, B. Huang and Z. Zheng, *Chem. Eng. J.*, 2021, **405**, 126654.
66 A. Yakovlev, V. Milichko, E. Pidko, V. Vinogradov and A. Vinogradov, *Sci. Rep.*, 2016, **6**, 37090.
67 M. Paik, Y. Lee, H. Yun, S. Lee, S. Hong and S. Seok, *Adv. Energy Mater.*, 2020, **10**, 2001799.
68 C. Wang, X. Kang, J. Liu, D. Wang, N. Wang, J. Chen, J. Wang, C. Tian and H. Fu, *Inorg. Chem. Front.*, 2023, **10**, 1153–1163.
69 J. Kim, D. Suh, C. Kim, Y. Baek, B. Lee, H. Kim, J.-C. Lee and J. Yoon, *Desalination*, 2016, **397**, 157–164.
70 C.-Y. Lee, A. Taylor, S. Beirne and G. Wallace, *Adv. Energy Mater.*, 2017, **7**, 1701060.
71 A. Mazare, J. Park, S. Simons, S. Mohajernia, I. Hwang, J. E. Yoo, H. Schneider, M. Fischer and P. Schmuki, *Acta Biomater.*, 2019, **97**, 681–688.

72 H. Pan, M. Sun, X. Wang, M. Zhang, M. Muruganantan and Y. Zhang, *Appl. Catal., B*, 2022, **307**, 121174.
73 W. Li, A. Elzatahry, D. Aldhayan and D. Zhao, *Chem. Soc. Rev.*, 2018, **47**, 8203–8237.
74 A. Gromov, N. Kouznetsova, S. Yudina and V. Lunin, *J. Alloys Compd.*, 1997, **261**, 269–272.
75 R. David, Y. Finkelstein, E. Grinberg, S. Samuha, E. Rabkin and D. Cohen, *Int. J. Hydrogen Energy*, 2020, **45**, 25043–25053.
76 K. Kato, Y. Xin, J. Hong, K. Katsumata and T. Shirai, *Adv. Powder Technol.*, 2020, **31**, 1777–1783.
77 J. Gu, J. Aguiar, S. Ferrere, K. Steirer, Y. Yan, C. Xiao, J. Young, M. Al-Jassim, N. Neale and J. Turner, *Nat. Energy*, 2017, **2**(2), 1–8.
78 J. Seo, S. Jeon, S. Lee, D. Lim, J. Kim, J. Kim, S. Ahn and W. Jung, *ACS Catal.*, 2022, **12**, 8593–8600.
79 J. Huang, S. Yang, X. Tang, L. Yang, W. Chen, Z. Chen, X. Li, Z. Zeng, Z. Tang and X. Gui, *Adv. Mater.*, 2023, e2303737.
80 Y. Xu, S. Chen, X. Chang, X. Wang, G. Sun, Z. Lu, Z. Zhao, C. Pei and J. Gong, *ACS Catal.*, 2023, **13**, 6104–6113.
81 J. Zhou, G. Li, H. Li, Z. Ma, S. Liu and X. Tang, *Fuel*, 2023, **343**, 128014.
82 S. Chen, Y. Xu, X. Chang, Y. Pan, G. Sun, X. Wang, D. Fu, C. Pei, Z. Zhao, D. Su and J. Gong, *Science*, 2024, **385**, 295–300.
83 M. Monai, K. Jenkinson, A. Melcherts, J. Louwen, E. Irmak, S. Van Aert, T. Altantzis, C. Vogt, W. Van der Stam, T. Duchoň, B. Šmíd, E. Groeneveld, P. Berben, S. Bals and B. Weckhuysen, *Science*, 2023, **380**, 644–651.
84 J. Li, E.-H. Wu, J. Hou, P. Huang, Z. Xu, Y. Jiang, Q.-S. Liu and Y.-Q. Zhong, *RSC Adv.*, 2020, **10**, 34775–34780.
85 N. Denisov, S. Qin, G. Cha, J. Yoo and P. Schmuki, *J. Electroanal. Chem.*, 2020, **872**, 114098.
86 Y. Tong, S. Fang, C. Wang and Y. Hu, *J. Phys. Chem. Solids*, 2021, **154**, 110053.
87 J. Li, C.-H. Liu, X. Li, Z.-Q. Wang, Y.-C. Shao, S.-D. Wang, X.-L. Sun, W.-F. Pong, J.-H. Guo and T.-K. Sham, *Chem. Mater.*, 2016, **28**, 4467–4475.
88 Y. Li, Z. Wang, Y. Wang, A. Kovács, C. Foo, R. Dunin-Borkowski, Y. Lu, R. Taylor, C. Wu and E. Tsang, *Energy Environ. Sci.*, 2022, **15**, 265–277.
89 J. Lim, Y. Yang and M. Hoffmann, *Environ. Sci. Technol.*, 2019, **53**, 6972–6980.
90 E. Khorashadizade, S. Mohajernia, S. Hejazi, H. Mehdipour, N. Naseri, O. Moradlou, A. Moshfegh and P. Schmuki, *J. Phys. Chem. C*, 2021, **125**, 6116–6127.
91 N. Liu, C. Schneider, D. Freitag, M. Hartmann, U. Venkatesan, J. Muller, E. Spiecker and P. Schmuki, *Nano Lett.*, 2014, **14**, 3309–3313.
92 M. Plodinec, I. Grčić, M. Willinger, A. Hammud, X. Huang, I. Panžić and A. Gajović, *J. Alloys Compd.*, 2019, **776**, 883–896.
93 Y. Yang, L. Kao, Y. Liu, K. Sun, H. Yu, J. Guo, S. Liou and M. Hoffmann, *ACS Catal.*, 2018, **8**, 4278–4287.
94 S. Mohajernia, S. Hejazi, A. Mazare, N. Nguyen, I. Hwang, S. Kment, G. Zoppellaro, O. Tomanec, R. Zboril and P. Schmuki, *Mater. Today Energy*, 2017, **6**, 46–52.
95 M. Motola, M. Čaplovičová, M. Krbal, H. Sopha, G. Thirunavukkarasu, M. Gregor, G. Plesch and J. Macak, *Electrochim. Acta*, 2020, **331**, 135374.
96 H. Brahmi, R. Neupane, L. Xie, S. Singh, M. Yarali, G. Katwal, S. Chen, M. Paulose and A. Mavrokefalos, *Nanoscale*, 2018, **10**, 3863–3870.
97 S. Wang, Z. Zhang, W. Huo, X. Zhang, F. Fang, Z. Xie and J. Jiang, *Chem. Eng. J.*, 2021, **403**, 126331.
98 E. Lee, C. Park, D. W. Lee, G. Lee, H.-Y. Park, J. Jang, H.-J. Kim, Y.-E. Sung, Y. Tak and S. J. Yoo, *ACS Catal.*, 2020, **10**, 12080–12090.
99 Y. Xu, M. Melia, L.-K. Tsui, J. Fitz-Gerald and G. Zangari, *J. Phys. Chem. C*, 2017, **121**, 17121–17128.
100 H. Li, Z. Chen, C. Tsang, Z. Li, X. Ran, C. Lee, B. Nie, L. Zheng, T. Hung, J. Lu, B. Pan and Y. Li, *J. Mater. Chem. A*, 2014, **2**, 229–236.
101 X. Hou, S. Jiang and Y. Li, *Appl. Catal., B*, 2019, **258**, 117949.
102 H. Zhu, M. Zhao, J. Zhou, W. Li, H. Wang, Z. Xu, L. Lu, L. Pei, Z. Shi, S. Yan, Z. Li and Z. Zou, *Appl. Catal., B*, 2018, **234**, 100–108.
103 Z. Li, Y. Ding, W. Kang, C. Li, D. Lin, X. Wang, Z. Chen, M. Wu and D. Pan, *Electrochim. Acta*, 2015, **161**, 40–47.
104 N. Peighambardoust, S. Khameneh Asl, R. Mohammadpour and S. Asl, *Electrochim. Acta*, 2018, **270**, 245–255.
105 Y. Ma, N. Wang, J. Chen, C. Chen, H. San, J. Chen and Z. Cheng, *ACS Appl. Mater. Interfaces*, 2018, **10**, 22174–22181.
106 C. Xu, Y. Song, L. Lu, C. Cheng, D. Liu, X. Fang, X. Chen, X. Zhu and D. Li, *Nanoscale Res. Lett.*, 2013, **8**, 1–7.
107 Y. Zhang, X. Chen, S. Zhang, L. Yin and Y. Yang, *Chem. Eng. J.*, 2020, **401**, 126033.
108 Y. Cheng, J. Gao, Q. Shi, Z. Li and W. Huang, *J. Alloys Compd.*, 2022, **901**, 163562.
109 Z. Zhang, M. Hedhili, H. Zhu and P. Wang, *Phys. Chem. Chem. Phys.*, 2013, **15**, 15637.
110 K. Du, G. Liu, M. Li, C. Wu, X. Chen and K. Wang, *Electrochim. Acta*, 2016, **210**, 367–374.
111 K. Du, G. Liu, X. Chen and K. Wang, *Electrochim. Acta*, 2018, **277**, 244–254.
112 Y. Yang, J. Liao, Y. Li, X. Cao, N. Li, C. Wang and S. Lin, *RSC Adv.*, 2016, **6**, 46871–46878.
113 Y. Yang and M. Hoffmann, *Environ. Sci. Technol.*, 2016, **50**, 11888–11894.
114 C. Kim, S. Kim, S. Hong, J. Lee and J. Yoon, *Phys. Chem. Chem. Phys.*, 2016, **18**, 14370–14375.
115 P. Li, Z. Jin, Z. Fang and G. Yu, *Angew. Chem., Int. Ed.*, 2020, **59**, 22610–22616.
116 D. Yu, Y. Zhang, F. Wang and J. Dai, *RSC Adv.*, 2021, **11**, 2307–2314.
117 L. Zhu, H. Ma, H. Han, Y. Fu, C. Ma, Z. Yu and X. Dong, *RSC Adv.*, 2018, **8**, 18992–19000.
118 X. Hou, L. Fan, Y. Zhao, P. Lund and Y. Li, *J. Power Sources*, 2022, **524**, 231095.
119 M. Shang, H. Hu, G. Lu and Y. Bi, *J. Mater. Chem. A*, 2016, **4**, 5849–5853.

120 H. Cui, W. Zhao, C. Yang, H. Yin, T. Lin, Y. Shan, Y. Xie, H. Gu and F. Huang, *J. Mater. Chem. A*, 2014, **2**, 8612–8616.
121 A. Sinhamahapatra, J.-P. Jeon and J.-S. Yu, *Energy Environ. Sci.*, 2015, **8**, 3539–3544.
122 L. Hu, Y. Li, W. Zheng, Y.-K. Peng, E. Tsang, L. Lee and K.-Y. Wong, *J. Mater. Chem. A*, 2020, **8**, 22828–22839.
123 M. Ye, J. Jia, Z. Wu, C. Qian, R. Chen, P. O'Brien, W. Sun, Y. Dong and G. Ozin, *Adv. Energy Mater.*, 2017, **7**, 1601811.
124 C. Yang, Z. Wang, T. Lin, H. Yin, X. Lu, D. Wan, T. Xu, C. Zheng, J. Lin, F. Huang, X. Xie and M. Jiang, *J. Am. Chem. Soc.*, 2013, **135**, 17831–17838.
125 Z. Wang, C. Yang, T. Lin, H. Yin, P. Chen, D. Wan, F. Xu, F. Huang, J. Lin, X. Xie and M. Jiang, *Energy Environ. Sci.*, 2013, **6**, 3007.
126 J. Gao, Q. Shen, R. Guan, J. Xue, X. Liu, H. Jia, Q. Li and Y. Wu, *J. CO2 Util.*, 2020, **35**, 205–215.
127 W. Ou, J. Pan, Y. Liu, S. Li, H. Li, W. Zhao, J. Wang, C. Song, Y. Zheng and C. Li, *J. Energy Chem.*, 2020, **43**, 188–194.
128 Y. Cao, Z. Xing, Z. Li, X. Wu, M. Hu, X. Yan, Q. Zhu, S. Yang and W. Zhou, *J. Hazard. Mater.*, 2018, **343**, 181–190.
129 J. Cai, Y. Zhu, D. Liu, M. Meng, Z. Hu and Z. Jiang, *ACS Catal.*, 2015, **5**, 1708–1716.
130 Z.-W. Zhou, L. Pan, Y.-T. Liu, X.-D. Zhu and X.-M. Xie, *Chem. Commun.*, 2018, **54**, 4790–4793.
131 X. Zhang, C. Wang, J. Chen, W. Zhu, A. Liao, Y. Li, J. Wang and L. Ma, *ACS Appl. Mater. Interfaces*, 2014, **6**, 20625–20633.
132 L. Zheng, X. Ye, X. Deng, Y. Wang, Y. Zhao, X. Shi and H. Zheng, *ACS Sustainable Chem. Eng.*, 2020, **8**, 15906–15914.
133 J. Zhang, Y. Tian, T. Zhang, Z. Li, X. She, Y. Wu, Y. Wang and J. Wu, *ChemCatChem*, 2020, **12**, 2760–2767.
134 N. Wan, Z. Xing, J. Kuang, Z. Li, J. Yin, Q. Zhu and W. Zhou, *Appl. Surf. Sci.*, 2018, **457**, 287–294.
135 X. Yan, Z. Xing, Y. Cao, M. Hu, Z. Li, X. Wu, Q. Zhu, S. Yang and W. Zhou, *Appl. Catal., B*, 2017, **219**, 572–579.
136 J. Hou, T. Xu, Y. Ning, B. Huang, Y. Yang and Q. Wang, *Spectrochim. Acta, Part A*, 2021, **244**, 118896.
137 X. Liu, P. Carvalho, M. Getz, T. Norby and A. Chatzitakis, *J. Phys. Chem. C*, 2019, **123**, 21931–21940.
138 J. Jiang, Z. Xing, M. Li, Z. Li, X. Wu, M. Hu, J. Wan, N. Wang, A. Besov and W. Zhou, *Ind. Eng. Chem. Res.*, 2017, **56**, 7948–7956.
139 Z. Li, H. Bian, X. Xiao, J. Shen, C. Zhao, J. Lu and Y. Li, *ACS Appl. Nano Mater.*, 2019, **2**, 7372–7378.
140 Z. Li, H. Bian, Z. Xu, J. Lu and Y. Li, *ACS Appl. Energy Mater.*, 2020, **3**, 6087–6092.
141 S. Islam, A. Reed, S. Nagpure, N. Wanninayake, J. Browning, J. Strzalka, D. Kim and S. Rankin, *Microporous Mesoporous Mater.*, 2018, **261**, 35–43.
142 X. Liu, R. Hua, J. Niu, Z. Zhang and J. Zhang, *J. Alloys Compd.*, 2021, **881**, 160509.
143 F. Teng, M. Li, C. Gao, G. Zhang, P. Zhang, Y. Wang, L. Chen and E. Xie, *Appl. Catal., B*, 2014, **148–149**, 339–343.
144 F. Bella, A. Munoz-Garcia, F. Colo, G. Meligrana, A. Lamberti, M. Destro, M. Pavone and C. Gerbaldi, *ACS Omega*, 2018, **3**, 8440–8450.
145 M. Pylnev, W.-H. Chang and M.-S. Wong, *Appl. Surf. Sci.*, 2018, **462**, 285–290.
146 M. Pylnev and M.-S. Wong, *J. Photochem. Photobiol., A*, 2019, **378**, 125–130.
147 F. Yu, C. Wang, Y. Li, H. Ma, R. Wang, Y. Liu, N. Suzuki, C. Terashima, B. Ohtani, T. Ochiai, A. Fujishima and X. Zhang, *Adv. Sci.*, 2020, **7**, 2000204.
148 H.-R. An, S. Park, J. Huh, H. Kim, Y.-C. Lee, Y. Lee, Y. Hong and H. Lee, *Appl. Catal., B*, 2017, **211**, 126–136.
149 A. Lepcha, C. Maccato, A. Mettenbörger, T. Andreu, L. Mayrhofer, M. Walter, S. Olthof, T. Ruoko, A. Klein, M. Moseler, K. Meerholz, J. Morante, D. Barreca and S. Mathur, *J. Phys. Chem. C*, 2015, **119**, 18835–18842.
150 S. Zhu, Z. Yu, L. Zhang and S. Watanabe, *ACS Appl. Nano Mater.*, 2021, **4**, 3940–3948.
151 C. Yuan, Y. Shen, C. Zhu, P. Zhu, F. Yang, J. Liu and C. An, *ACS Sustainable Chem. Eng.*, 2022, **10**, 10311–10317.
152 M. Ji, Y. Choa and Y. Lee, *Ultrason. Sonochem.*, 2021, **74**, 105557.
153 C. Fan, X. Fu, L. Shi, S. Yu, G. Qian and Z. Wang, *J. Alloys Compd.*, 2017, **703**, 96–102.
154 M. Shahrezaei, S. Hejazi, H. Kmentova, V. Sedajova, R. Zboril, A. Naldoni and S. Kment, *ACS Appl. Mater. Interfaces*, 2023, **15**, 37976–37985.
155 C. Fan, C. Chen, J. Wang, X. Fu, Z. Ren, G. Qian and Z. Wang, *Sci. Rep.*, 2015, **5**, 11712.
156 Y. Wang, M. Zu, X. Zhou, H. Lin, F. Peng and S. Zhang, *Chem. Eng. J.*, 2020, **381**, 122605.
157 X. Hou, Z. Li, L. Fan, J. Yuan, P. Lund and Y. Li, *Chem. Eng. J.*, 2021, **425**, 131415.
158 M. E. Aguirre, R. Zhou, A. Eugene, M. Guzman and M. Grela, *Appl. Catal., B*, 2017, **217**, 485–493.
159 Y. Pang, Y. Li, G. Xu, Y. Hu, Z. Kou, Q. Feng, J. Lv, Y. Zhang, J. Wang and Y. Wu, *Appl. Catal., B*, 2019, **248**, 255–263.
160 Z. Yan, W. Wang, L. Du, J. Zhu, D. Phillips and J. Xu, *Appl. Catal., B*, 2020, **275**, 119151.
161 B. Sun, N. Lu, Y. Su, H. Yu, X. Meng and Z. Gao, *Appl. Surf. Sci.*, 2017, **394**, 479–487.
162 H. Pan, X. Wang, Z. Xiong, M. Sun, M. Murugananthan and Y. Zhang, *Environ. Res.*, 2021, **198**, 111176.
163 X. Hou, K. Aitola and P. Lund, *Energy Sci. Eng.*, 2021, **9**, 921–937.
164 M. Ge, Q. Li, C. Cao, J. Huang, S. Li, S. Zhang, Z. Chen, K. Zhang, S. Al-Deyab and Y. Lai, *Adv. Sci.*, 2017, **4**, 1600152.
165 H. Hosono and M. Kitano, *Chem. Rev.*, 2021, **121**, 3121–3185.
166 S. Wu, H. Yu, S. Chen and X. Quan, *ACS Catal.*, 2020, **10**, 14380–14389.
167 Z. Chen, S. Wu, J. Ma, S. Mine, T. Toyao, M. Matsuoka, L. Wang and J. Zhang, *Angew. Chem., Int. Ed.*, 2021, **60**, 11901–11909.
168 R. Lang, W. Xi, J. Liu, Y. Cui, T. Li, A. Lee, F. Chen, Y. Chen, L. Li, L. Li, J. Lin, S. Miao, X. Liu, A. Wang, X. Wang, J. Luo, B. Qiao, J. Li and T. Zhang, *Nat. Commun.*, 2019, **10**, 234.
169 Y. Tang, C. Asokan, M. Xu, G. Graham, X. Pan, P. Christopher, J. Li and P. Sautet, *Nat. Commun.*, 2019, **10**, 4488.

170 Z. Xue, M. Yan, Y. Zhang, J. Xu, X. Gao and Y. Wu, *Appl. Catal., B*, 2023, **325**, 122303.
171 S. Wu, Z. Chen, W. Yue, S. Mine, T. Toyao, M. Matsuoka, X. Xi, L. Wang and J. Zhang, *ACS Catal.*, 2021, **11**, 4362–4371.
172 L. Chen, R. Unocic, A. Hoffman, J. Hong, A. Braga, Z. Bao, S. Bare and J. Szanyi, *JACS Au*, 2021, **1**, 977–986.
173 C. Liu, J. Qian, Y. Ye, H. Zhou, C.-J. Sun, C. Sheehan, Z. Zhang, G. Wan, Y.-S. Liu, J. Guo, S. Li, H. Shin, S. Hwang, T. Gunnoe, W. Goddard and S. Zhang, *Nat. Catal.*, 2020, **4**, 36–45.
174 Y. Zhou, Z. Xie, J. Jiang, J. Wang, X. Song, Q. He, W. Ding and Z. Wei, *Nat. Catal.*, 2020, **3**, 454–462.
175 B. Lee, S. Park, M. Kim, A. Sinha, S. Lee, E. Jung, W. Chang, K. Lee, J. Kim, S. Cho, H. Kim, K. Nam and T. Hyeon, *Nat. Mater.*, 2019, **18**, 620–626.
176 Y. Yao, L. Zhao, J. Dai, J. Wang, C. Fang, G. Zhan, Q. Zheng, W. Hou and L. Zhang, *Angew. Chem., Int. Ed.*, 2022, **61**, e202208215.
177 B. Sarma, F. Maurer, D. Doronkin and J. Grunwaldt, *Chem. Rev.*, 2023, **123**, 379–444.
178 F. Abdelghafar, X. Xu, S. Jiang and Z. Shao, *Mater. Rep.: Energy*, 2022, **2**, 100144.
179 L. Kuai, Z. Chen, S. Liu, E. Kan, N. Yu, Y. Ren, C. Fang, X. Li, Y. Li and B. Geng, *Nat. Commun.*, 2020, **11**, 48.
180 J. Liu, J. Wan, L. Liu, W. Yang, J. Low, X. Gao and F. Fu, *Chem. Eng. J.*, 2022, **430**, 133125.
181 Q. Zhang, Y. Li, M. Geng, J. Zhu, H. Sun and B. Jiang, *Appl. Catal., B*, 2023, **330**, 122658.
182 M. Ismael, *Sol. Energy*, 2020, **211**, 522–546.
183 P. Kodithuwakku, D. Jayasundara, I. Munaweera, R. Jayasinghe, T. Thoradeniya, M. Weerasekera, P. Ajayan and N. Kottegoda, *Prog. Solid State Chem.*, 2022, **67**, 100369.
184 A. Soleimani-Gorgani, H. Al-Hazmi, A. Esmaeili and S. Habibzadeh, *Environ. Res.*, 2023, **237**, 117079.
185 E. Cerrato, E. Gaggero, P. Calza and M. Paganini, *Chem. Eng. J. Adv.*, 2022, **10**, 100268.
186 M. Dozzi and E. Selli, *J. Photochem. Photobiol., C*, 2013, **14**, 13–28.
187 S. Muthukrishnan, R. Vidya and A. Sjåstad, *Mater. Chem. Phys.*, 2023, **299**, 127467.
188 T. Pawar, D. Contreras López, J. Olivares Romero and J. Vallejo Montesinos, *J. Mater. Sci.*, 2023, **58**, 6887–6930.
189 M. Coto, G. Divitini, A. Dey, S. Krishnamurthy, N. Ullah, C. Ducati and R. V. Kumar, *Mater. Today Chem.*, 2017, **4**, 142–149.
190 W. Lee, C. Lee, G. Cha, B. Lee, J. Jeong, H. Park, J. Heo, M. Bootharaju, S. Sunwoo, J. Kim, K. Ahn, D. Kim and T. Hyeon, *Nat. Nanotechnol.*, 2023, **18**, 754–762.
191 D. Hasina, M. Saini, M. Kumar, A. Mandal, N. Basu, P. Maiti, S. Srivastava and T. Som, *Small*, 2023, e2305605.
192 B. He, Z. Wang, P. Xiao, T. Chen, J. Yu and L. Zhang, *Adv. Mater.*, 2022, **34**, e2203225.
193 X. Zhang, Y. Zeng, W. Shi, Z. Tao, J. Liao, C. Ai, H. Si, Z. Wang, A. Fisher and S. Lin, *Chem. Eng. J.*, 2022, **429**, 131312.
194 M. Rajeswari, K. Vanasundari, G. Mahalakshmi, P. Ponnarasi, M. Parthibavarman, M. Shkir and I. Ashraf, *Chem. Phys. Lett.*, 2022, **805**, 139936.
195 S. Vignesh, S. Chandrasekaran, M. Srinivasan, R. Anbarasan, R. Perumalsamy, E. Arumugam, M. Shkir, H. Algarni and S. AlFaify, *Chemosphere*, 2022, **288**, 132611.
196 L. Chen, X.-L. Song, J.-T. Ren and Z.-Y. Yuan, *Appl. Catal., B*, 2022, **315**, 121546.
197 M. Mousavi, M. Soleimani, M. Hamzehloo, A. Badiei and J. Ghasemi, *Mater. Chem. Phys.*, 2021, **258**, 123912.
198 Y.-P. Zhang, W. Han, Y. Yang, H. Zhang, Y. Wang, L. Wang, X. Sun and F. Zhang, *Chem. Eng. J.*, 2022, **446**, 137213.
199 T. Nguyen, J. Li, E. Lizundia, M. Niederberger, W. Hamad and M. MacLachlan, *Adv. Funct. Mater.*, 2019, **29**, 1904639.
200 Y. Xue, F. Wang, H. Luo and J. Zhu, *ACS Appl. Mater. Interfaces*, 2019, **11**, 34355–34363.
201 Z. Xiong, Z. Lei, Y. Li, L. Dong, Y. Zhao and J. Zhang, *J. Photochem. Photobiol., C*, 2018, **36**, 24–47.
202 Y. Yamazaki, T. Toyonaga, N. Doshita, K. Mori, Y. Kuwahara, S. Yamazaki and H. Yamashita, *ACS Appl. Mater. Interfaces*, 2022, **14**, 2291–2300.
203 P. Bousoulas, P. Asenov, I. Karageorgiou, D. Sakellaropoulos, S. Stathopoulos and D. Tsoukalas, *J. Appl. Phys.*, 2016, **120**, 154501.
204 C. Wen, H. Jiang, S. Qiao, H. Yang and G. Lu, *J. Mater. Chem.*, 2011, **21**, 7052–7061.
205 D. Wang, T. Sheng, J. Chen, H.-F. Wang and P. Hu, *Nat. Catal.*, 2018, **1**, 291–299.
206 S. Lu, B. Weng, A. Chen, X. Li, H. Huang, X. Sun, W. Feng, Y. Lei, Q. Qian and M. Yang, *ACS Appl. Mater. Interfaces*, 2021, **13**, 13044–13054.
207 J. DuChene, G. Tagliabue, A. Welch, W. Cheng and H. Atwater, *Nano Lett.*, 2018, **18**, 2545–2550.
208 L. Putri, B. Ng, W. Ong, S. Chai and A. Mohamed, *Adv. Energy Mater.*, 2022, **12**, 2201093.
209 X. Du, Y. Huang, X. Pan, B. Han, Y. Su, Q. Jiang, M. Li, H. Tang, G. Li and B. Qiao, *Nat. Commun.*, 2020, **11**, 5811.
210 Y. Zhang, J. Liu, K. Qian, A. Jia, D. Li, L. Shi, J. Hu, J. Zhu and W. Huang, *Angew. Chem., Int. Ed.*, 2021, **60**, 12074–12081.
211 S. Wang, G. Liu and L. Wang, *Chem. Rev.*, 2019, **119**, 5192–5247.
212 M. Malizia, B. Seger, I. Chorkendorff and P. Vesborg, *J. Mater. Chem. A*, 2014, **2**, 6847–6853.
213 Z. Tian, Y. Da, M. Wang, X. Dou, X. Cui, J. Chen, R. Jiang, S. Xi, B. Cui, Y. Luo, H. Yang, Y. Long, Y. Xiao and W. Chen, *Nat. Commun.*, 2023, **14**, 142.
214 G. Ren, M. Shi, S. Liu, Z. Li, Z. Zhang and X. Meng, *Chem. Eng. J.*, 2023, **454**, 140158.
215 Y. Guo, Y. Huang, B. Zeng, B. Han, M. Akri, M. Shi, Y. Zhao, Q. Li, Y. Su, L. Li, Q. Jiang, Y. Cui, L. Li, R. Li, B. Qiao and T. Zhang, *Nat. Commun.*, 2022, **13**, 2648.
216 K. Fujiwara and S. Pratsinis, *Appl. Catal., B*, 2018, **226**, 127–134.
217 J. Chen, Y. Kang, W. Zhang, Z. Zhang, Y. Chen, Y. Yang, L. Duan, Y. Li and W. Li, *Angew. Chem., Int. Ed.*, 2022, **61**, e202203022.

218 J. Wan, W. Chen, C. Jia, L. Zheng, J. Dong, X. Zheng, Y. Wang, W. Yan, C. Chen, Q. Peng, D. Wang and Y. Li, *Adv. Mater.*, 2018, **30**, 1705369.
219 K. Selvakumar, T. Oh, Y. Wang, M. Arunpandian and M. Swaminathan, *Chemosphere*, 2023, **314**, 137694.
220 D. Prashad Ojha, M. Babu Poudel and H. Joo Kim, *Mater. Lett.*, 2020, **264**, 127363.
221 L. Zheng, H. Su, J. Zhang, L. Walekar, H. Vafaei Molamahmood, B. Zhou, M. Long and Y. Hu, *Appl. Catal., B*, 2018, **239**, 475–484.
222 S. Parmar, T. Das, B. Ray, B. Debnath, S. Gosavi, G. Shanker, S. Datar, S. Chakraborty and S. Ogale, *Adv. Energy Sustainability Res.*, 2021, **3**, 2100137.
223 Z. Wu, P. Yang, Q. Li, W. Xiao, Z. Li, G. Xu, F. Liu, B. Jia, T. Ma, S. Feng and L. Wang, *Angew. Chem., Int. Ed.*, 2023, **62**, e202300406.
224 Z. Huang, Q. Sun, K. Lv, Z. Zhang, M. Li and B. Li, *Appl. Catal., B*, 2015, **164**, 420–427.
225 Z. Li, H. Li, S. Wang, F. Yang and W. Zhou, *Chem. Eng. J.*, 2022, **427**, 131830.
226 A. Hezam, K. Alkanad, M. A. Bajiri, J. Strunk, K. Takahashi, Q. Drmosh, N. Al-Zaqri and L. Krishnappagowda, *Small Methods*, 2023, **7**, e2201103.
227 D.-H. Yoon, M. Biswas and A. Sakthisabarimoorthi, *Diamond Relat. Mater.*, 2022, **129**, 109363.
228 C. Qiang, N. Li, S. Zuo, Z. Guo, W. Zhan, Z. Li and J. Ma, *Sep. Purif. Technol.*, 2022, **283**, 120214.
229 J. Zhou, M. Guo, L. Wang, Y. Ding, Z. Zhang, Y. Tang, C. Liu and S. Luo, *Chem. Eng. J.*, 2019, **366**, 163–171.
230 J. Pan, Z. Dong, B. Wang, Z. Jiang, C. Zhao, J. Wang, C. Song, Y. Zheng and C. Li, *Appl. Catal., B*, 2019, **242**, 92–99.
231 J. Lin, W. Ren, A. Li, C. Yao, T. Chen, X. Ma, X. Wang and A. Wu, *ACS Appl. Mater. Interfaces*, 2020, **12**, 4204–4211.
232 R. Nawaz, S. Haider, H. Ullah, M. Akhtar, S. Khan, M. Junaid and N. Khan, *J. Environ. Chem. Eng.*, 2022, **10**, 106968.
233 X. Shi, Z. Liu, X. Li, W. You, Z. Shao and R. Che, *Chem. Eng. J.*, 2021, **419**, 130020.
234 V. Navakoteswara Rao, N. Lakshmana Reddy, M. Mamatha Kumari, P. Ravi, M. Sathish, K. Kuruvilla, V. Preethi, K. Reddy, N. Shetti, T. Aminabhavi and M. Shankar, *Appl. Catal., B*, 2019, **254**, 174–185.
235 X. Lu, A. Chen, Y. Luo, P. Lu, Y. Dai, E. Enriquez, P. Dowden, H. Xu, P. Kotula, A. Azad, D. Yarotski, R. Prasankumar, A. Taylor, J. Thompson and Q. Jia, *Nano Lett.*, 2016, **16**, 5751–5755.
236 K. Kato, Y. Xin, S. Vaucher and T. Shirai, *Scr. Mater.*, 2022, **208**, 114358.
237 G. Liu, H. Yang, X. Wang, L. Cheng, H. Lu, L. Wang, G. Lu and H. Cheng, *J. Phys. Chem. C*, 2009, **113**, 21784–21788.
238 A. Wang, S. Wu, J. Dong, R. Wang, J. Wang, J. Zhang, S. Zhong and S. Bai, *Chem. Eng. J.*, 2021, **404**, 127145.
239 Q. Shi, Y. Li, Y. Zhou, S. Miao, N. Ta, E. Zhan, J. Liu and W. Shen, *J. Mater. Chem. A*, 2015, **3**, 14409–14415.
240 W. Zhang, J. Xue, Q. Shen, S. Jia, J. Gao, X. Liu and H. Jia, *J. Alloys Compd.*, 2021, **870**, 159400.
241 F. Ullah, R. Bashiri, N. Muti Mohamed, A. Zaleska-Medynska, C. Kait, U. Ghani, M. Shahid and M. Saheed, *Appl. Surf. Sci.*, 2022, **576**, 151871.
242 B. Kakavandi, E. Dehghanifard, P. Gholami, M. Noorisepehr and B. MirzaHedayat, *Appl. Surf. Sci.*, 2021, **570**, 151145.
243 C. Wang, J. Li, E. Paineau, H. Remita and M. Ghazzal, *Sol. RRL*, 2023, **7**, 2200929.
244 S. Lee, H. Bae and W. Choi, *Acc. Chem. Res.*, 2023, **56**, 867–877.
245 C. Luo, X. Ren, Z. Dai, Y. Zhang, X. Qi and C. Pan, *ACS Appl. Mater. Interfaces*, 2017, **9**, 23265–23286.
246 C. Foo, Y. Li, K. Lebedev, T. Chen, S. Day, C. Tang and E. Tsang, *Nat. Commun.*, 2021, **12**, 661.
247 C. Holder and R. Schaak, *ACS Nano*, 2019, **13**, 7359–7365.
248 A. Arif, R. Balgis, T. Ogi, F. Iskandar, A. Kinoshita, K. Nakamura and K. Okuyama, *Sci. Rep.*, 2017, **7**, 3646.
249 L. Guo, Y. Jing and B. Chaplin, *Environ. Sci. Technol.*, 2016, **50**, 1428–1436.
250 Z. Wu, P. Yang, Q. Li, W. Xiao, Z. Li, G. Xu, F. Liu, B. Jia, T. Ma, S. Feng and L. Wang, *Angew. Chem., Int. Ed.*, 2023, **62**, e202300406.
251 A. Smith and S. Nie, *Acc. Chem. Res.*, 2010, **43**, 190–200.
252 Z. Chen, S. Mo, H. Lin, Z. Wu, Y. Zhao, X. Hua and P. Zhao, *Cell Rep. Phys. Sci.*, 2023, 101681.
253 M. Terban and S. Billinge, *Chem. Rev.*, 2022, **122**, 1208–1272.
254 S. Billinge, *Philos. Trans. R. Soc., A*, 2019, **377**, 20180413.
255 S. Zhang, J. Gong, D. Xiao, B. Jayan and A. McGaughey, *Comput. Mater. Sci.*, 2023, **218**, 111964.
256 X. Hua, Z. Liu, M. Fischer, O. Borkiewicz, P. Chupas, K. Chapman, U. Steiner, P. Bruce and C. Grey, *J. Am. Chem. Soc.*, 2017, **139**, 13330–13341.
257 X. Hua, Z. Liu, P. G. Bruce and C. P. Grey, *J. Am. Chem. Soc.*, 2015, **137**, 13612–13623.
258 T.-D. Nguyen-Phan, Z. Liu, S. Luo, A. Gamalski, D. Vovchok, W. Xu, E. Stach, D. Polyansky, E. Fujita, J. Rodriguez and S. Senanayake, *J. Phys. Chem. C*, 2016, **120**, 3472–3482.
259 F. Haase, A. Bergmann, T. Jones, J. Timoshenko, A. Herzog, H. Jeon, C. Rettenmaier and B. Cuenya, *Nat. Energy*, 2022, **7**, 765–773.
260 X. Lv, X. Li, C. Yang, X. Ding, Y. Zhang, Y. Z. Zheng, S. Li, X. Sun and X. Tao, *Adv. Funct. Mater.*, 2020, **30**, 1910830.
261 Y. Li, S. Wang, Y. Dong, P. Mu, Y. Yang, X. Liu, C. Lin and Q. Huang, *Bioact. Mater.*, 2020, **5**, 1062–1070.
262 C. Roy, B. Sebok, S. Scott, E. Fiordaliso, J. Sørensen, A. Bodin, D. Trimarco, C. Damsgaard, P. Vesborg, O. Hansen, I. Stephens, J. Kibsgaard and I. Chorkendorff, *Nat. Catal.*, 2018, **1**, 820–829.
263 A. Grisafi, J. Nigam and M. Ceriotti, *Chem. Sci.*, 2021, **12**, 2078–2090.
264 T.-T. Wei, F.-F. Wang, X.-Z. Li, J.-H. Zhang, Y.-R. Zhu and T.-F. Yi, *Sustainable Mater. Technol.*, 2021, **30**, e00355.
265 X. Zhang, W. Hu, K. Zhang, J. Wang, B. Sun, H. Li, P. Qiao, L. Wang and W. Zhou, *ACS Sustainable Chem. Eng.*, 2017, **5**, 6894–6901.

266 N. Dwivedi, R. Yeo, H. Tan, R. Stangl, A. Aberle, C. Bhatia, A. Danner and B. Liao, *Adv. Funct. Mater.*, 2018, **28**, 1707018.
267 T. Mochizuki, K. Gotoh, Y. Kurokawa, T. Yamamoto and N. Usami, *Adv. Mater. Interfaces*, 2018, **6**, 1801645.
268 M. Barzilay, T. Qiu, A. Rappe and Y. Ivry, *Adv. Funct. Mater.*, 2019, **30**, 1902549.
269 L. Zhou, Y. Shao, F. Yin, J. Li, F. Kang and R. Lv, *Nat. Commun.*, 2023, **14**, 7644.
270 M. Yuan, M. Kermanian, T. Agarwal, Z. Yang, S. Yousefiasl, Z. Cheng, P. Ma, J. Lin and A. Maleki, *Adv. Mater.*, 2023, **35**, e2304176.
271 C. Christensen, M. Mamakhel, A. Balakrishna, B. Iversen, Y. Chiang and D. Ravnsbaek, *Nanoscale*, 2019, **11**, 12347–12357.
272 J. Gao, J. Xue, S. Jia, Q. Shen, X. Zhang, H. Jia, X. Liu, Q. Li and Y. Wu, *ACS Appl. Mater. Interfaces*, 2021, **13**, 18758–18771.
273 M. Yazdanpanah, M. Fereidooni, V. Marquez, C. Paz, T. Saelee, M. Salazar Villanueva, M. Rittiruam, P. Khajondetchairit, S. Praserthdam and P. Praserthdam, *ChemSusChem*, 2023, e202301033.
274 H. Chen, J. Li, W. Yang, S. Balaghi, C. Triana, C. Mavrokefalos and G. Patzke, *ACS Catal.*, 2021, **11**, 7637–7646.
275 J. Kang, Y. Zhang, Z. Chai, X. Qiu, X. Cao, P. Zhang, G. Teobaldi, L. Liu and L. Guo, *Adv. Mater.*, 2021, **33**, e2100407.
276 M. Pisarek, M. Krawczyk, M. Holdynski and W. Lisowski, *ACS Omega*, 2020, **5**, 8647–8658.
277 G. Jia, Y. Wang, X. Cui, H. Zhang, J. Zhao, L. H. Li, L. Gu, Q. Zhang, L. Zheng, J. Wu, Q. Wu, D. Singh, W. Li, L. Zhang and W. Zheng, *Matter*, 2022, **5**, 206–218.
278 C. Chen, M. Wu, C. Yang, X. Yu, J. Yu, H. Yin, G. Li, G. Su, Z. Hao, M. Song and C. Ma, *Cell Rep. Phys. Sci.*, 2022, **3**, 100936.
279 S. Zhang, J. Gong, S. Chu, D. Xiao, B. Reeja-Jayan and A. McGaughey, *APL Mach. Learn.*, 2023, **1**, 026115.
280 C. Mao, J. Wang, Y. Zou, G. Qi, J. Yang Loh, T. Zhang, M. Xia, J. Xu, F. Deng, M. Ghoussoub, N. Kherani, L. Wang, H. Shang, M. Li, J. Li, X. Liu, Z. Ai, G. Ozin, J. Zhao and L. Zhang, *J. Am. Chem. Soc.*, 2020, **142**, 17403–17412.
281 J. Chapman, K. Kweon, Y. Zhu, K. Bushick, L. Bayu Aji, C. Colla, H. Mason, N. Goldman, N. Keilbart, S. Qiu, T. Heo, J. Rodriguez and B. Wood, *J. Mater. Chem. A*, 2023, **11**, 8670–8683.
282 S. Selcuk, X. Zhao and A. Selloni, *Nat. Mater.*, 2018, **17**, 923–928.
283 J. Bae, D. Kim, H. Yoo, E. Park, Y. Lim, M. Park, Y. Kim and H. Kim, *ACS Appl. Mater. Interfaces*, 2016, **8**, 4541–4547.
284 C. Xue, R. Huang, R. Xue, Q. Chang, N. Li, J. Zhang, S. Hu and J. Yang, *J. Alloys Compd.*, 2022, **909**, 164843.
285 H. Sugiyama, T. Nakao, M. Miyazaki, H. Abe, Y. Niwa, M. Kitano and H. Hosono, *ACS Catal.*, 2022, **12**, 12572–12581.
286 R. Lakra, R. Kumar, P. Sahoo, D. Thatoi and A. Soam, *Inorg. Chem. Commun.*, 2021, **133**, 108929.
287 Y. Zhang, Y. Li, H. Yu, K. Yu and H. Yu, *J. Mater. Sci. Technol.*, 2022, **106**, 139–146.
288 R. Wang, X. Xue, W. Lu, H. Liu, C. Lai, K. Xi, Y. Che, J. Liu, S. Guo and D. Yang, *Nanoscale*, 2015, **7**, 12833–12838.
289 Y. Yang, P. Gao, Y. Wang, L. Sha, X. Ren, J. Zhang, Y. Chen, T. Wu, P. Yang and X. Li, *Nano Energy*, 2017, **33**, 29–36.
290 Y. Yoshida, S. Tokashiki, K. Kubota, R. Shiratuchi, Y. Yamaguchi, M. Kono and S. Hayase, *Sol. Energy Mater. Sol. Cells*, 2008, **92**, 646–650.
291 D. Liu, Q. Yu, S. Liu, K. Qian, S. Wang, W. Sun, X.-Q. Yang, F. Kang and B. Li, *J. Phys. Chem. C*, 2019, **123**, 12797–12806.
292 G. Cha, S. Mohajernia, N. Nguyen, A. Mazare, N. Denisov, I. Hwang and P. Schmuki, *Adv. Energy Mater.*, 2019, **10**, 1903448.
293 J. Balajka, M. Hines, W. DeBenedetti, M. Komora, J. Pavelec, M. Schmid and U. Diebold, *Science*, 2018, **361**, 786–789.
294 D. Barauskas, M. Dzikaras, D. Bieliauskas, D. Pelenis, G. Vanagas and D. Viržonis, *Sensors*, 2020, **20**, 3554.
295 W. Wang, T. Xu, J. Chen, J. Shangguan, H. Dong, H. Ma, Q. Zhang, J. Yang, T. Bai, Z. Guo, H. Fang, H. Zheng and L. Sun, *Nat. Mater.*, 2022, **21**, 859–863.
296 Y. Li, Y. Peng, L. Hu, J. Zheng, D. Prabhakaran, S. Wu, T. Puchtler, M. Li, K. Wong, R. Taylor and E. Tsang, *Nat. Commun.*, 2019, **10**, 4421.
297 Y. Li, H. Zhou, S. Cai, D. Prabhakaran, W. Niu, A. Large, G. Held, R. Taylor, X. Wu and E. Tsang, *Nat. Catal.*, 2024, **7**, 77–88.
298 M. Xing, J. Zhang, B. Qiu, B. Tian, M. Anpo and M. Che, *Small*, 2015, **11**, 1920–1929.
299 H. Wang, H. Qi, X. Sun, S. Jia, X. Li, T. Miao, L. Xiong, S. Wang, X. Zhang, X. Liu, A. Wang, T. Zhang, W. Huang and J. Tang, *Nat. Mater.*, 2023, **22**, 619–626.
300 C. Kim, S. Kim, J. Lee, J. Kim and J. Yoon, *ACS Appl. Mater. Interfaces*, 2015, **7**, 7486–7491.
301 A. Tighineanu, T. Ruff, S. Albu, R. Hahn and P. Schmuki, *Chem. Phys. Lett.*, 2010, **494**, 260–263.
302 M. Sboui, W. Niu, G. Lu, K. Zhang and J. Pan, *Chemosphere*, 2023, **310**, 136753.
303 J. Liu, J. Yan, Q. Shi, H. Dong, J. Zhang, Z. Wang, W. Huang, B. Chen and H. Zhang, *J. Phys. Chem. C*, 2019, **123**, 4094–4102.
304 S. K. Kajli, D. Ray and S. Roy, *Nanoscale Adv.*, 2021, **3**, 432–445.
305 H. Huang, X. Hou, J. Xiao, L. Zhao, Q. Huang, H. Chen and Y. Li, *Catal. Today*, 2019, **330**, 189–194.
306 X. Guan, S. Shen and S. Mao, *Cell Rep. Phys. Sci.*, 2023, **4**, 101211.
307 A. Fujishima and K. Honda, *Nature*, 1972, **238**, 37–38.
308 A. Behera, A. Kar and R. Srivastava, *Inorg. Chem.*, 2022, **61**, 12781–12796.
309 F. Guzman, S. Chuang and C. Yang, *Ind. Eng. Chem. Res.*, 2013, **52**, 61–65.
310 Z. Haider and Y. Kang, *ACS Appl. Mater. Interfaces*, 2014, **6**, 10342–10352.
311 R. Shi, H. Ye, F. Liang, Z. Wang, K. Li, Y. Weng, Z. Lin, W. Fu, C. Che and Y. Chen, *Adv. Mater.*, 2018, **30**, 1705941.

312 W. Zhou, W. Li, J. Wang, Y. Qu, Y. Yang, Y. Xie, K. Zhang, L. Wang, H. Fu and D. Zhao, *J. Am. Chem. Soc.*, 2014, **136**, 9280–9283.
313 B. Sun, W. Zhou, H. Li, L. Ren, P. Qiao, W. Li and H. Fu, *Adv. Mater.*, 2018, **30**, 1804282.
314 S. Lin, H. Huang, T. Ma and Y. Zhang, *Adv. Sci.*, 2020, **8**, 2002458.
315 N. Liu, S. Mohajernia, N. Nguyen, S. Hejazi, F. Plass, A. Kahnt, T. Yokosawa, A. Osvet, E. Spiecker, D. Guldi and P. Schmuki, *ChemSusChem*, 2020, **13**, 4937–4944.
316 A. Juliya, V. Mujeeb, K. Sreenivasan and K. Muraleedharan, *J. Photochem. Photobiol.*, 2021, **8**, 100076.
317 Q. Liu, D. Ding, C. Ning and X. Wang, *Int. J. Hydrogen Energy*, 2015, **40**, 2107–2114.
318 K. Shin and J. Park, *ACS Appl. Mater. Interfaces*, 2015, **7**, 18429–18434.
319 S. Lin, H. Ren, Z. Wu, L. Sun, X.-G. Zhang, Y.-M. Lin, K. H. Zhang, C.-J. Lin, Z.-Q. Tian and J.-F. Li, *J. Energy Chem.*, 2021, **59**, 721–729.
320 F. Dingenen and S. Verbruggen, *Renewable Sustainable Energy Rev.*, 2021, **142**, 110866.
321 A. Shih, M. Monteiro, F. Dattila, D. Pavesi, M. Philips, A. da Silva, R. Vos, K. Ojha, S. Park, O. van der Heijden, G. Marcandalli, A. Goyal, M. Villalba, X. Chen, G. Gunasooriya, I. McCrum, R. Mom, N. López and M. Koper, *Nat. Rev. Methods Primers*, 2022, **2**, 84.
322 H. Zhao and Z. Yuan, *Adv. Energy Mater.*, 2023, **13**, 2300254.
323 LENNECH, **https://www.lenntech.com/applications**, (accessed August 2024).
324 X. Ren, J. Zhou, X. Qi, Y. Liu, Z. Huang, Z. Li, Y. Ge, S. Dhanabalan, J. Ponraj, S. Wang, J. Zhong and H. Zhang, *Adv. Energy Mater.*, 2017, **7**, 1700396.
325 J. Hausmann, R. Schlögl, P. Menezes and M. Driess, *Energy Environ. Sci.*, 2021, **14**, 3679–3685.
326 M. Yesupatham, A. Augustin, N. Agamendran, B. Honnappa, M. Shanmugam, P. Sagayaraj, G. Thennarasu, N. Sagaya Selvam and K. Sekar, *Sustainable Energy Fuels*, 2023, **7**, 4727–4757.
327 S. Lv, Y. Wang, Y. Zhou, Q. Liu, C. Song and D. Wang, *J. Alloys Compd.*, 2021, **868**, 159144.
328 S. Xiao, S. Wu, L. Wu, Y. Dong, J. Liu, L. Wang, X. Chen, Y. Wang, G. Tian, G. Chang, M. Shalom, P. Fornasiero and X. Yang, *ACS Nano*, 2023, **17**, 18217–18226.
329 M. Khan, T. Al-Attas, S. Roy, M. Rahman, N. Ghaffour, V. Thangadurai, S. Larter, J. Hu, P. Ajayan and M. Kibria, *Energy Environ. Sci.*, 2021, **14**, 4831–4839.
330 F. Dionigi, T. Reier, Z. Pawolek, M. Gliech and P. Strasser, *ChemSusChem*, 2016, **9**, 962–972.
331 Z. Zhu, H. Zheng, H. Kong, X. Ma and J. Xiong, *Nat. Water*, 2023, **1**, 790–799.
332 T. Suguro, F. Kishimoto, N. Kariya, T. Fukui, M. Nakabayashi, N. Shibata, T. Takata, K. Domen and K. Takanabe, *Nat. Commun.*, 2022, **13**, 5698.
333 H. Xie, Z. Zhao, T. Liu, Y. Wu, C. Lan, W. Jiang, L. Zhu, Y. Wang, D. Yang and Z. Shao, *Nature*, 2022, **612**, 673–678.
334 J. Liu, Y. Zou, B. Jin, K. Zhang and J. Park, *ACS Energy Lett.*, 2019, **4**, 3018–3027.
335 J. Tang, T. Zhao, D. Solanki, X. Miao, W. Zhou and S. Hu, *Joule*, 2021, **5**, 1432–1461.
336 J. Zhang, W. Hu, S. Cao and L. Piao, *Nano Res.*, 2020, **13**, 2313–2322.
337 J. Zhang, Y. Lei, S. Cao, W. Hu, L. Piao and X. Chen, *Nano Res.*, 2021, **15**, 2013–2022.
338 Y. Hong, Y. Cho, E. Go, P. Sharma, H. Cho, B. Lee, S. Lee, S. Park, M. Ko, S. Kwak, C. Yang and J.-W. Jang, *Chem. Eng. J.*, 2021, **418**, 129346.
339 Y. Yang, B. Zhu, L. Wang, B. Cheng, L. Zhang and J. Yu, *Appl. Catal., B*, 2022, **317**, 121788.
340 S. Yu, X. Cheng, Y. Wang, B. Xiao, Y. Xing, J. Ren, Y. Lu, H. Li, C. Zhuang and G. Chen, *Nat. Commun.*, 2022, **13**, 4737.
341 G. Wang, H. Wang, Y. Ling, Y. Tang, X. Yang, R. Fitzmorris, C. Wang, J. Zhang and Y. Li, *Nano Lett.*, 2011, **11**, 3026–3033.
342 X. Hou, K. Aitola, H. Jiang, P. Lund and Y. Li, *Catal. Today*, 2021, **402**, 3–9.
343 X. Shi, S. Back, T. Gill, S. Siahrostami and X. Zheng, *Chem*, 2021, **7**, 38–63.
344 Y. Xue, Y. Wang, Z. Pan and K. Sayama, *Angew. Chem., Int. Ed.*, 2021, **60**, 10469–10480.
345 S. Xue, L. Tang, Y. Tang, C. Li, M. Li, J. Zhou, W. Chen, F. Zhu and J. Jiang, *ACS Appl. Mater. Interfaces*, 2020, **12**, 4423–4431.
346 W. Liu, H. Liu and Z. Ai, *J. Hazard. Mater.*, 2015, **288**, 97–103.
347 Z. Xu, J. Liang, Y. Wang, K. Dong, X. Shi, Q. Liu, Y. Luo, T. Li, Y. Jia, A. Asiri, Z. Feng, Y. Wang, D. Ma and X. Sun, *ACS Appl. Mater. Interfaces*, 2021, **13**, 33182–33187.
348 T. u Haq, M. Pasha, Y. Tong, S. Mansour and Y. Haik, *Appl. Catal., B*, 2022, **301**, 120836.
349 CO_2 earth, **https://www.co2.earth**, (accessed August 2024).
350 R. Sharifian, R. Wagterveld, I. Digdaya, C. Xiang and D. Vermaas, *Energy Environ. Sci.*, 2021, **14**, 781–814.
351 Y. Li, Z. Zeng, Y. Zhang, Y. Chen, W. Wang, X. Xu, M. Du, Z. Li and Z. Zou, *ACS Sustainable Chem. Eng.*, 2022, **10**, 6382–6388.
352 Y. Park, D. Kim, C. Hiragond, J. Lee, J.-W. Jung, C.-H. Cho, I. In and S.-I. In, *J. CO2 Util.*, 2023, **67**, 102324.
353 J. Low, S. Qiu, D. Xu, C. Jiang and B. Cheng, *Appl. Surf. Sci.*, 2018, **434**, 423–432.
354 J. Low, L. Zhang, B. Zhu, Z. Liu and J. Yu, *ACS Sustainable Chem. Eng.*, 2018, **6**, 15653–15661.
355 M. Zubair, H. Kim, A. Razzaq, C. Grimes and S.-I. In, *J. CO2 Util.*, 2018, **26**, 70–79.
356 J. Liu, H. Shi, Q. Shen, C. Guo and G. Zhao, *Appl. Catal., B*, 2017, **210**, 368–378.
357 L. Zhang, H. Cao, Q. Pen, L. Wu, G. Hou, Y. Tang and G. Zheng, *Electrochim. Acta*, 2018, **283**, 1507–1513.
358 J. Perini, L. Torquato, K. Irikura and M. Zanoni, *J. CO2 Util.*, 2019, **34**, 596–605.
359 J. Wu, Y. Feng, B. Logan, C. Dai, X. Han, D. Li and J. Liu, *ACS Sustainable Chem. Eng.*, 2019, **7**, 15289–15296.
360 M. de Souza, E. Cardoso, G. Fortunato, M. Lanza, C. Nazário, M. Zanoni, G. Maia and J. Cardoso, *J. Environ. Chem. Eng.*, 2021, **9**, 105803.

361 M. Zhang, J. Cheng, X. Xuan, J. Zhou and K. Cen, *ACS Sustainable Chem. Eng.*, 2016, **4**, 6344–6354.
362 F. Fu, I. Shown, C. Li, P. Raghunath, T. Lin, T. Billo, H. Wu, C. Wu, P. Chung, M. Lin, L. Chen and K. Chen, *ACS Appl. Mater. Interfaces*, 2019, **11**, 25186–25194.
363 Y. Xia, M. Tang, L. Zhang, J. Liu, C. Jiang, G. Gao, L. Dong, L. Xie and Y. Lan, *Nat. Commun.*, 2022, **13**, 2964.
364 M. Li, L. Shen and M.-Q. Yang, *Trans. Tianjin Univ.*, 2022, **28**, 506–532.
365 V. Kumaravel, J. Bartlett and S. Pillai, *ACS Energy Lett.*, 2020, **5**, 486–519.
366 W. Zhang, Z. Jin and Z. Chen, *Adv. Sci.*, 2022, **9**, e2105204.
367 T. Billo, F. Fu, P. Raghunath, I. Shown, W. Chen, H. Lien, T. Shen, J. Lee, T. Chan, K. Huang, C. Wu, M. Lin, J. Hwang, C. Lee, L. Chen and K. Chen, *Small*, 2018, **14**, 1702928.
368 Y. Hwang, S. Sorcar, J. Lee, J. Jung, C. Cho and S.-I. In, *J. Power Sources*, 2023, **556**, 232430.
369 T. Dong, X. Liu, Z. Tang, H. Yuan, D. Jiang, Y. Wang, Z. Liu, X. Zhang, S. Huang, H. Liu, L. Zhao and W. Zhou, *Appl. Catal., B*, 2023, **326**, 122176.
370 Y. Liu, M. Xia, D. Ren, S. Nussbaum, J. H. Yum, M. Gratzel, N. Guijarro and K. Sivula, *ACS Energy Lett.*, 2023, **8**, 1645–1651.
371 H. Lin, S. Luo, H. Zhang and J. Ye, *Joule*, 2022, **6**, 294–314.
372 C. Fu, F. Li, J. Zhang, D. Li, K. Qian, Y. Liu, J. Tang, F. Fan, Q. Zhang, X. Gong and W. Huang, *Angew. Chem., Int. Ed.*, 2021, **60**, 6160–6169.
373 S. Funk, B. Hokkanen, E. Johnson and U. Burghaus, *Chem. Phys. Lett.*, 2006, **422**, 461–465.
374 H. Zhang, Y. Li, J. Wang, N. Wu, H. Sheng, C. Chen and J. Zhao, *Appl. Catal., B*, 2021, **284**, 119692.
375 J. Lin, T. Wang, J. Zhou, X. Wu, Z. Ma and S. Liu, *Appl. Catal., B*, 2023, **324**, 122234.
376 J. Fan, L. Cheng, J. Fan, Q. Wang, M. Gao, D. Li and J. Feng, *J. CO2 Util.*, 2023, **67**, 102333.
377 B. Ni, H. Jiang, W. Guo, Q. Xu and Y. Min, *Appl. Catal., B*, 2022, **307**, 121141.
378 S. Nitopi, E. Bertheussen, S. Scott, X. Liu, A. Engstfeld, S. Horch, B. Seger, I. Stephens, K. Chan, C. Hahn, J. Norskov, T. Jaramillo and I. Chorkendorff, *Chem. Rev.*, 2019, **119**, 7610–7672.
379 L. Zhang, H. Cao, Y. Lu, H. Zhang, G. Hou, Y. Tang and G. Zheng, *J. Colloid Interface Sci.*, 2020, **568**, 198–206.
380 Y. Wang, P. Gao, B. Li, Z. Yin, L. Feng, Y. Liu, Z. Du and L. Zhang, *Chemosphere*, 2022, **291**, 133007.
381 H. Iriawan, S. Andersen, X. Zhang, B. Comer, J. Barrio, P. Chen, A. Medford, I. Stephens, I. Chorkendorff and Y. Shao-Horn, *Nat. Rev. Methods Primers*, 2021, **1**, 56.
382 S. Han, H. Li, T. Li, F. Chen, R. Yang, Y. Yu and B. Zhang, *Nat. Catal.*, 2023, **6**, 402–414.
383 H. Hirakawa, M. Hashimoto, Y. Shiraishi and T. Hirai, *J. Am. Chem. Soc.*, 2017, **139**, 10929–10936.
384 R. Urrego-Ortiz, S. Builes and F. Calle-Vallejo, *ACS Catal.*, 2022, **12**, 4784–4791.
385 J. Fu, Y. Zhou, M. Saccoccio, S. Li, R. Sažinas, K. Li, S. Andersen, A. Xu, N. Deissler, J. Mygind, C. Wei, J. Kibsgaard, P. Vesborg, J. Nørskov and I. Chorkendorff, *Science*, 2023, **379**, 707–712.
386 S. Lin, X. Zhang, L. Chen, Q. Zhang, L. Ma and J. Liu, *Green Chem.*, 2022, **24**, 9003–9026.
387 J. Z. Bao, H. Maimaiti, X.-W. Zhao, J.-Y. Sun and L.-R. Feng, *Appl. Surf. Sci.*, 2022, **602**, 154328.
388 Q. Han, C. Wu, H. Jiao, R. Xu, Y. Wang, J. Xie, Q. Guo and J. Tang, *Adv. Mater.*, 2021, **33**, e2008180.
389 K. Chen, X. Xu, Q. Mei, J. Huang, G. Yang and Q. Wang, *Appl. Catal., B*, 2024, **341**, 123299.
390 X. Huang, F. Dong, G. Zhang, Y. Guo and Z. Tang, *Chem. Eng. J.*, 2021, **419**, 129572.
391 H. Shen, C. Choi, J. Masa, X. Li, J. Qiu, Y. Jung and Z. Sun, *Chem*, 2021, **7**, 1708–1754.
392 D. Ye and E. Tsang, *Nat. Synth.*, 2023, **2**, 612–623.
393 H. Fang, D. Liu, Y. Luo, Y. Zhou, S. Liang, X. Wang, B. Lin and L. Jiang, *ACS Catal.*, 2022, **12**, 3938–3954.
394 N. Cao, Z. Chen, K. Zang, J. Xu, J. Zhong, J. Luo, X. Xu and G. Zheng, *Nat. Commun.*, 2019, **10**, 2877.
395 C. Li, T. Wang, Z. Zhao, W. Yang, J. Li, A. Li, Z. Yang, G. Ozin and J. Gong, *Angew. Chem., Int. Ed.*, 2018, **57**, 5278–5282.
396 X. Li, Z. Wu, Y. Zeng, J. Han, S. Zhang and Q. Zhong, *Chem. Phys. Lett.*, 2020, **750**, 137494.
397 X. Wu, J. Li, R. Zhong, S. Liu, F. Huang, Q. Yang, B. Zhang, X. Wang and F. Zhang, *Adv. Funct. Mater.*, 2024, 2405868.
398 A. Mirzaei, M. Eddah, S. Roualdes, D. Ma and M. Chaker, *Chem. Eng. J.*, 2021, **422**, 130507.
399 Y. Shu, J. Ji, M. Zhou, S. Liang, Q. Xie, S. Li, B. Liu, J. Deng, J. Cao, S. Liu and H. Huang, *Appl. Catal., B*, 2022, **300**, 120688.
400 Y. Liu, P. Deng, R. Wu, R. Geioushy, Y. Li, Y. Liu, F. Zhou, H. Li and C. Sun, *Front. Phys.*, 2021, **16**, 53503.
401 R. Guan, X. Cheng, Y. Chen, Z. Wu, Z. Zhao, Q. Shang, Y. Sun and Z. Sun, *Nano Res.*, 2023, **16**, 10770–10778.
402 C. Mao, H. Li, H. Gu, J. Wang, Y. Zou, G. Qi, J. Xu, F. Deng, W. Shen, J. Li, S. Liu, J. Zhao and L. Zhang, *Chem*, 2019, **5**, 2702–2717.
403 C. Tang, D. Zhou and Q. Zhang, *Mater. Lett.*, 2012, **79**, 42–44.
404 M. Trojanowicz, A. Bojanowska-Czajka, I. Bartosiewicz and K. Kulisa, *Chem. Eng. J.*, 2018, **336**, 170–199.
405 J. Jeong, W. Song, W. Cooper, J. Jung and J. Greaves, *Chemosphere*, 2010, **78**, 533–540.
406 H. Yu, E. Nie, J. Xu, S. Yan, W. Cooper and W. Song, *Water Res.*, 2013, **47**, 1909–1918.
407 A. Son, J. Lee, M. Seid, E. Rahman, J. Choe, K. Cho, J. Lee and S. Hong, *Appl. Catal., B*, 2022, **315**, 121543.
408 B. Vellanki, B. Batchelor and A. Abdel-Wahab, *Environ. Eng. Sci.*, 2013, **30**, 264–271.
409 Y. Liang, G. Huang, X. Xin, Y. Yao, Y. Li, J. Yin, X. Li, Y. Wu and S. Gao, *J. Mater. Sci. Technol.*, 2022, **112**, 239–262.
410 H. Zhang, Y. Liu, L. Wang, Z. Li, Z. Lu, T. Yang and J. Ma, *Environ. Sci. Technol.*, 2021, **55**, 11612–11623.
411 T. Zhang, Y. Liu, Y. Rao, X. Li, D. Yuan, S. Tang and Q. Zhao, *Chem. Eng. J.*, 2020, **384**, 123350.

412 Q. Li, J. Hu, H. Wang and Z. Wu, *Appl. Surf. Sci.*, 2021, **562**, 150250.
413 Y.-U. Shin, J. Lim and S. Hong, *Desalination*, 2022, **538**, 115899.
414 B. Ou, J. Wang, Y. Wu, S. Zhao and Z. Wang, *ACS Omega*, 2019, **4**, 9664–9672.
415 J. Sun, L. Liu and F. Yang, *Appl. Catal., B*, 2022, **308**, 121215.
416 M. Jia, Q. Liu, W. Xiong, Z. Yang, C. Zhang, D. Wang, Y. Xiang, H. Peng, J. Tong, J. Cao and H. Xu, *Appl. Catal., B*, 2022, **310**, 121344.
417 Y. Xu, Z. He, S. Yu, L. Li, L. Cai and P. Yi, *Chem. Eng. J.*, 2022, **429**, 132104.
418 X. Liu, G. Liu and S. You, *Chemosphere*, 2021, **263**, 127898.
419 B. Yang, Z. Zhang, P. Liu, X. Fu, J. Wang, Y. Cao, R. Tang, X. Du, W. Chen, S. Li, H. Yan, Z. Li, X. Zhao, G. Qin, X. Chen and L. Zuo, *Nature*, 2023, **622**, 499–506.
420 S. Namboorimadathil Backer, A. Ramachandran, A. Venugopal, A. Mohamed, A. Asok and S. Pillai, *ACS Appl. Nano Mater.*, 2020, **3**, 6827–6835.
421 L. Ren, W. Zhou, L. Wang, K. Lin, Y. Xu, J. Wu, Y. Xie and H. Fu, *Sci. Bull.*, 2023, **68**, 2760–2768.
422 C. Mao, L. Yu, J. Li, J. Zhao and L. Zhang, *Appl. Catal., B*, 2018, **224**, 612–620.
423 I. Zada, W. Zhang, P. Sun, M. Imtiaz, N. Iqbal, U. Ghani, R. Naz, Y. Zhang, Y. Li, J. Gu, Q. Liu, D. Pantelić, B. Jelenković and D. Zhang, *Appl. Mater. Today*, 2020, **20**, 100669.
424 P. Zheng, J. Tang, Z. Zhou, L. Gong, H. Yang, X. Jia, X. Li, Y. Liu and L. Tan, *Surf. Interfaces*, 2021, **22**, 100901.
425 F. Yu, C. Wang, R. Wang, Y. Li, B. Ohtani, A. Fujishima and X. Zhang, *Appl. Surf. Sci.*, 2023, **624**, 157119.
426 S. Gurbatov, E. Modin, V. Puzikov, P. Tonkaev, D. Storozhenko, A. Sergeev, N. Mintcheva, S. Yamaguchi, N. Tarasenka, A. Chuvilin, S. Makarov, S. Kulinich and A. Kuchmizhak, *ACS Appl. Mater. Interfaces*, 2021, **13**, 6522–6531.
427 J. Umlauff, H. Kalt, W. Langbein, J. Hvam, M. Scholl, J. Söllner, M. Heuken, B. Jobst and D. Hommel, *Phys. Rev. B: Condens. Matter Mater. Phys.*, 1998, **57**, 1390–1393.
428 X. Mettan, J. Jaćimović, O. S. Barišić, A. Pisoni, I. Batistić, E. Horváth, S. Brown, L. Rossi, P. Szirmai, B. Farkas, H. Berger and L. Forró, *Commun. Phys.*, 2019, **2**, 123.
429 Q. Liu, Y. Yang, Y. Ni, Q. Wang, H. Yu, X. Zhu, Z. Ying and Y. Song, *Appl. Surf. Sci.*, 2021, **570**, 151175.
430 A. Chaichi, G. Venugopalan, R. Devireddy, C. Arges and M. Gartia, *ACS Appl. Energy Mater.*, 2020, **3**, 5693–5704.
431 X. Lu, G. Wang, T. Zhai, M. Yu, J. Gan, Y. Tong and Y. Li, *Nano Lett.*, 2012, **12**, 1690–1696.
432 A. Ramadoss and S. Kim, *Carbon*, 2013, **63**, 434–445.
433 J. Zhi, C. Yang, T. Lin, H. Cui, Z. Wang, H. Zhang and F. Huang, *Nanoscale*, 2016, **8**, 4054–4062.
434 S. Yang, Y. Li, J. Sun and B. Cao, *J. Power Sources*, 2019, **431**, 220–225.
435 T. Pinto, Y. Núñez-de la Rosa, P. Hammer and J. Aquino, *Electrochim. Acta*, 2022, **408**, 139898.
436 R. Huang, J. Zhang, Z. Dong, H. Lin and S. Han, *J. Power Sources*, 2022, **550**, 232169.
437 P. Pazhamalai, K. Krishnamoorthy, V. Mariappan and S. Kim, *J. Colloid Interface Sci.*, 2019, **536**, 62–70.
438 A. Auer and J. Kunze-Liebhäuser, *Small Methods*, 2018, **3**, 1800385.
439 Y. Tang, L. Hong, Q. Wu, J. Li, G. Hou, H. Cao, L. Wu and G. Zheng, *Electrochim. Acta*, 2016, **195**, 27–33.
440 J. Wang, W. Liu and C. Wang, *J. Alloys Compd.*, 2022, **921**, 166220.
441 B. Babu, S. Ullattil, R. Prasannachandran, J. Kavil, P. Periyat and M. Shaijumon, *ACS Sustainable Chem. Eng.*, 2018, **6**, 5401–5412.
442 J. Kang, J. Kim, S. Lee, S. Wi, C. Kim, S. Hyun, S. Nam, Y. Park and B. Park, *Adv. Energy Mater.*, 2017, **7**, 1700814.
443 S. Patil, H. Phattepur, B. Kishore, R. Viswanatha and G. Nagaraju, *Mater. Renew. Sustainable Energy*, 2019, **8**, 1–10.
444 T. Wu, G. Sun, W. Lu, L. Zhao, A. Mauger, C. Julien, L. Sun, H. Xie and J. Liu, *Electrochim. Acta*, 2020, **353**, 136529.
445 F. Zhou, L. Ouyang, J. Liu, X.-S. Yang and M. Zhu, *J. Power Sources*, 2020, **449**, 227549.
446 Y. Yang, W. Shi, S. Liao, R. Zhang and S. Leng, *J. Alloys Compd.*, 2018, **746**, 619–625.
447 Y. Wang, X. Xue, P. Liu, C. Wang, X. Yi, Y. Hu, L. Ma, G. Zhu, R. Chen, T. Chen, J. Ma, J. Liu and Z. Jin, *ACS Nano*, 2018, **12**, 12492–12502.
448 P. Sun, Z. Cao, Y. Zeng, W. Xie, N. Li, D. Luan, S. Yang, L. Yu and D. Lou, *Angew. Chem., Int. Ed.*, 2022, **61**, e202115649.
449 J. Ge, G. Du, A. Kalam, X. Bi, S. Ding, Q. Su, B. Xu and A. Al-Sehemi, *Ceram. Int.*, 2021, **47**, 6965–6971.
450 S.-T. Myung, M. Kikuchi, C. Yoon, H. Yashiro, S.-J. Kim, Y.-K. Sun and B. Scrosati, *Energy Environ. Sci.*, 2013, **6**, 2609–2614.
451 C. Zhang, H. Yu, Y. Li, Y. Gao, Y. Zhao, W. Song, Z. Shao and B. Yi, *ChemSusChem*, 2013, **6**, 659–666.
452 C. Zhang, H. Yu, Y. Li, L. Fu, Y. Gao, W. Song, Z. Shao and B. Yi, *Nanoscale*, 2013, **5**, 6834–6841.
453 C. Park, E. Lee, G. Lee and Y. Tak, *Appl. Catal., B*, 2020, **268**, 118414.
454 K. Naik, E. Higuchi and H. Inoue, *J. Power Sources*, 2020, **455**, 227972.
455 H. Xie, X. Xie, G. Hu, V. Prabhakaran, S. Saha, L. Gonzalez-Lopez, A. Phakatkar, M. Hong, M. Wu, R. Shahbazian-Yassar, V. Ramani, M. Al-Sheikhly, D.-E. Jiang, Y. Shao and L. Hu, *Nat. Energy*, 2022, **7**, 281–289.
456 L. Zhang, C. Fu, S. Wang, M. Wang, R. Wang, S. Xiang, Z. Wang, J. Liu, H. Ma, Y. Wang, Y. Yan, M. Chen, L. Shi, Q. Dong, J. Bian and Y. Shi, *Adv. Funct. Mater.*, 2023, **33**, 2213961.
457 L. Jakob, L. Tutsch, T. Hatt, J. Westraadt, S. Ngongo, M. Glatthaar, M. Bivour and J. Bartsch, *Sol. RRL*, 2023, **7**, 2200929.
458 W. Wu and Z. Zhang, *J. Mater. Chem. B*, 2017, **5**, 4883–4889.
459 T. David, K. Gnanasekar, P. Wilson, P. Sagayaraj and T. Mathews, *ACS Omega*, 2020, **5**, 11352–11360.

460 Q. Li, S. Fu, X. Wang, L. Wang, X. Liu, Y. Gao, Q. Li and W. Wang, *ACS Appl. Mater. Interfaces*, 2022, **14**, 57471–57480.
461 L. Duy, R. Yeasmin, S.-I. Han, S. Iqbal, C. Park and H. Seo, *Sens. Actuators, B*, 2023, **394**, 134387.
462 S. Zhang, S. Cao, T. Zhang and J. Lee, *Adv. Mater.*, 2020, **32**, e2004686.
463 W. Ni, M. Li, J. Cui, Z. Xing, Z. Li, X. Wu, E. Song, M. Gong and W. Zhou, *Mater. Sci. Eng., C*, 2017, **81**, 252–260.
464 M. Zhang, N. Wu, J. Yang and Z. Zhang, *ACS Appl. Bio. Mater.*, 2022, **5**, 1341–1347.
465 J. Lawton, S. Thornley, S. Wakeham, M. Thwaites, V. Stolojan and M. Baker, *Surf. Coat. Tech.*, 2024, **476**, 130247.
466 G. Zhou, B. Sun, X. Hu, L. Sun, Z. Zou, B. Xiao, W. Qiu, B. Wu, J. Li, J. Han, L. Liao, C. Xu, G. Xiao, L. Xiao, J. Cheng, S. Zheng, L. Wang, Q. Song and S. Duan, *Adv. Sci.*, 2021, **8**, 2003765.
467 J. Kibsgaard and I. Chorkendorff, *Nat. Energy*, 2019, **4**, 430–433.
468 Y. Goto, T. Hisatomi, Q. Wang, T. Higashi, K. Ishikiriyama, T. Maeda, Y. Sakata, S. Okunaka, H. Tokudome, M. Katayama, S. Akiyama, H. Nishiyama, Y. Inoue, T. Takewaki, T. Setoyama, T. Minegishi, T. Takata, T. Yamada and K. Domen, *Joule*, 2018, **2**, 509–520.
469 Z. Wang, T. Hisatomi, R. Li, K. Sayama, G. Liu, K. Domen, C. Li and L. Wang, *Joule*, 2021, **5**, 344–359.
470 H. Asif Javed, A. Qureshi, R. Mehmood, M. Tahir, S. Javed, M. Sarfaraz, M. Javaid, M. Awais and U. Ali, *Int. J. Hydrogen Energy*, 2021, **46**, 14311–14321.
471 M. Yang, B. Dong, X. Yang, W. Xiang, Z. Ye, E. Wang, L. Wan, L. Zhao and S. Wang, *RSC Adv.*, 2017, **7**, 41738–41744.
472 H. Zhang, L. Xie, C. Huang, Z. Ren, H. Wang, J. Hu, H. Zhang, Z. Jiang and F. Song, *Appl. Surf. Sci.*, 2021, **568**, 150933.
473 Y. Peng, Y. Hu, H. L. Chou, Y. Fu, I. Teixeira, L. Zhang, H. He and E. Tsang, *Nat. Commun.*, 2017, **8**, 675.

